High power Kerr-lens mode-locked thin-disk oscillators

Der Fakultät für Mathematik und Physik
der Gottfried Wilhelm Leibniz Universität Hannover

zur Erlangung des akademischen Grades
Doktor der Naturwissenschaften
– Dr. rer. nat. –

genehmigte Dissertation von

M.Sc. José Ricardo Cardoso de Andrade

2020

Referent	Prof. Dr. Uwe Morgner
Korreferent	Prof. Dr. Bernhard Roth
Korreferent	Prof. Dr. Thomas Südmeyer
Tag der Promotion	27.08.2020

In the memory of Maria da Assunção

Abstract

José Ricardo Cardoso de Andrade

High power Kerr-lens mode-locked thin-disk oscillators

Titanium doped sapphire (Ti:sapphire) systems are the backbone of current ultrafast technology and they are invaluable research tools in contemporary science. However, little progress was observed in their average power scaling due to lack of suitable pumping systems, therefore, no Ti:sapphire laser in the kilowatt-class exists. In contrast, ytterbium (Yb) doped gain media is cementing itself as the *new-wave* of ultrafast technology. Enabled by the diminished costs of high-grade crystal production for industrial applications, maturity of optics and the developments of high power laser diodes able to pump these gain media, Yb-doped solid-state laser are more cost effective, compact and of lower complexity when compared to titanium doped sapphire systems. Not only does this makes them attractive for industrial applications, but their lowered complexity and cost mean that their further dissemination through the scientific world becomes easier, opening the doors to cutting-edge research in every scientific subject.

Within this frame, the development aspects of compact high power ultrafast thin-disk laser oscillators based on Yb gain media will be given. Not only about their design and implementation, but also on how to further improve a system by its post-compression and implementing carrier-envelope offset (φ_{CEO}) locking. At the core of this work is the understanding and effective implementation of hard-aperture Kerr-lens mode-locking which enables a successful exploitation of the gain bandwidth offered by these gain media.

The work being reported in this thesis aims to deliver several of the important aspects and hurdles which may be encountered while implementing a state-of-the-art high-power system and also provide a groundwork to future developments by the demonstration of two things: first, how to improve existing numerical methods to help with the design of high-power oscillators and second, give a detailed guide towards the φ_{CEO} locking of such systems.

Keywords: Ultrafast Optics, High-Power Thin-Disk Lasers, Pulse Compression, f_{CEO} locking

Contents

List of Tables

List of Figures

1 Introduction

Ultrafast laser science, the generation and manipulation of laser pulses with durations ranging from a few tens of attoseconds (as) to several picoseconds (ps), is undoubtedly an indispensable part of our current technological, scientific and societal world. Although not present in a directly assessable manner, ultrafast lasers help in the manufacturing of countless of everyday products as they are outstanding material processing tools [1]; they have a large impact in medicine (i.e. LASIK/SMILE [2, 3], PIRL [4], pathology tools [5]); and are disseminated in the research world. In particular, fundamental science has been revolutionized by ultrafast lasers. They enabled the chemistry Nobel prizes for super-resolution microscopy [6] and femtochemistry [7]. Spectroscopy and fundamental physics were revamped through the introduction of the frequency comb and carrier-envelope phase (CEP) control, which won the 2005 physics Nobel prize [8]. That technology together with the 2018 physics Nobel prize – chirped pulse amplification (CPA) [9] – allowed scientists to peer at the ultrafast motion of molecules [10] and electrons [11], and drive the limits of the table-top physics beyond the petawatt (PW) level [12], to name a few. Surprisingly, some of the basic techniques that enable that level of integration nowadays were demonstrated in the beginning of the 90's (semiconductor saturable absorber mirror (SESAM), 1990 [13]; Kerr-lens mode-locking (KLM), 1991 [14]). Naturally, the knowledge gathered since the first mode-locked laser 26 years prior [15] gave a rapid development to these new techniques, specially CPA [9], and nowadays, all these three technologies [9,13,14]. are part[1] of the solid foundations of ultrafast science.

Technological leaps in the field, scaling the energy per pulse in increasingly shorter pulses allow to cover a broad spectral range and nowadays ultrafast lasers come in every size, shape and flavour, depending on their application. Lasers based on mode-

[1] I mean part, not whole!

locked technologies opened the doors to coherent radiation from the THz frequencies, up to soft-X-rays; from less than a picojoule to hundreds of joules of energy per pulse; from nano-sized emitters, to whole buildings needed. Most of the development was enabled by the CPA technology applied to solid state lasers, mainly titanium doped sapphire (Ti:Sa) systems, as this broadband gain material enables the amplification and generation of sub-50-fs pulses just from the application of the stimulated emission of radiation. However, current state-of-the-art amplified Ti:sapphire based sources – which face financial hurdles when scaling the average power[2] – are complex bulky systems that require expert staff and regular maintenance.

Mentality nowadays intends to take advantage of the progress in all aspects of the optical technologies world in order to simplify and compactify ultrafast laser sources. With this new mindset, ytterbium (Yb) based systems seem to start taking a bigger part in laboratories around the world. With the maturity of high-performance mirrors, high power laser diodes and crystal growing, the basis has been laid to shift from amplification of broadband lasers – as is the case of Ti:Sa based CPA and optical parametric CPA systems – to high-power Yb based systems, and, if needed, apply either nonlinear compression or nonlinear conversion [16].

The work presented in this Thesis follows this trend. This manuscript gives insights on the design and implementation of compact high power (>50 W) ultrafast oscillators, targeting multi-MHz repetition rates, along with the demonstration of a technique to enable the use of this laser tool as a high-power frequency comb or a source with a stabilized waveform. Also the route to obtain shorter pulses (sub-50-fs), both directly from the oscillator and through post-compression will be addressed.

1.1 State of the art

There are three main technologies based on ytterbium doped media for high power ultrafast laser sources: fibre [17], Innoslab [18] and thin-disk geometries [16, 19]. While the first two achieve kW-level outputs [16–18], they rely on a chain of pre- and main-amplifiers, or parallelization of the amplification and then coherently combine all out-

[2]Currently there are no high power laser diodes capable of pumping Ti:Sa systems, and so they rely on cascaded laser conversion to be pumped. This increases complexity and cost per delivered Watt of a Ti:Sa system compared to other types of laser.

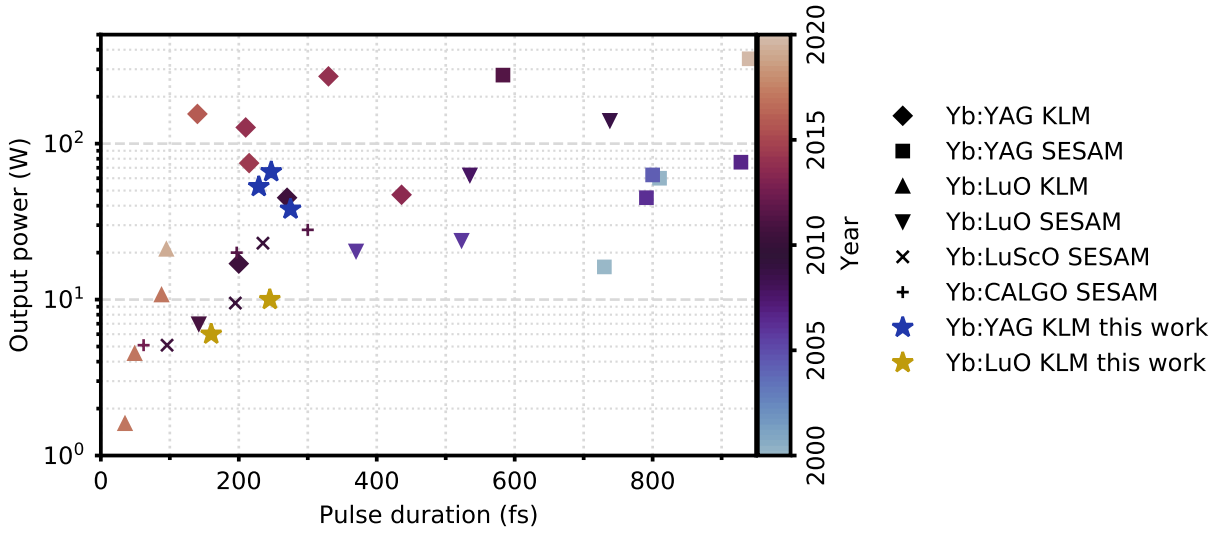

Figure 1.1: Overview of selected state-of-the-art ultrafast Yb-doped thin-disk oscillators, sorted by output average power and pulse duration (<950 fs). Yb:CALGO was also mode-locked via Kerr-lensing, but the output power was solely 0.15 W (30 fs) [25] and therefore was not plotted. References: Yb:YAG KLM [23, 26–29]; Yb:YAG SESAM [30–36]; Yb:LuO KLM [37, 38]; Yb:LuO SESAM [33, 39–42]; Yb:LuScO SESAM [43, 44]; Yb:CALGO SESAM [45, 46].

puts [20]. The scaling rules for each of those technologies, due to their form factors, also limit the maximal pulse energy per amplification channel [18, 21] lending them better suited to high repetition rates. Moreover, in the case of the Innoslab, it is solely used as an amplifier. The thin-disk geometry however, can be used either as a standalone system – an oscillator – or as an amplifier, obeying similar scaling rules as the other two geometries, but as the form factor allows for extremely high saturation energies, its operation at low repetition rates and high pulse energies is also possible. It is therefore the most versatile of the three, when considering its operation repetition rates which span from 100 Hz [22] to >100 MHz [23], with the potential for kW operation in the whole range [16, 24].

This work will solely focus on the development of high-power single-stage thin-disk ultrafast lasers (TDLs), or oscillators, as fibre and slab do not allow this kind of operation. The technical details of the thin-disk-based laser systems will be presented in the next Chapter.

In Figure 1.1 an overview of several of the state-of-the-art ultrafast (<950 fs) thin-disk lasers based on different Yb-doped gain media can be found. The thin-disk geometry is proponent to high output powers, as most reported systems emit >10 W. It can be seen that KLM helped push the boundaries of the high average output powers

to shorter pulses, where both Yb:YAG and Yb:LuO were shown to be able to operate at considerably shorter pulse duration for certain output powers. Note how there are no Yb:YAG SESAM mode-locked TDL systems below 500 fs. In the work shown in this thesis, the oscillators developed are sub-250-fs, 100-W-class systems, in competition with the state-of-the-art Kerr-lens mode-locked thin-disk laser systems.

When also requiring a system with a stabilized carrier-envelope phase slippage (φ_{CEO}), TDLs have proved that not only are they the number one choice when it comes to average power from a stabilized oscillator [47–53] but their noise performance rivals that of the best performing systems to date, displaying integrated phase-noises below 100 mrad [52]. The system presented in this work joins the only three[3] other φ_{CEO} stabilized single-stage systems in the world with output powers >25 W [50–52]. Additional information about the insertion of this work within the state of the art will be given in the appropriate chapter, as the technical foundations will be in place to better understand the currently existing technologies.

Thesis layout

This work was the foundation for a multitude of research projects, where the systems are built specifically to be able to drive multiple experiments concurrently with the ultimate goal of being compact and reliable. During the course of their experimental realization, the gathered knowledge also gives insight into future directions for even more powerful and reliable systems.

This manuscript, after a small technical and theoretical introduction, is divided into two distinct parts: part one, will deal with the implementation and design of high power TDL systems relying on hard-aperture Kerr-lens mode-locking; while part two – solely Chapter 6 – dedicates itself to additional improvements to the developed high-power system, i.e. generation of shorter pulses and φ_{CEO} stabilization.

The first part will be further split into the description of two different lasers: an Yb:YAG based, 100-W-class TDL (Chapter 3 and Chapter 4) and an Yb:LuO thin-disk laser, which, due to its broader gain bandwidth, has the capability to generate shorter pulses than Yb-doped YAG (Chapter 5). Regarding the former system, the technical

[3] All from the same group.

challenges for the implementation of high-power systems will be given in Section 3.1, while the rest of Chapter 3 will be dedicated to the pulsed output characteristics in dependence to specific resonator parameters, such as Kerr medium position or aperture size. The actual guidelines for the implementation of a hard-aperture Kerr-lens mode-locked system will be given later, in Chapter 4, as its behaviour will be studied via the ABCD analysis, allowing to better understand the spatial properties of the experimentally demonstrated resonator and the applied mode-locking concept. The presented computational analysis uses a code developed to calculate the resonator transversal mode while tackling the high intracavity peak powers present in state-of-the-art systems. The numerical results show a good agreement with the solitonic solution of these type of systems. The last chapter regarding the implementation of oscillators – Chapter 5 – presents a different gain material, Yb:LuO and its appeal. The knowledge obtained from the Yb:YAG system is applied to this other material with the objective of reaching the generation of sub-100-fs pulses.

The second part of this work, Chapter 6 will be centered on the nonlinear post-compression of ultrashort pulses, supercontinuum generation in bulk, and φ_{CEO} stabilization of high power systems. These three topics will be discussed in-depth, albeit the main objective being the demonstration of a novel concept for the stabilization of the φ_{CEO}. This technique uses part of the output of the high-power TDL to modulate the gain via depletion modulation and in turn lock the φ_{CEO}. This was motivated by the lack of easily applicable commercial solutions for φ_{CEO} stabilization of high power systems, and resulted in a simple, cost-effective technique capable of stabilizing this oscillator parameter. Benchmarking of the method against pump modulation, a proven method for the stabilization of the φ_{CEO}, will be shown together with its discussion.

The Chapter closing this Thesis will summarise the obtained results and give a small outlook on some of the possible future research on the topics covered in this thesis. Moreover, that Chapter also serves to show how these compact high-power ultrafast systems enable research in various fields by listing all the past and future scientific work that was possible to do with the Yb:YAG TDL system. The last section will cover preliminary results of the study of plasmonic structures using the compressed output of the system.

2 Conceptual background

This Chapter will cover the basic components needed to understand this work, either theoretical or technical. Readers more eager to understand the underlying mathematical proofs and derivations can find them in the appropriately referenced bibliography.

First, in the theoretical side, some of the important nonlinear effects most present when dealing with high peak power light sources will be treated, namely self-phase modulation and Kerr-lensing. This will allow to segway into the aspects of solitonic mode-locking, followed by an introduction of how and why frequency combs arise from mode-locked systems. The theoretical concepts will be closed by a description of the ray-tracing or ABCD formalism, where its fundamentals are needed to better understand Chapter 4.

Afterwards, the thin-disk geometry will be introduced, justifying its use as a single-stage laser concept.

2.1 Self-phase modulation and self-focusing

Light propagation through a transparent dielectric material is classically treated via its polarization response to the electric field of the propagating light. This picture is linear until the electric field of the impinging light starts being commensurable to that of the electronic binding. In that case, higher-order terms start being apparent and the response of the material becomes nonlinear, affecting the propagation of the light as well. When isolating the first- and third-order polarizations, $P^{(1)} + P^{(3)}$, of a medium, for a monochromatic electric field $E(t) = E_0 e^{i\omega t} + \text{c.c.}$ of amplitude E_0 and frequency ω, treated in scalar forms, one obtains [54]:

$$P^{(1)} + P^{(3)} = \left[\epsilon_0 \chi^{(1)} E_0 e^{i\omega t} + \epsilon_0 \chi^{(3)} E_0^3 e^{i3\omega t} + 3\epsilon_0 \chi^{(3)} E_0^2 E_0^* e^{i\omega t} + \text{c.c.}\right]. \tag{2.1}$$

naturally, ϵ_0 is the vacuum permittivity, $\chi^{(n)}$ the n-th order electric susceptibility. The first term of Equation (2.1) pertains to the refractive index n_0 of the medium, the second term to the third-harmonic generation[1] and the last term, also acting on ω, is associated with the nonlinear refractive index n_2. As light intensity is defined as:

$$I = \frac{1}{2} n_0 \epsilon_0 c \left|E_0\right|^2,$$

where c is the speed of light, we obtain from the medium's polarization:

$$n = n_0 + n_2 I, \tag{2.2}$$

with:

$$n_2 = \frac{3}{2 n_0^2 \epsilon_0 c} \chi^{(3)}. \tag{2.3}$$

The consequences from Equation (2.2) can be considerable for ultrashort pulses where the peak intensity can indeed surpass values which make a strong impact on the value of n. Specially if one recalls that an ultrashort pulse has a spatio-temporal intensity profile. The effect of n_2 on the temporal behaviour of the electric field is called self-phase modulation (SPM), while that on the spatial profile is called self-focusing or Kerr-lensing, illustrated in Figure 2.1.

SPM alone cannot change the intensity profile of a pulse, but the time dependent phase added to the pulse as it propagates through a medium of thickness d via SPM is:

$$\varphi_{\text{SPM}}(t) = -n_2 I(t) d \frac{\omega}{c}, \tag{2.4}$$

and it can create new frequencies, as the instantaneous frequency is connected to the derivative of the temporal phase. There is an imprint of the temporal shape of the pulse onto the phase velocity v_{p}, leading to an up-chirp (lower frequencies at the leading edge, and higher frequencies in the trailing edge) along the pulse for values of n_2>0.

The Kerr-lensing, for Gaussian pulses, can be very well described via the aberrationless approximation [55, 56] where the transversal refractive index is treated as parabolic, approximating the Gaussian profile[2]. For media with positive n_2, the low

[1] Added for completeness, usually negligible.
[2] Discussion of the limitations can be found in [57].

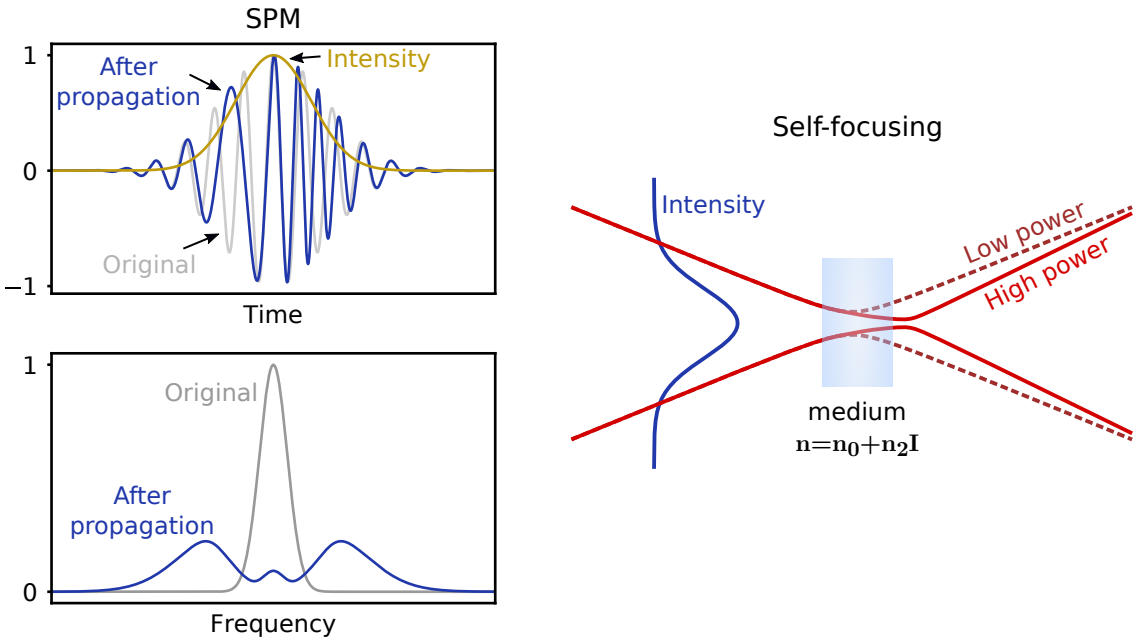

Figure 2.1: SPM and self-focusing examples. SPM does not change the temporal intensity, but new frequencies are created. A high power Gaussian beam suffers an effective focusing when travelling through a medium. In both cases n_2 is positive.

intensity wings of the pulse see the linear refractive index, while the center sees a medium with a higher index $n = n_0 + n_2 I$. This leads to a gradual "bending" of the phase fronts, exactly like a lens. Therefore, the Kerr-lensing can be approximated by a thin-lens, following the formula:

$$\frac{1}{f_{\text{Kerr}}} = \frac{8 n_2 d}{\pi w^4} P_0, \tag{2.5}$$

where P_0 is the peak power, d again medium thickness and w the beam radius [55]. This spatial effect is what allows a laser to be mode-locked via Kerr-lensing. There is a spatial difference between the low power continuous wave (CW) fields and those with high peak power of a mode-locked (ML) laser. This allows the introduction of peak power dependent losses in a resonator. The choice of an appropriate position where the CW beam has a beam size exceeding that of the ML case is suited for the introduction of a physical aperture. Through this aperture, the CW losses are increased while the high P_0 ML beam is left undisturbed, effectively thwarting the growth of low power fields and favouring those of a high peak power nature. This is hard-aperture Kerr-lensing mode-locking (KLM) [58].

2.2 Solitonic mode-locking

Solitons are wave-packets which can propagate undisturbed due to the balance between the accumulated propagation phase and the nonlinear phase-shift induced by the soliton itself. Optical temporal solitons are widely studied, specially when created/lauched into fibres [59]. These solitons are solutions for "free-propagation", i.e. the only effects acting on the wave-packet are those of dispersion and nonlinearities of the medium. When it comes to oscillators, solitons can also be created and sustained within a resonator. Their treatment requires additional elements, as gain/loss mechanisms are present in an oscillator and they alter their stability and behaviour [60–65][3].

To treat such a system, the mode-locking master equation [60] includes all the relevant effects when considering a mode-locked oscillator around its steady state:

$$T_R \frac{\partial}{\partial T} A(T,t) = i\left(-D\frac{\partial^2}{\partial t^2} + \gamma\left|A\right|^2\right)A + \left(g\left(1+\frac{1}{\Omega_g^2}\frac{\partial^2}{\partial t^2}\right) - l - q(T,t)\right)A \tag{2.6}$$

for a slowly varying complex field envelope $A(T,t)$. The roundtrip time is given by T_R. The first complex term of the right side deals with the phase of the pulse accumulated during propagation, taking into account the dispersion D and self-phase modulation. Here, γ:

$$\gamma = \frac{2\pi}{\lambda}\int_0^{2d}\frac{2n_2(z)}{\pi w^2}dz \tag{2.7}$$

represents the SPM coefficient, with λ the vacuum wavelength and $w(z)$ the beam radius along the resonator of length d. The equation with just dispersion and SPM, i.e. ignoring the next term, is the basic solitonic equation, from which the free-propagation soliton can arise. The second term of Equation (2.6) treats the influence of gain and losses. The gain g is also treated as being frequency dependent, seeing a dispersion term $1/\Omega_g^2$, which leads to spectral gain filtering. The linear losses are represented by l and q is time dependent and connected to the mode-locking mechanism's losses, e.g. a semiconductor saturable absorber mirror (SESAM) or KLM.

The in-depth treatment of all the above elements goes beyond the scope of this thesis. In general, there are several simplifications that yield analytical solutions of the $\mathrm{sech}()$ type [64–66]. However, real systems often departure from these simplistic

[3]These references treat this topic in depth.

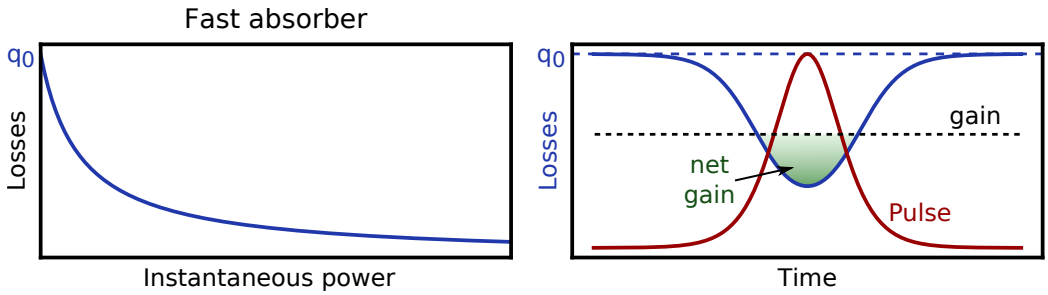

Figure 2.2: Fast saturable absorber, considerations just for the second term of Equation (2.6). For increasing power, the losses diminish. The term q_0 represents the linear losses due to the absorber. On the right, a simplified picture of the time dynamics of the stabilization of an ultrashort pulse are shown. The gain is considered constant for the steady-state of solid-state lasers as the upper laser level lifetime is several orders of magnitude higher than the cavity roundtrip time. Details in the text.

assumptions and the equation is solved numerically instead, until the steady-state is reached.

One of the most important terms in the master equation is the saturable absorber q [65]. This is the term responsible for the stabilization of the pulsed condition and suppression of the growth of CW fields. The Kerr-lensing element coupled to the resonator spatial dynamics acts as a fast absorber, lowering the losses for increasing power of the pulsed field, as seen in Figure 2.2, a picture emphasizing the effects of the gain and losses term of the master equation.

This is a simplified view of the action of mode-locking with a fast saturable absorber. In reality, soft-aperture, or the overlap between the resonator mode and the gain region also play a role in the saturation process. In the case of this work, a soft-aperture effect is also present in the mode-locking and the net gain is also shaped by an instantaneous power dependent gain.

The combined effects of the power dependent losses and/or gain is the self-amplitude modulation (SAM). This creates a nonlinear gain of the mode-locked field, preferred to that of a CW field, and also has a shaping and stabilization role on the envelope of the pulse [65].

When combining the action of the SAM with that of the solitonic condition where the dispersion is negative and balances the nonlinear phase from SPM (n_2>0), the pulse shaping and stabilization is further strengthened by the creation of the soliton, and the laser is operated in the solitonic mode-locking regime.

There are several advantages of solitonic mode-locking with KLM when compared to SESAM. Although SESAM offers easiness of use and scaling is straightforward – i.e. increasing beam radii along the cavity – manufacturing[4] of these mirrors still encounters problems in surface flatness, leading to problems when trying to use large diameter beams. Additionally, the narrow spectral absorption of the quantum well and the increased two-photon absorption for higher modulation depths [67] both limit the pulse duration, and no SESAM mode-locked Yb:YAG high-power TDL system with sub-500-fs has been reported to date. In contrast, for infrared systems, many transparent dielectrics display no dispersion of the $\chi^{(3)}$ element responsible for the n_2 value [68] and the Kerr-effect is deemed instantaneous for the gain bandwidth limited pulse durations, i.e. there is no bandwidth limitation for Kerr media. Moreover, high quality crystals and glasses can be obtained and are relatively cheaper than SESAMs. Additionally, there is minimal heat deposition in the Kerr medium[5]: the "absorbed" light from the saturable absorber is either dumped remotely at the hard aperture or lost through diffraction along the resonator. All these factors contributed to the demonstration of gain limited performance of Yb:YAG and Yb:LuO through Kerr-lens mode-locking [29, 37, 38]. However, there are several geometrical constraints on the cavity design for KLM to be able to achieve proper SAM, resulting in the scaling not being as straightforward as in SESAM based systems [28].

There are other regimes of mode-locking, for example in the positive dispersion regime, where the pulses within the oscillator are chirped, but their treatment falls out of the scope of this manuscript and they can be found elsewhere [69].

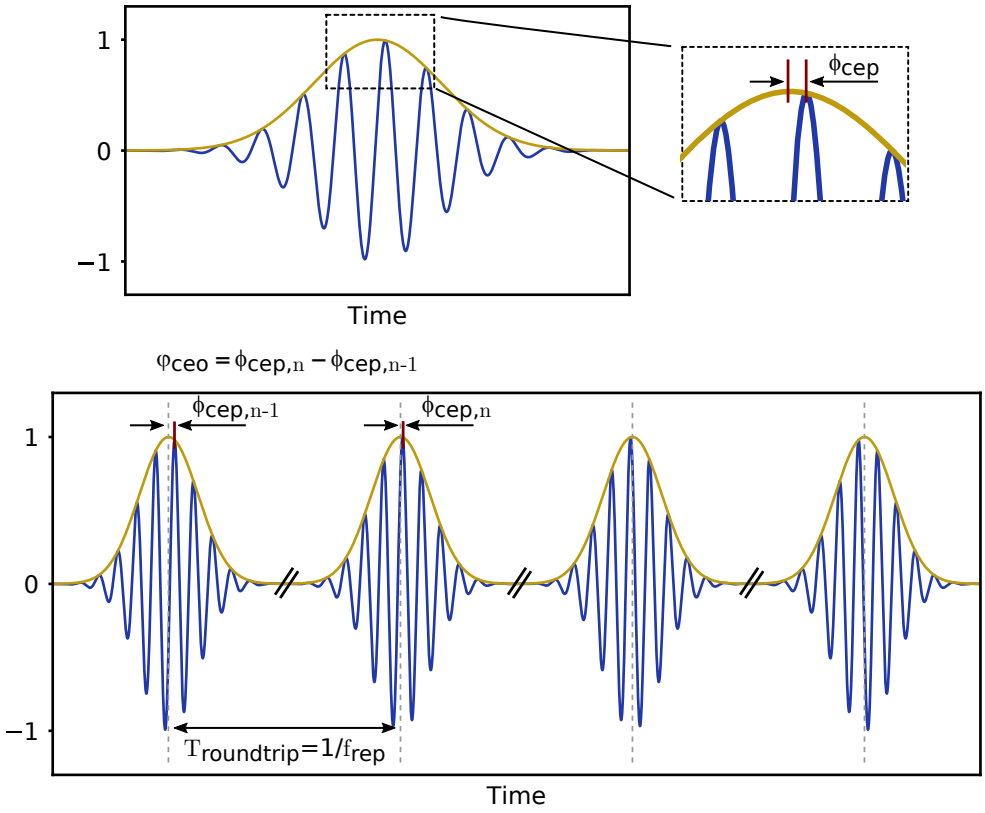

Figure 2.3: Definitions of ϕ_{CEP} and φ_{CEO}. The phase difference between the maximum of the envelope and the maximum of the electric field is called the carrier-envelope phase ϕ_{CEP}. The ϕ_{CEP} difference between consecutive pulses is called the carrier-envelope offset phase φ_{CEO}. In the bottom image we can see a pulse train where all ϕ_{CEP} are different.

2.3 Carrier-envelope phase and φ_{CEO}

The carrier-envelope phase ϕ_{CEP} is defined as the phase difference (relative to the carrier frequency ω_0) between the maximum of the envelope and the maximum of the electric field, as illustrated in Figure 2.3. The electric field propagates at the phase velocity $v_{\text{p}} = \omega/k$, while the envelope propagates at the group velocity $v_{\text{g}} = \partial\omega/\partial k$.

In a mode-locked solitonic oscillator, one controls v_{g} (by controlling the dispersion), as seen in the previous Section. However, the phase velocity v_{p} does not play an integral role on the mode-locking process, and so it is left unchecked. This leads to a discrepancy between the two velocities as they observe different dispersion relations. As a consequence, there is a slippage of the phase under the envelope as it propagates

[4]The author's experience with commercial SESAMs is nothing but frustrating as it seems that their quality is sub-par.

[5]Limited by impurity content, material choice, etc.

through the cavity and, thus, consecutive pulses do not – usually – display the same ϕ_{CEP}. This leads to the definition of the carrier-envelope offset phase φ_{CEO} [70,71]:

$$\varphi_{\text{CEO}} = \Delta t \cdot \omega_0 = \omega_0 \left(\frac{2d}{v_{\text{p}}} - \frac{2d}{v_{\text{g}}} \right) = \omega_0 2d \left(1 - \frac{v_{\text{p}}}{v_{\text{g}}} \right). \tag{2.8}$$

Here, d is the length of the oscillator. The carrier-envelope offset φ_{CEO} is defined as the difference of the ϕ_{CEP} between two consecutive pulses. It is now possible to define the time needed for the same ϕ_{CEP} condition to be fulfilled:

$$T_{\text{CEO}} = \frac{2\pi}{\varphi_{\text{CEO}}} T_{\text{R}} \tag{2.9}$$

which – as $T_{\text{R}} = 1/f_{\text{ref}} = v_{\text{g}}/2d$ – can be re-written to:

$$f_{\text{CEO}} = \frac{\varphi_{\text{CEO}}}{2\pi} f_{\text{rep}} \Rightarrow \varphi_{\text{CEO}} = 2\pi \frac{f_{\text{CEO}}}{f_{\text{rep}}}. \tag{2.10}$$

From the above equation arises the carrier-envelope offset frequency f_{CEO}, the frequency associated to the repetition of same ϕ_{CEP} conditions. If the ratio $r = f_{\text{rep}}/f_{\text{CEO}}, r \in \mathbb{N}$, then pulses which are r pulses apart will have the same ϕ_{CEP}.

The f_{CEO} can also be found in the frequency domain description of the pulse train exiting the oscillator. By taking the description of the electric field of an infinite pulse train, when $I(\omega) = |\mathcal{F}\{E(t)\}|^2$ is the Fourier transform of a single pulse, then, the spectral intensity of the pulse train $I_{\text{pt}}(\omega)$ [8,70]:

$$I_{\text{pt}}(\omega) = I(\omega) \cdot \sum_j \delta \left[\omega - 2\pi \left(j f_{\text{rep}} + f_{\text{CEO}} \right) \right], j \in \mathbb{N}, \tag{2.11}$$

where δ is the Dirac-delta function. Naturally, this is the description for an infinite number of pulses, for a real description one would have to convolute the above result with the Fourier transform of the truncated time-series, which is nonetheless a narrow function[6]. This means that the spectrum is defined as a series of narrow spectral lines located at $f_j = j \cdot f_{\text{rep}} + f_{\text{CEO}}$ with amplitudes defined by the single pulse's characteristics: a frequency comb.

[6]For example a long Heaviside window would result in a very narrow $\text{sinc}()$ function. The linewidth is either way broadened by other physical means arising from noise, cavity finesse, etc.

2.3.1 f-$2f$ detection

The above representation of the spectral features of a mode-locked laser are idealistic. They do not take into account noises which can couple easily to the φ_{CEO}. For example, taking $n = n_0 + n_2 I$ shows that amplitude noise can couple to the phase experienced by the pulse. This becomes very apparent when detecting the f_{CEO}. To measure its value, the most common found technique is the self-referenced detection via an f-$2f$ interferometer [70, 72]. Later, in Chapter 6 other types of interferometers [72] will be briefly discussed, but their underlying concept is the same as the one of the f-$2f$, where two comb components are mixed to produce a beating equal to f_{CEO} by the aid of a nonlinearity.

To measure the f_{CEO}, one heterodynes two spectral components derived from the laser, hence the self-referenced detection. The original components need to be one octave apart as it will be demonstrated shortly. This requirement is a drawback for lasers whose bandwidths are far from exhibiting an octave, but, for now, let's assume that an octave is at hand.

One isolates two spectral regions around the following frequencies, from Equation (2.11):

$$f_n = n \cdot f_{\text{rep}} + f_{\text{CEO}} \text{ and } f_m = f_{2n} = 2n \cdot f_{\text{rep}} + f_{\text{CEO}}, \quad n, m \in \mathbb{N}. \tag{2.12}$$

Performing now the second-harmonic generation of f_n yields $2 \cdot f_n = 2n \cdot f_{\text{rep}} + 2f_{\text{CEO}}$. Now the heterodyne detection between $2 \cdot f_n$ and f_m yields a beat frequency f_{b} [71,72]:

$$f_{\text{b}} = 2f_n - f_m = 2nf_{\text{rep}} - 2nf_{\text{rep}} + 2f_{\text{CEO}} - f_{\text{CEO}} = f_{\text{CEO}} \tag{2.13}$$

After the detection of the f_{CEO} as described above and examplified in Figure 2.4, its stabilization follows. As mentioned before, noise can easily couple into the φ_{CEO}. By stabilizing the behaviour of the f_{CEO}, via a phase-lock loop, the φ_{CEO} becomes fixed and consecutive output pulses of the oscillator have a fixed electric field phase relationship. In the case where f_{rep} is a multiple of f_{CEO}, then the pulses with the same ϕ_{CEP} have a stabilized waveform.

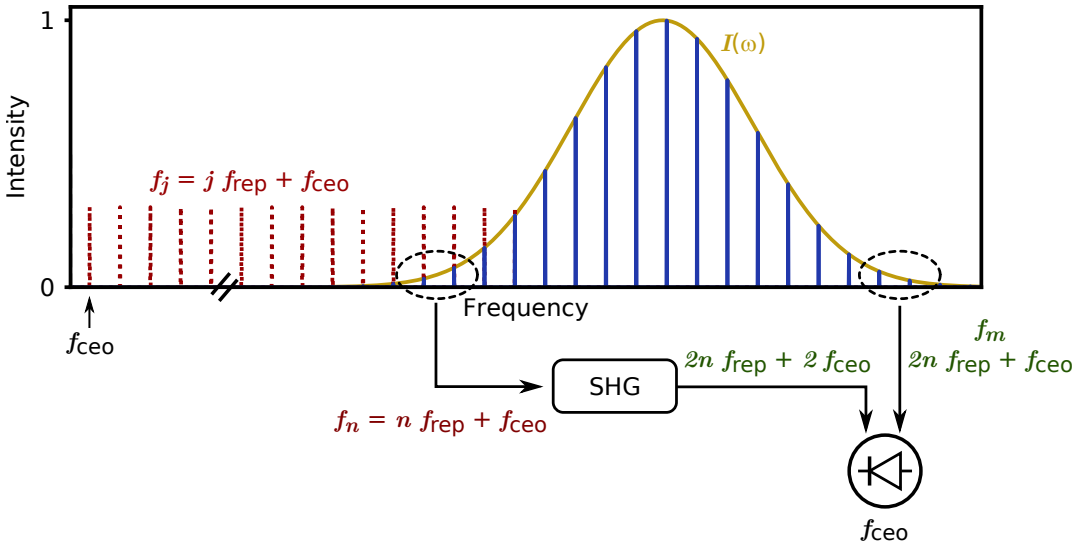

Figure 2.4: Example of an octave-spanning comb and the f-$2f$ self-referenced detection.

It is obvious that this type of detection works easily for oscillators and high-repetition rate systems. However, for amplified systems with low repetition rates the beating term between the f and $2f$ components is better resolved spectrally where the φ_{CEO} can be calculated from a shot-to-shot analysis. This work will not cover the challenges for the detection of low repetition rate systems as they fall out of the scope of this thesis.

2.4 Ray-tracing/ABCD formalism

The ray-tracing/ray-transfer/ABCD matrix formalism was created to analyse paraxial ray propagation through an optical system. It consists of a 2-element vector u describing the ray for its initial state u_i, and by multiplication of a suitable 2x2 (ABCD) matrix M the end state u_o of the ray can be found:

$$u_o = [M]\, u_i \Rightarrow \begin{pmatrix} u_{o,1} \\ u_{o,2} \end{pmatrix} = \begin{pmatrix} A & B \\ C & D \end{pmatrix} \begin{pmatrix} u_{i,1} \\ u_{i,2} \end{pmatrix} \tag{2.14}$$

The matrix M can be either a single optical element, or a series of elements: $M_{\text{total}} = M_n \cdot M_{n-1} \cdots M_1$. This enables the calculation of the end state of the ray from its initial state and a transfer function of the optical train. The formalism is useful in the analysis of cavities or resonators in the sense that it allows to find the conditions where a resonator

acts as a waveguide/resonator, where the rays are confined within such an optical device.

However, for laser physics, it is most advantageous in a form where the vector can fully describe a fundamental Gaussian beam [73], as a solution to the wave equation[7]. In this treatment, not only does the vector describe a beam with a Gaussian intensity distribution, but also most of the matrices for the ray-transfer analysis are compatible with the new vector formulation. All matrices used in this work and some additional information are given in the Appendix A.

In the Gaussian beam description, the vector u takes the form:

$$u = \begin{pmatrix} q \\ 1 \end{pmatrix} \tag{2.15}$$

where q is defined as:

$$\frac{1}{q} = \frac{1}{R} - i\frac{\lambda}{\pi w^2}, \tag{2.16}$$

with R being the radius of curvature of the phase fronts, λ the vacuum wavelength and w the beam radius. This description of the Gaussian beam is for its transversal profile on a plane containing its propagation direction. For the application of the formalism to a vector u_i, then, the application of an ABCD matrix M is as follows:

$$u_o = k\,[M]\,u_i. \tag{2.17}$$

The coefficient k is used to normalize the output vector to the form $u_o = (q_o, 1)$. Alternatively, based on Equation (2.17), we can calculate q_o directly:

$$\frac{1}{q_o} = \frac{C + D/q_i}{A + B/q_i}. \tag{2.18}$$

With the above formulations, it is possible to calculate the effects of lenses, curved mirrors, material propagation, etc. on a Gaussian beam, provided that one has the right matrices. This in itself is already useful, but the analysis of resonators is also possible with the formalism, making this method very powerful as every laser starts from an oscillator based on a resonator. In this case, the train of optics which describe the

[7] There are several textbooks on the topic, but the original paper by Kogelnik et. al. is very instructive and contains all the derivations [73].

resonator becomes an eigen-vector problem. The matrix describing a linear resonator M_{lin} can be calculated from its N elements as:

$$[M_{\text{lin}}] = \left(\prod_{l=N-1}^{1} [M_l] \right) \left(\prod_{i=1}^{N} [M_i] \right). \tag{2.19}$$

From this train of optics, the resonator matrix M_{res} is found to be:

$$[M_{\text{res}}] = [M_{\text{lin}}]^p, p \to \infty, p \in \mathbb{N}. \tag{2.20}$$

What Equation (2.20) dictates is that application of a resonator is described as an entity that repeats itself *ad infinitum*. It still does not mean that this entity would allow the confinement of a Gaussian mode. That can be attested via the trace of the matrix M_{lin}, $\text{Tr}\,(M) = A + D$, which indicates if it is divergent or convergent. Thus, M_{res} is stable if:

$$-1 < \frac{1}{2}\text{Tr}\,(M_{\text{lin}}) < 1, \tag{2.21}$$

and when that is the case, then the eigen-vectors of M_{lin} are the modes invariant to the application of M_{lin}, i.e. application *ad infinitum* of M_{lin} will always yield the eigen-vectors.

Consequently, for a stable cavity, it is possible to calculate the mode at the entrance of the resonator, by calculating the eigen-values $\lambda_{\pm}$ of M_{lin}, and computing the eigen-vectors $u_{\pm} = (q_{\pm}, 1)$. After this eigen-mode is found, the size of the Gaussian beam in the rest of the resonator can be propagated via Equation (2.17). This is how the resonators in this manuscript were calculated, and once again, the used matrices can be found in the Appendix A.

2.5 Lasers based on the thin-disk geometry

Heat deposition in the gain medium is perhaps the biggest hurdle for the power scaling of laser technologies. The requirement for high light intensities in small volumes to increase the stimulated emission interaction probability directly relates to localized heat deposition and strong thermal gradients. Preceding the introduction of the thin-disk technology, the best performing concepts – rods and slabs – relied on a heat flow

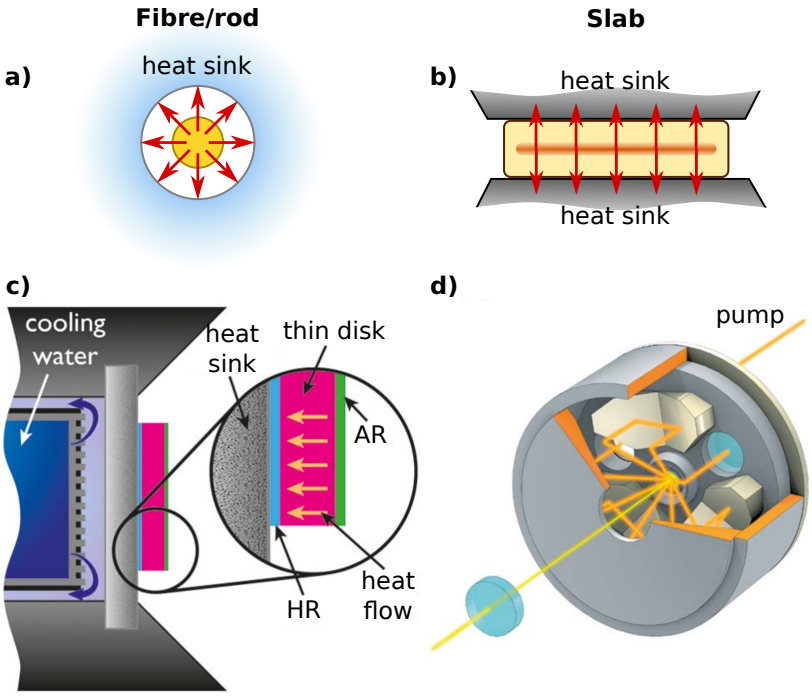

Figure 2.5: Heat flow and cooling for a) rod/fibre, b) slab and c) thin disk. The problem of pumping of thin disks is solved using a multipass approach shown in d). Image c) from [16] and kindly provided by the author. Image d) kindly provided by Trumpf Scientific GmbH.

through a transversal direction to that of the laser amplification path to cool the gain medium. The created thermal lensing and performance losses from the high localized temperatures both decreased the efficiency and beam quality at high pump powers. The thin disk concept was invented to tackle this problems by having the heat flow be one dimensional and parallel to the laser emission [74]. The overview of the heat flow and cooling concepts for the rod/fibre, slab and thin disk can be seen in Figure 2.5 a), b) and c), respectively.

The thin disk is usually a 100-300 µm thick gain medium glued to a heat sink. Water flows behind the heat sink to provide a very effective heat transport system. Pump diameters are in the millimeter to centimeter range and due to the thickness of the medium, makes the pumped region a quasi-2D entity where the heat readily flows into the heatsink. The 2D form factor means that the disk is more akin to an active mirror, which provides gain per reflection. The back side of the disk has and HR coating and the front an AR coating for both pump and laser wavelengths. The geometry has the drawback that at the expense of a small interaction length, the pump absorption/gain per pass is low. To circumvent the pumping problem, an imaging parabolic mirror in

conjunction with deflection prisms ensure that the pump passes >20 times the disk [75], as illustrated in Figure 2.5. To increase the gain, the system is typically used inside a resonator: either as a regenerative amplifier [76] or as an oscillator, where the latter is the case of this work. In both cases it is not uncommon to also have several passes of the resonator path on the thin disk.

3 High power ultrafast Yb:YAG thin-disk oscillator

In this chapter a detailed overview of the development and end results of a high-power ultrafast thin-disk oscillator will be given. In this Chapter only empirical and quantitative effects are shown. Later, in Chapter 4, a more in-depth study of the observed data will be given, as a ray transfer matrix analysis of the system together with the *a posteriori* knowledge of the output parameters allow a better understanding of the underlying phenomena.

3.1 Pumping, layout and CW performance

The thin disk, an ytterbium doped yttrium aluminium garnet (Yb:YAG), is mounted on a diamond heat sink. Diamond as mounting relaxes the design of the resonator as the thermally induced lensing of the gain material is considerably mitigated when compared to traditional metal welding on copper heat sinks [77]. This results from diamond having roughly three times higher thermal conductivity at room temperature and two times the specific heat of copper. For the metal mounted disks, the change in focal distance of the thin disk follows a linear slope of approximately -0.1 dioptre for every $\mathrm{kW/cm^2}$. Contrastingly, disks mounted on diamond display absolute dioptre changes in the order of $0.02\,\mathrm{cm^2/(kW\,m)}$ and lower [77].

The whole assembly, from Trumpf Scientific, is commercially available (TruMicro 5000). The exact properties of the thin-disk are proprietary and there is no information regarding the doping concentration, nonetheless, based on publications using similar systems, it is deduced that the thickness is around 120 µm. The results presented in this section pertain to a thin disk with a curvature of 18 m. Later, in Chapter 6, a disk

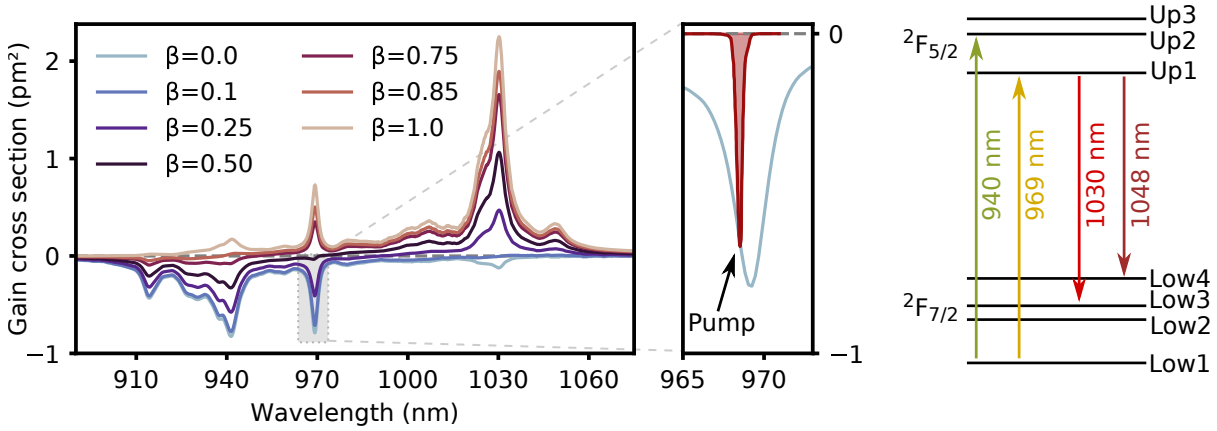

Figure 3.1: Yb:YAG absorption and emission spectra for different inversion (β) values at 20 °C and energy levels scheme. The different shown inversions include the necessary values needed to cross the transparency line: β=0.1 for the gain at 1030 nm, β=0.5 for 969 nm and β=0.85 for 940 nm. The small highlighted area shows the zero-phonon absorption line (for β=0) along with the spectrum of the used pump diode. The spectra are published in [78] and were kindly provided by Dr. Jörg Körner. The diagram is loosely based on the one from [79].

with a radius of 21 m was used. The performance difference between the two cases is negligible when it comes to the full length cavity.

The energy levels diagram of Yb:YAG can be seen in Figure 3.1. It is more common to find diode-pumped solid-state lasers (DPSSL) with this gain material to be pumped in the 940 nm region due to the larger absorption bandwidth (18.3 nm FWHM). This is a consequence of the fact that the emitted bandwidth by high-power laser diodes is typically 3 to 5 nm and the emitted central wavelength dependent on the diode junction's temperature. While it is possible to tune the emission via the coolant temperature, usual values lying between 0.2 and 0.4 nm K^{-1}, it is important to notice that the temperature change and consequently the central wavelength in a laser diode comes from the conjunction of the coolant and the output power. As the current is increased so does the temperature of the diode junction [80][1]. In the case of this work, a volume Bragg grating (VBG) stabilized diode was used to pump the medium through the zero-phonon line at 969 nm [81,82]. As the pumping transition is between the lowest energy levels of each band, the maximum possible inversion between the ground and excited state is 50%. This comes as a consequence of the fast thermalization within each band, the majority of the electronic population being in the lowest possible energy state, also responsible for the fast depopulation of the lower laser level (Low 3) after emission

[1] I cannot give values as this depends highly on age and technology used in the high-power diodes.

of a 1030 nm photon [79]. The low quantum defect between the pump at 969 nm and the 1030 nm lasing transition in Yb:YAG also ensures a low energy deposition without sacrificing gain. Per photon, ~33% less energy is left in the system after emission than when pumping at 940 nm, and moreover, pumping at the zero-phonon line also suppresses nonlinear relaxation effects which impact the temperature of the thin disk [82]. Consequently, pumping at this wavelength is highly beneficial for the thermal management of Yb:YAG. However, the zero-phonon transition has a bandwidth of <3 nm putting hard constraints on the pump wavelength[2], and hence the necessity of the use of a VBG stabilized laser diode.

When it comes to emission, the bandwidth of the material has the main gain transition – from the Up 1 to the Low 3 – enlarged by the Up 1 to Low 2 emission, which is centred at 1024 nm. Although just a moderate improvement, the total bandwidth of ~8 nm (FWHM) is able to go under the 200 fs mark, between 140 fs and 160 fs. Despite not being suited for extremely short pulses, the maturity of Yb:YAG makes it the choice for high-energy and high-average power applications. By deciding to post compress the generated pulses, through nonlinear broadening and linear compression, also high-peak powers are unlocked [84–86].

In the sections below, some of the hurdles in the initial stages of the realization of a high-power ultrafast TDL oscillator will be given. They are regarding the pumping of the material and the continuous-wave performance, which give insights on the proper implementation of a high-power system.

3.1.1 Pumping

The thin-disk chamber works by having 18 passes of the pump light on the thin disk and then a back reflecting mirror ensures a second set of 18 passes of the pump laser on the gain medium. The action of back reflecting the light has the drawback of allowing a partial back coupling of light into the pump fibre. This stray light can decrease the total lifetime of the pump diode and it also has adverse effects on the wavelength stabilization via the VBG.

[2]The spectral absorption measurements at 30 °C of Brown et al. [83] indicate the maximum is at 968.825 nm. The requested wavelength for the pump was 968.8 nm as per the mentioned work. The spectra given in Figure 3.1 have the absorption maximum shifted to 969.2 nm. The spectrum of the pump peaks at 968.5 nm, within the manufacturer's guaranteed tolerance.

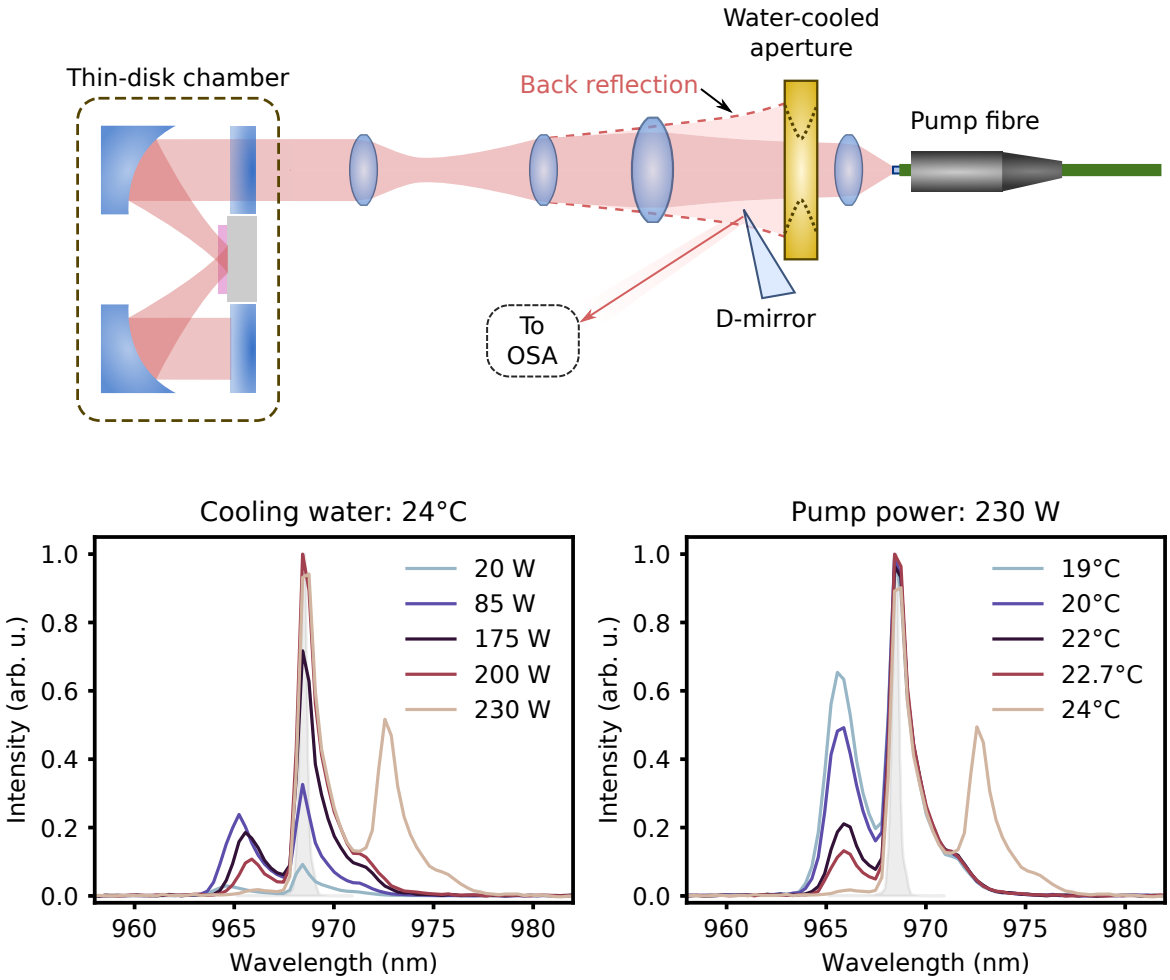

Figure 3.2: Back reflected pump spectrum dependence on water cooling and pump's output power. On top is a schematic of the pump optics and how the back reflection was sampled. The bottom plots are for CW operation of the TDL. In both plots the grey shaded region depicts the free propagation pump spectrum. The water temperature pertains to the water circulating in the pump diode. The output power of the thin-disk laser while pumped by 230 W for the 22.7 °C case was 128 W while for 19 °C it was reduced to 114 W.

During testing of the pump module, the output wavelength stayed stable at 968.5 nm all the way up to 400 W of output power. However, during operation, the spectrum of the pump light is altered due to an increased thermal load and destabilization of the VBG locking due to the back reflection from the thin-disk chamber. Clear evidence of this phenomenon can be seen in Figure 3.2 where the back reflected pump light's spectrum was being recorded while ramping the system up in CW with a 15 % OC. These were taken by coupling part of the back reflected pump into a spectrometer, only possible due to the open characteristic of our home-built pump optics[3] shown

[3]The four-lens-based home-built pump optics were extremely versatile and allowed to achieve precise pump light diameters on the thin disk. Unfortunately they were destroyed in a laser fire, see Fig-

in the Figure. It needs to be understood that in principle the main 969 nm peak has been highly decreased due to the absorption in the gain medium. Nonetheless, at a fixed cooling water temperature of 24 °C the lower wavelength lobes for pump powers up to 200 W are evident. The optimal pumping for this fixed diode's cooling water temperature seems to be around 200 W, the main peak having the highest contrast to the lobe. Past this pump power point a stronger red-shifted lobe appears. Tuning the temperature of the water can effectively mitigate the effect and help the VBG locking of the diode. Lower temperatures contract the grating and the Bragg condition shifts towards shorter wavelengths and vice-versa for higher temperatures. Despite this, it seems that it is not possible to completely eliminate the side lobes at high-power.

On first inspection and due to the characteristics of the pump chamber to fold light multiple times on the gain medium, one might think that this behaviour is a result of amplification of spontaneous emission (ASE) of the thin disk which then in turn can also be amplified by the laser diode. However, cross checking with absorption/emission spectra of Yb:YAG and its laser levels does not support this argumentation. The most simple explanation is the same as to how VBG stabilization works, by positive feedback to the laser diode. The VBG acts as a positive feedback at 969 nm while the thin-disk pump chamber can act as a broadband positive feedback with high attenuation at the absorption peak. The coupling of all three parts – laser diode, Bragg conditions of the VBG and back reflection – probably leads to the observed behaviour.

The detrimental aspect of this phenomenon lies on the reduced efficiency of the system. The laser diode probably still outputs the rated optical power (which is not possible to test), however, the seen lobes have <20% of the absorption capacity of the 969 nm peak. As stated in the caption of Figure 3.2, the output power while pumping with 230 W drops by 12.7 % for the colder circulating water when compared to the optimum at 22.7 °C, which is a considerable amount. One solution would be to have an active water temperature stabilization driven by the measured spectrum; or a look-up-table based on previous measurements. The implementation of such a solution would be beyond the scope of this work. However, it is hoped that the information presented here will help in the development of the next generation of high-power TDLs. The

ure H.4 in the Appendix). After that the pump-fibre's collimation unit was swapped for an enclosed system which no longer allows one to access the back reflected pump light and no investigation was done for the high-power mode-locked operation.

integration, for example, of a simple electronic lobe detection within the pump module to generate an active signal for the cooling water temperature, or installation of a small fibre port on the back side of the back reflection mirror to allow an easy access to the pump spectrum from the radiation leakage of this component are some ideas which could facilitate further developments.

3.1.2 CW operation

The oscillator was designed with several performance aspects in mind. A stylized schematic of the elements of the oscillator can be found in Figure 3.3 along with a ray-transfer matrix simulation of the beam size in both transversal planes. As mentioned in the caption, the hard aperture was not used for the CW performance measurements.

The resonator is designed to use the disk four times as an active mirror per roundtrip, resulting in an effective gain length of eight times that of the thickness.

The measured performance of the thin-disk oscillator in continuous wave mode (CW) can be seen in Figure 3.4. Data for two different output couplers (OC) are shown. The OC with lower transmission (2.4 %) allows for a higher build-up of the stored power within the cavity. The measurement was stopped when the intracavity power reached close to 1 kW in order to avoid potential damage to the optical components. Nonetheless, at this point of operation one can see that air turbulences and possible mechanical de-adjustments of the optics holders are influencing the stability of the laser output. These are attributed to heating of the opto-mechanical parts and optics, and the generation of air drafts inside the oscillator. That is also the case for the operation of the laser at 800 W intracavity for an OC with a transmission of 15 %. The performance in the CW mode showcases the abilities of thin-disk lasers and their high-power handling capabilities. With an output power of 120 W while pumped by 228 W, the optical-to-optical efficiency is ~53 %. Although no measurement of the M^2 was done, the oscillator had been aligned in order to display a Gaussian beam profile and as the highest output power point still falls within the same linear slope of the fundamental transversal mode, there is a high chance that the output still had a low content of higher-order modes. Nonetheless, at this power level it was possible to excite other transversal modes without much effort. In this work, all holders, optics substrates etc. are standard, while the high power systems in the literature have water cooled com-

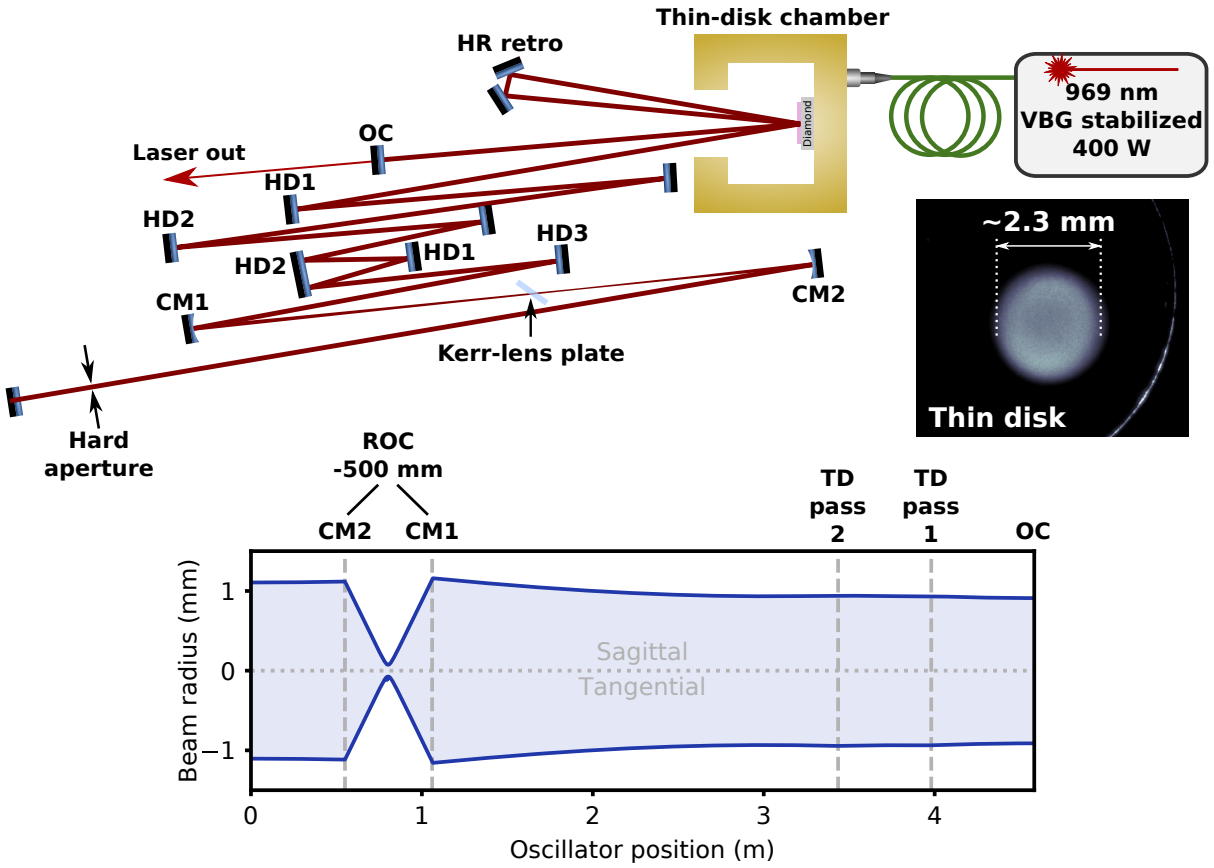

Figure 3.3: Layout of the high power thin-disk Yb:YAG oscillator. The laser is pumped by a volume Bragg grating (VBG) stabilized diode with a maximum output power of 400 W. The different highly dispersive Gires-Tournois-interferometer (GTI) mirrors were marked as HD mirrors. The HD1, HD2, HD3 mirrors introduce $-3000\,\mathrm{fs}^2$, $-1200\,\mathrm{fs}^2$ and $-900\,\mathrm{fs}^2$ of dispersion, respectively. This entails a total of $-21\,000\,\mathrm{fs}^2$ at 1030 nm. CM1 and CM2 are curved mirrors with an ROC of −50 mm. OC: output coupler. HR retro: roof style retro-reflector. For the CW performance the hard aperture was not included into the cavity. The photograph shows part of the thin disk while in operation. It is possible to distinguish the depletion of the pumped region caused by the laser as a "shadow" in the centre of the fluorescence. An ABCD transfer matrix simulation of both sagittal and tangential planes is shown in the graph below for CW operation around the best point (80% overlap with pump region).

ponents and low-expansion substrates [35,87]. In order to go over the 1 kW intracavity or >120 W of output power, in the case of this system, a proper thermal management of all parts is necessary. After all, a 0.1 % leakage of a mirror for an intracavity power of 1 kW is considerable, specially considering the double pass of the components in a linear cavity and how various multi-watt-beams are being shone everywhere within the laser box. Therefore, high quality coatings, low-expansion optical substrates, stable opto-mechanics, thermal management of the laser box and well thought out disposal of stray beams are needed for high operation powers.

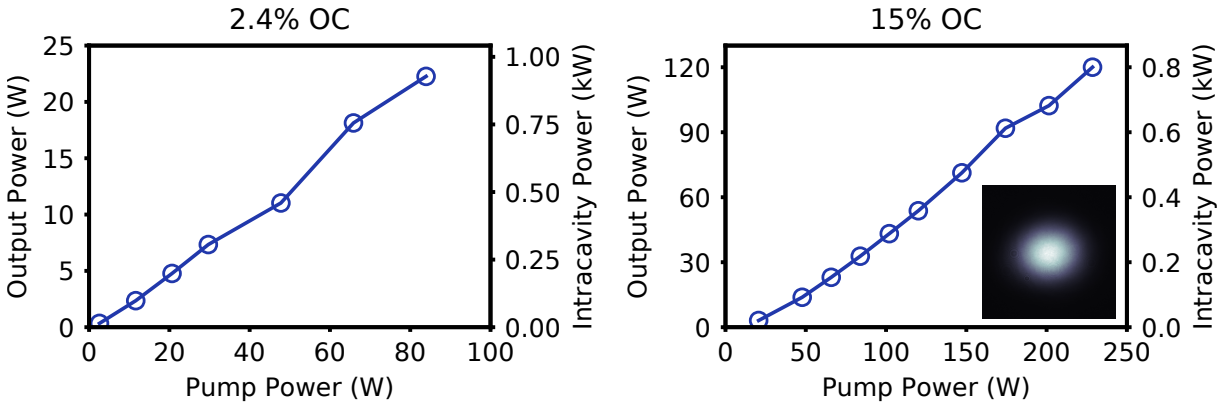

Figure 3.4: CW performance of the Yb:YAG laser. The slope efficiency for a 2.4% transmission output coupler is $\eta_{2.4}$=0.27 and for a 15% transmission OC η_{15}=0.58. The inset shows an exemplary beam profile of the output.

3.2 Mode-locked operation

Hard-aperture Kerr-lens mode-locking together with a net negative group delay dispersion (GDD) allows to operate the oscillator in the mode-locked solitonic regime. Perturbation of the oscillator (by moving the single-reflection HD2 mirror) allows the generation and subsequent stabilization of ultrashort pulses within the cavity as the self-amplitude modulation (SAM) saturates [65, 66, 88]. For the SAM to discriminate the high peak-power pulses from the CW case, first, the oscillator has to be "detuned" from its optimal single-mode CW configuration by increasing the distance between both curved mirrors.

The onset and stabilization of ultrashort mode-locked pulses in an oscillator depend heavily on the interplay between several variables, and the impact that a few selected elements have on the pulsed performance of the laser will be explored below. Namely, hard-aperture size, the position of the Kerr-lensing element and different

Table 3.1: Ranges of observed pulse-durations (τ), average powers ($\bar{P}$) and peak-powers (P_0) for the mirror configuration introducting −21 kfs^2, ~2.3 mm pump diameter, 15% OC and 3 mm FS plate as Kerr medium. The repetition rate was f_{rep}~33 MHz.

	Measured values
τ (fs)	230 to 300
$\bar{P}$ (W)	30 to 50
P_0 (MW)	2.7 to 6.1

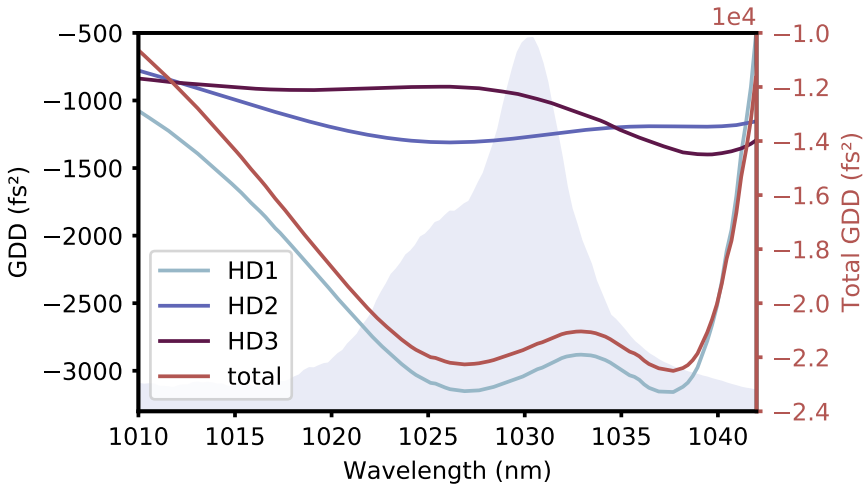

Figure 3.5: Single mirror dispersion profiles, and the total dispersion. HD1 is a GTI mirror from UltraFast Innovations GmbH, design HD73 (4 reflections); HD2 is a mirror from Layertec GmbH, coating 113773 (6 reflections); and lastly HD3 is an in-house design and manufactured by LZH (2 reflections). The total GDD of around $-21\,500\,\mathrm{fs}^2$ has a strong TOD component around the lasing wavelength. The shaded region is the emission cross-section of Yb:YAG.

Kerr-lens substrates and thickness. To understand that indeed the variation is large, a non-exhaustive table with the observed output parameters can be seen in Table 3.1. What is non-quantifiable and plays an important role on the selection of a working point is usability. Whether the warm-up time is long or short, sensitivity to misalignments (usually also contributing to the amount of amplitude noise), reproducibility etc. What is usually referred to as "user-friendliness". Some of the observed values had low reproducibility, typically at either end, requiring an outstanding alignment of the system. It is also hard to quantify whether some of the values were achieved because a certain mirror had a very specific angle of incidence which might tune the GDD a certain way. Although some of the observed parameters were never considered as a reproducible output of the system, they were definitely a solution to the solitonic mode-locking and are considered in the table above. With that said, below, only some selected reproducible cases are shown, those of typical day-to-day performance, or those with better output parameters but reduced "user-friendliness", as is the case of the later section showing the influence of Kerr medium changes.

For all the presented cases, the total negative dispersion introduced in the oscillator was kept the same. In Figure 3.5 it can be seen along with each mirror's individual dispersion profile. The total dispersion is dominated by the HD1 mirror (>50%), chosen

due to its high performance: introduction of a great amount of dispersion per reflection, high damage threshold and low transmission losses. This allowed to increase the negative dispersion considerably without having to either fold the beamline many more times, which increases the losses from the additional reflections, or lengthen the cavity distance. The oscillator length, and hence its repetition rate, was chosen with its later applications in mind [89–93]. As the dispersion from the highly-dispersive mirrors was kept the same for all the taken experimental data, its effects on the working point of the system was not thoroughly investigated. Nevertheless, from the analysis of Figure 3.5 it is possible to discern that the maximum bandwidth of the system will be limited to the region with a fairly flat GDD, between ~1023 nm and 1040 nm, and that the third-order dispersion (TOD) at the maximum of emission of Yb:YAG (approximately -1.6×10^5 fs^3) might increase the time-bandwidth product of the mode-locked pulses, as this deviates the generated spectrum from the analytical solution assuming a flat GDD profile.

An example of the observed emitted pulses from the ultrafast oscillator can be seen in the pulse properties of Figure 3.6. The time bandwidth product (TBP) of the selected operation point is 0.33, the 270 fs pulses being longer than the transform limit of ~260 fs. Nonetheless, the autocorrelation shows an excellent agreement with the solitonic solution. The presented pulses are the typical work-day output of the laser system, the oscillator being aligned for a fast start of operation and stability. The average power is typically between 35 W and 38 W at a repetition rate of 33 MHz with an efficiency of ~37% in this configuration. The bottom plots of Figure 3.6 show the typical short and long time scales energy fluctuations. The fast modulations reach the measurement noise-floor around 10 kHz and the integrated RMS noise is 0.22%. During working hours, the system also displays good levels of stability, with one hour fluctuations being typically below 0.4% RMS. The shown 7 h trace has a downwards trend as this measurement was taken at the end of a working day and the lab temperature was also sinking, raising the relative standard deviation of the measurement to 0.85%. Being that most parts of the oscillator are not temperature stabilized, it is often seen that the warmed-up oscillator output power follows the ambient temperature. Although the depletion region on the thin-disk also follows the temperature of the laboratory, it is not possible to discern whether this is an air wedge effect [94], or simply due to the

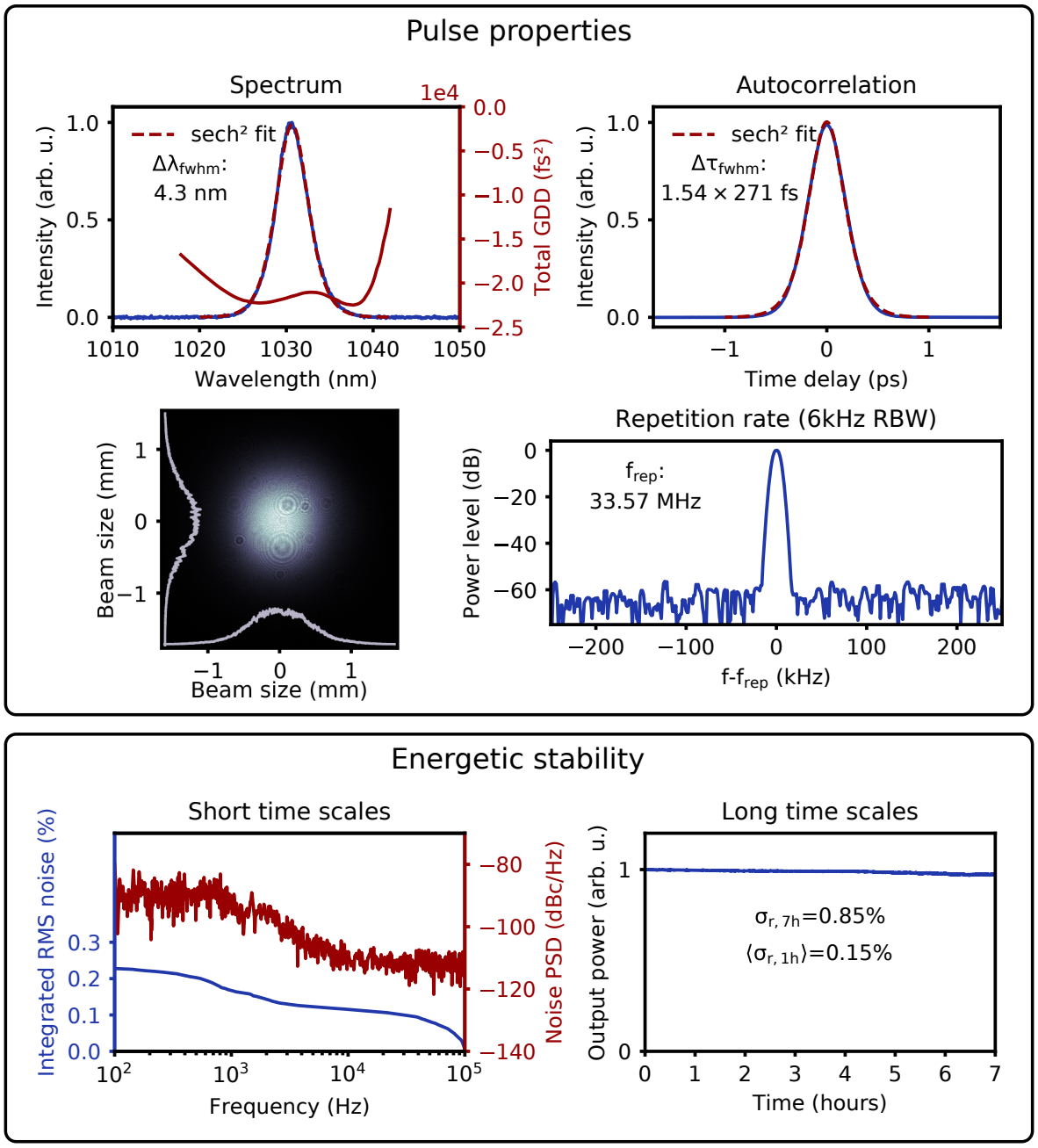

Figure 3.6: Working point of the Kerr-lens mode-locked thin-disk laser for day-to-day operation. On the top, the spectrum of the laser output along with an autocorrelation measurement of the produced pulses. In both cases a sech^2 fit (dashed red) was performed to retrieve the FWHM of the traces and they are displayed in the plot. Additionally, the total negative GDD introduced via GTI mirrors in the oscillator is shown in the spectral measurement. The beam profile and the repetition rate are also shown. The bottom plots show the system stability for short and long time scales. The displayed relative standard deviations pertain to the whole trace ($\sigma_{\mathrm{r,7h}}$) and to the running one hour average ($\langle\sigma_{\mathrm{r,1h}}\rangle$), typical for an output power of ~38 W.

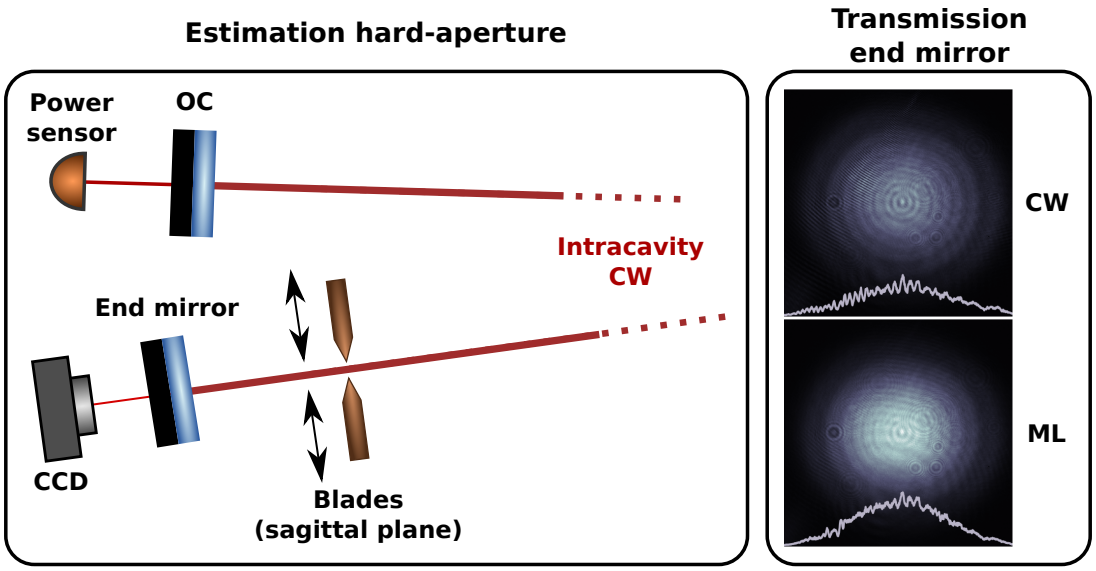

Figure 3.7: Sketch of the procedure for the determination of the hard-aperture size and its effect. While in the single-mode CW operation and a ~80% coverage of the pumped region by the intracavity mode, the effects of closing blades in the sagittal plane are recorded and then the minimum aperture size with no influence on the laser measured. When the hard-aperture is in place it is possible to see its effect on the CW and mode-locked (ML) operation.

contraction/expansion of the opto-mechanical parts. On days displaying extreme amplitudes, the system requires special attention to maintain a stable mode-locked state. Another testament to the necessity of a thermal management of the whole laser box for long and stable operation.

3.2.1 Hard-aperture size

The above presented case was taken with a hard-aperture of 4.1 mm. The rough value for the aperture size was chosen based on the beam diameter close to the end mirror when the cavity was running in CW single-mode and the profile covering approximately 70 to 80% of the pumped region on the thin-disk. When running on this mode, both the beam transmitted through the end mirror and the output power were being observed while closing two blades around the intracavity beam in the sagittal plane. After careful determination of the minimum distance starting to influence the power output, the distance between the blades was used as a rough estimate of the necessary diameter. A sketch of this procedure can be seen in Figure 3.7. The objective was to force the Kerr-lensing, after shifting the resonator stability, to reproduce the same configuration, effectively reducing the losses at the hard-aperture and increasing the

Table 3.2: Hard-aperture size effect on output parameters τ (pulse duration) and P_0 (peak power).

	Hard-aperture diameter (mm)		
	3.65	3.95	4.1
τ (fs)	268	269	275
P_0 (MW)	4.6	4.3	3.9

gain overlap on the thin-disk. The effects of the hard-aperture can be easily seen in the camera images of Figure 3.7, before mode-locking, in CW and then in pulsed operation. The relative amplitude of the diffraction rings becomes lower and there is a higher transmission of the beam. No mode-locking was seen without diffraction from the circular aperture, and comparing efficiencies in CW (optimal, no hard-aperture, ~47% at same pump power, possibility of higher-order mode content) and ML operation (~37%) shows that the hard-aperture is not completely cleared and still introduces some losses in the system, albeit quite low. More information regarding the transmission of the hard-aperture will be given later, in Chapter 4.

As seen in the Table 3.2, when keeping all oscillator parameters the same (but still varying pump power), decreasing the aperture size allowed to achieve shorter pulses and higher peak powers. What is not included in the table is the fact that mode-locking became increasingly harder when moving to a smaller aperture and the efficiency for the given values had also decreased: the output power was higher, but the needed pumping for the rated output increased relatively more. Depending on the configuration of the oscillator the effect can be stronger or diminished. Typically, the aperture was usually kept constant while changing other parameters for daily operation, either 3.95 mm or 4.1 mm, the bigger sensitivity to the alignment of the smaller aperture(s) not being well suited for a fast start and operability of the oscillator.

3.2.2 Kerr-Lens position

An interesting phenomenon, which seems to be strongly coupled to the spatial transversal cavity dynamics (i.e the beam size throughout the cavity), is the position of the Kerr-lensing element for the used oscillator configuration. The behaviour shown in Figure 3.8 is the typical behaviour observed while tuning the system for the optimum parameters. As one moves the Kerr medium further from the focus, closer to the short

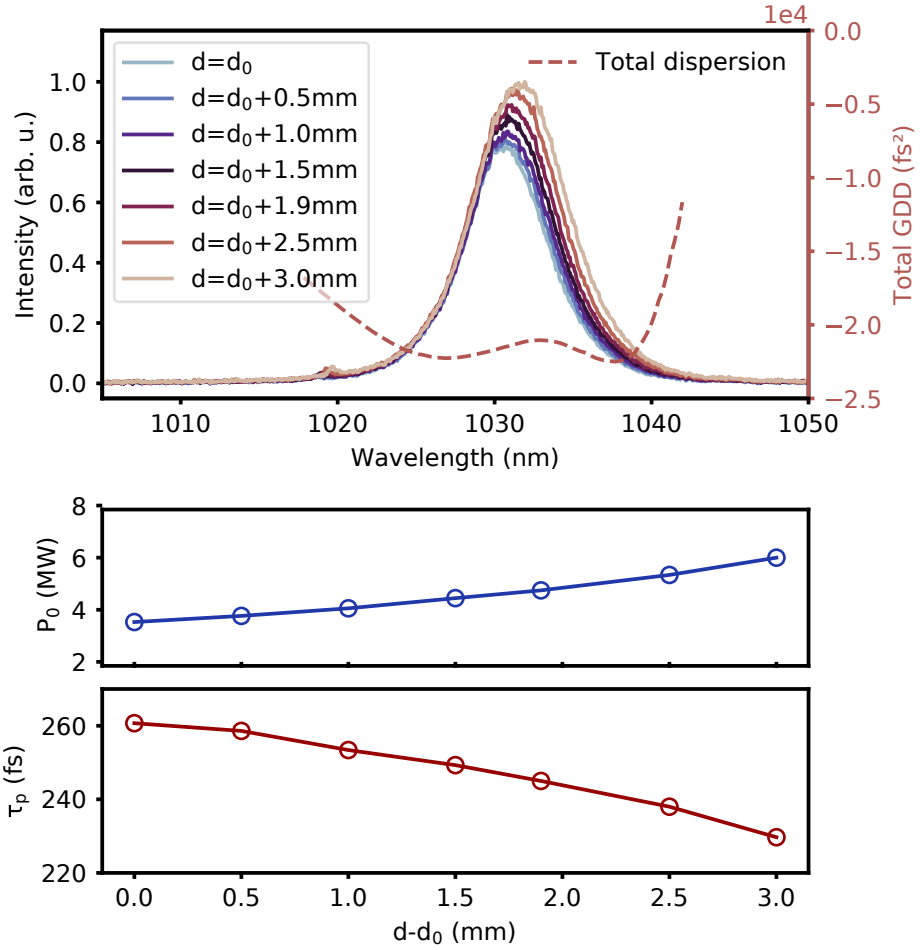

Figure 3.8: Spectral evolution with dependence on the Kerr-lens position accompanied by the measured output peak power (P_0) and pulse duration (τ_p). d_0 is the closest point to the focus, the other points being closer to the curved mirror CM2.

arm (the one with the hard-aperture), shorter and more energetic pulses can be had. The measured points shown in Figure 3.8 were all taken at the onset of a CW background, this means that the pump was adjusted to the point right before a CW breakthrough was seen. Additionally, these points correspond only to distances where it was possible to start the mode-locking process from the CW field, i.e. stabilize the mode-locking from perturbation of the single-reflection HD2 mirror while in CW. The actual range of mode-locked states extended from d_0-1 mm to ~0.5 mm above the last point. However they could only be reached if the system had been previously mode-locked, but they are not considered as their volatile nature – both extrema, at a roll-off of the SAM – made them extremely sensitive.

While tuning the system, nonetheless, one sees that the shorter and more energetic pulses have a higher sensitivity to perturbations and alignment. Rarely was the sys-

tem tuned to the higher extreme, as cooling down of the oscillator during the night and warm-up to a slightly different state the next day, more often than not, did not allow for mode-locking without proper realignment. The "typical" working point would be ~d_0+2 mm. The trade-off point between usability and output peak power/pulse duration. The shorter pulse durations of the measurements shown above had to do with the detuning value (separation of the two curved mirrors) of the system. The above shown measurements were for an oscillator tuning which was not suitable for a several-months-long hands-free operation. The oscillator was sensitive enough that a small misalignment of the perturbed HD2 mirror, for starting of the mode-lock, could inhibit the whole process altogether. With that in mind, the system would normally be kept at a slightly different detuning, lower output peak power and longer pulses, but no need for realignment for several months.

The output characteristics dependence on the Kerr medium's position will be further explored in the next Chapter, with the aid of the ABCD simulations.

3.2.3 Kerr-Lens Substrates

As shown above, it is possible to fine tune the system to significantly differing pulsed behaviours whilst tuning a single parameter. In the explored cases above, the nonlinear response of the cavity was tuned to achieve the different pulse characteristics. While SPM should have stayed quite static due to the solitonic solution, the Kerr-lensing was effectively changing. It is, however, possible to also scale or tune the system while keeping all nonlinear parameters the same, as long as the air/mirrors nonlinear phase shifts, thermal lensing, etc. are still negligible, i.e. the controlled (Kerr medium) nonlinear response is the dominant one.

It is simpler to picture what is meant with the above statement by looking at the governing nonlinear equations. In practical terms, the Kerr-lensing dioptre change (f_{Kerr}^{-1}) and SPM (ϕ_{SPM}) both scale with the nonlinear refractive index n_2, medium length d and peak power P_0:

$$f_{\text{Kerr}}^{-1} = \frac{8n_2 d}{\pi w^4} P_0,$$
$$\phi_{\text{SPM}} = \frac{4n_2 d}{\lambda w^2} P_0.$$

Table 3.3: Fused silica vs. sapphire, thermal properties and nonlinear refractive index. Whenever possible at room temperature. *Average for both axis. **For 800 nm.

	Fused silica	**Sapphire**
$n_2 \times 10^{-16}$ ($cm^2\,W^{-1}$)	2.74 [95]	3 [96]
Thermal conductivity ($W\,m^{-1}\,K^{-1}$)	1.38 [97]	27.21 [98]
Specific heat capacity ($J\,kg^{-1}\,K^{-1}$)	703 [97]	763 [98]
Thermal expansion $\times 10^{-6}$ (K^{-1})	0.55 [97]	5.3* [98]
$dn/dT \times 10^{-6}$ (K^{-1})	12 [99]	12.3** [100]

So, by exchanging the medium to effectively change the $n_2 d$ term, while keeping it in the same location to maintain the same beam size w, to achieve the same SPM and Kerr-lensing, the peak power will have to change. This is an effect that works both ways: would one increase the $n_2 d$ term, then P_0 will have to decrease; while diminishing the $n_2 d$ term should lead to an increase of P_0, if the above conditions regarding the relative contribution of the nonlinearities are still being met. This effect has several practical applications. First, it allows one to find a mode-locked state with lower peak powers for large values of $n_2 d$, and if this is achieved with a relatively long material, this typically means that the mode-locked range shown above in Section 3.2.2 is increased. This facilitates drastically the search for a mode-locked state of the system. Secondly, it can be used to scale the working point of the oscillator by using a lowered value of $n_2 d$, as will be demonstrated below. In the case of this work, the change from a 3 mm fused silica (FS) plate to a 2 mm sapphire plate (c-cut) was attempted, in order to obtain a higher output power at the same pulse duration.

The peak power increase factor from the FS to sapphire swap should be 1.37[4] in this case, if ignoring all other nonlinear terms, i.e. SPM and Kerr-lensing come from the Kerr medium alone. Naturally, air will have a higher relative contribution to SPM, but we are assuming to still be far from it being significant. The nonlinear refractive index of air is four orders of magnitude lower than that of the plate [101] and the thickness of the plate at the sole focus of the system is roughly 10% of the Rayleigh range. These effects will be explored later, in Chapter 4. The biggest differences would

[4]I have no clue which value of n_2 for fused silica to take. This reference at least went through more than 30 published n_2 values. The variation of measured nonlinear refractive indices for FS is amazing. For sapphire, they all seem to be around the same value of $3 \times 10^{-16}\,cm^2\,W^{-1}$, but I assume that there are many different ways of producing FS which completely change the value of n_2 and if anyone really needs to know it in their experimental setup, then they need to measure it!

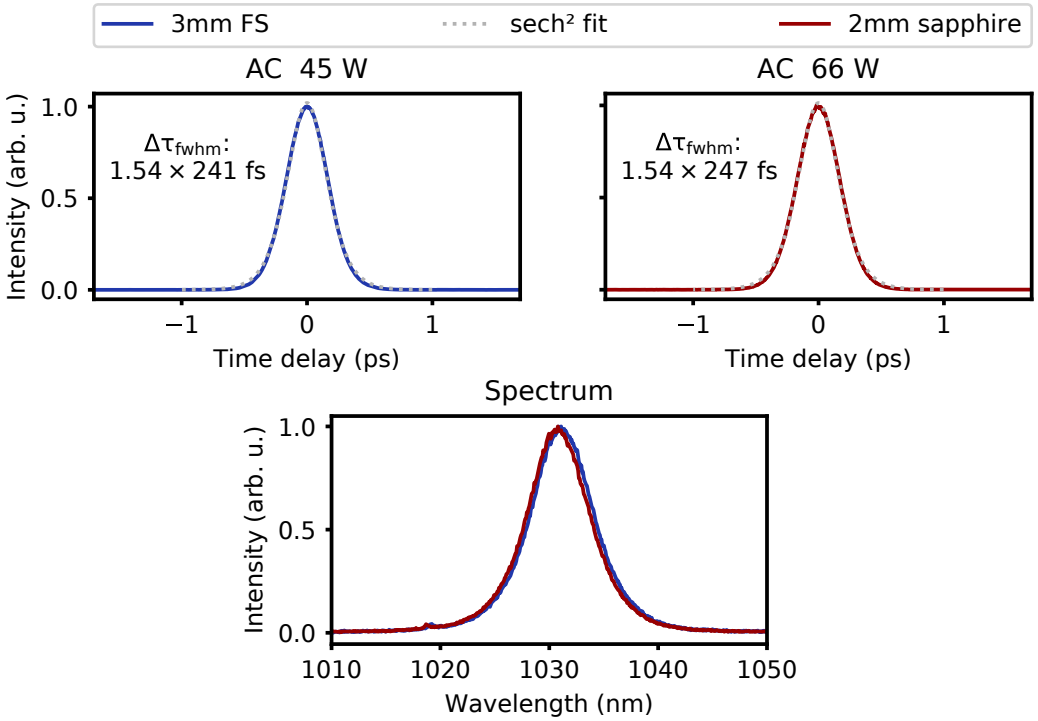

Figure 3.9: Mode-locked performance for a 3 mm fused silica plate and a 2 mm sapphire plate as Kerr media. All other parameters, when possible (see text), were kept the same. The emitted spectrum when using the sapphire plate ended up being 0.5 nm red-shifted.

be in material properties assuming similar absorptions which can highly depend on the quality of the substrates: the 20× larger thermal conductivity and slightly higher specific heat capacity of sapphire means that fused silica probably contributes more to thermal lensing, even considering the bulging effect from the expansion associated to the thermal gradient.

Experimentally, the change of substrates, while trying to keep every other parameter the same, resulted in an increased output power while pulse spectrum and duration stayed the same as it can be attested by the measurements shown in Figure 3.9. The oscillator was first aligned to one of the best performing points for the fused silica plate. The exchange to the sapphire plate had to be accompanied by a small decrease of the repetition rate, to achieve the same stability point in CW operation. As the two plates introduce different amounts of diffraction, this had to be accounted for in the distance between both curved mirrors. Consequently, a slight shift of the position of the Kerr medium was also needed. Naturally, achieving exactly the same settings is extremely demanding, but the approach taken here was proven successful. The measured peak-power increase factor was 1.47, surpassing slightly the expected value from

the simple supposition, an indication that either the n_2 value of FS is wrong, or that fused silica was introducing a higher amount of thermal lensing (by introducing more thermal lensing, then the Kerr lensing does not need to "work as hard"). The system also seemed to be working close to a performance point similar to that of FS. The output peak-power was 7.1 MW, the energetic content ~2 µJ per pulse and the optical to optical efficiency ~26%.

Further scaling was not attempted in order to avoid potential damage to the system, but scaling arguments will be explored below, both in the outlook of this Chapter and in the following one.

3.3 Outlook and conclusion

The system was designed to work in the 110 W to 150 W regime, by further scaling of the output power in a similar fashion to the scaling shown above. Using a 1 mm thick sapphire plate, should in principle double the output power to 130 W. Regrettably, the purchase of the pump diode followed the assumption that a target of 25~30% optical-optical efficiency would be met, as the reported high-power TDL systems usually display this efficiency. However, the needed overshoot of the pump power to start the mode-locking process was not considered, meaning that 400 W might not be enough to start mode-locking at these power levels. In the above case of the 2 mm sapphire plate, mode-locking was started at around 280 W, and stable pulsing with no CW background was then had at ~250 W of pumping. Nonetheless, using instead a 1.5 mm plate would probably allow mode-locking at the maximum pump power, and 90 W to 100 W of output power – around the 10 MW mark – are to be expected.

Overall, further scaling would require rethinking of several opto-mechanical components and their thermal management, as mentioned above, and also scaling of the beam sizes to match damage thresholds, maximum pump densities on the thin-disk, etc. The work done by Brons and colleagues offers a good insight on several techniques or assumptions one can take while further scaling thin-disk laser systems [28, 29, 87].

As per the work shown here, the output pulse characteristics are largely dependent on several parameters and their interplay is very complex. Systematic multi-dimensional analysis would be needed to assess the performance of the oscillator against

changes of all the different parts. Despite the fact that the insight given by such an analysis can be of great scientific interest, reproducibility is usually hindered by the tolerances and stability of the used components, and in the case of these high-power systems, with nonlinearities playing a big role in the characteristics of the output parameters, small changes (e.g. using plates of the same material and thickness but different purity levels) can lead to large variations. In this sense, the exceptional work done by Paradis and his co-workers during his PhD studies on systematic KLM of sub-100-fs TDLs is very instructive [37, 102].

To conclude, a high-power Kerr-lens mode-locked thin-disk laser system delivering up to 66 W of average power at 33 MHz was shown. The measured pulse duration of the output was 250 fs, corresponding to a peak-power of 7.1 MW. Despite these capabilities, the system is typically operated at an output average power of 38 W with the pulses having a duration of 270 fs.

4 ABCD matrix formalism for the design of high peak power laser oscillators

The ABCD matrix formalism [73, 103] is ubiquitous in the laser optics world, helping in the design and analysis of optical resonators. The formalism does not include diffraction, gain guiding, and other effects pertinent to laser physics, which resulted in the creation of extended treatments (some examples [104–106]). However, its basic form is still highly spread and is the beginning platform for the design of resonators: either with gain media within, resulting in oscillators, or simple bare resonators, as is the case of enhancement cavities [107, 108]. Its easy implementation, low computational cost and perhaps its dissemination through commercial and free software make it ideal to study the basic behaviour of light, which in many cases is sufficient for the successful experimental implementation of the designed resonator.

The problem of the simulation of a Kerr-lens mode-locked (KLM) system dates back to the first Ti:sapphire oscillators [106, 109–112] and it felt very attractive to have a full on recipe on how to design such oscillators. Several works were shown where the implementation of ABCD calculations matched measured data accurately [56, 110, 112]. However, those systems were limited to circulating peak powers P_0<5 MW and as laser science has evolved, oscillators achieved new heights and nowadays oscillators with an excess of 0.4 GW [29] of intracavity peak power exist. This in itself does not seem, at first glance, a hurdle to the design of such oscillators using the ray-transfer matrix formalism. However, the introduction of the Kerr-lensing element, following a nonlinear process, becomes increasingly "volatile" as the peak power is scaled. What is meant, is that changes introduced by the Kerr medium become more and more radical

for small changes of the input parameters, leading more often than not, to no solutions of a simulated resonator.

In this Chapter we explore the usage of the ABCD formalism in its basic form to aid in the geometrical characterization of high-peak-power oscillators, mainly oscillators which have a Kerr-lensing element within the resonator. The goal hereby being a simple implementation of the problem of finding the numerical solution of such a resonator and it should not increase the computational load by a substantial amount. The application of a differential evolution algorithm [113] resulted in the possibility to converge to the numerical solution within a useful time, in most cases a few seconds[1].

Below, first, a small demonstration of why high peak powers were detrimental to the calculation of resonator solutions with the commonly found approach will be given. It is followed by how the problem was rephrased to allow the use of a global minimum seeking algorithm. Afterwards, the application of the code to mimic the observed output parameters of the Yb:YAG oscillator presented in Chapter 3, will be shown. The Chapter ends with an outlook to the computer aided design of high-peak-power resonators, and what are the sensible next steps, which, will help the design of the next generation of laser oscillators.

4.1 Motivation

The problem for the geometrical computational design of Kerr-lens mode-locked lasers had typically two phases. First, the resonator including a Kerr lensing element was modelled and its peak power sensitivity – or small signal change – was plotted against the change of cavity parameters, such as mirror separation or Kerr medium position [109, 110, 114, 115]. This serves to identify zones where the resonator would be more sensitive to an increased peak power, distinguishing the low power CW fields from those with high peak powers of a mode-locked laser. The second phase would be to simulate the cavity for some selected parameters, which had been found via the first phase. The objective is to find the beam radii in the different resonator components, allowing a better design of the oscillator, e.g. better pump overlap, lower astigmatism [112].

[1] With a highly unoptimized code.

The former, the relative change to a small signal, or KLM sensitivity δ, has the mathematical description [109, 110]:

$$\delta = \left(\frac{1}{w} \frac{dw}{dP} \right)_{P=0} \tag{4.1}$$

where w is the mode-radius and P, power. It is calculated by the comparison of the beam radius of the linear resonator to that of a nonlinear one containing a calculated Kerr element for a close-to-zero peak-power, and normalizing the result to the zero-power mode size. Naturally, the calculation is performed for a single transversal plane of the oscillator, in the case of hard-aperture mode-locking, at the plane of the aperture. Values of δ>0 mean that the beam increases in size while δ<0 signifies that the radius decreases for increasing peak powers. For hard-aperture KLM, one is looking for points where δ is negative.

The second phase, is typically iteratively calculated [112, 116], by starting with the no-power resonator mode, propagating this mode to the Kerr element, calculating the Kerr matrix (see Appendix A) for the intended peak power P_0 and replacing the linear matrix for the propagation through the medium with the new nonlinear matrix. A new eigen-mode is calculated and the cycle is restarted until the mode no longer changes between iterations. It is usual to compare the beam size. A flowchart of the algorithm can be found in Figure 4.1.

Both design phases can be made either in two dimensions, i.e. for a single transversal plane, sagittal or tangential; or for the full transversal cross-section of the beam in four dimensions. Each plane is given by w, beam radius, and R, curvature of the phase fronts, hence the number of dimensions.

While scaling the peak power, the two-dimensionional calculation yields results until a higher peak power than full calculations, due to the lower amount of degrees of freedom and the fact that in the four-dimensional space all parameters become coupled through the nonlinear Kerr matrix. Nevertheless, the author experienced that both cases failed to be consistent in the high peak power regime. Specially when going many times above the self-focusing critical power, P_{crit}:

$$P_{\text{crit}} = \frac{0.148\lambda^2}{n_0\, n_2} \tag{4.2}$$

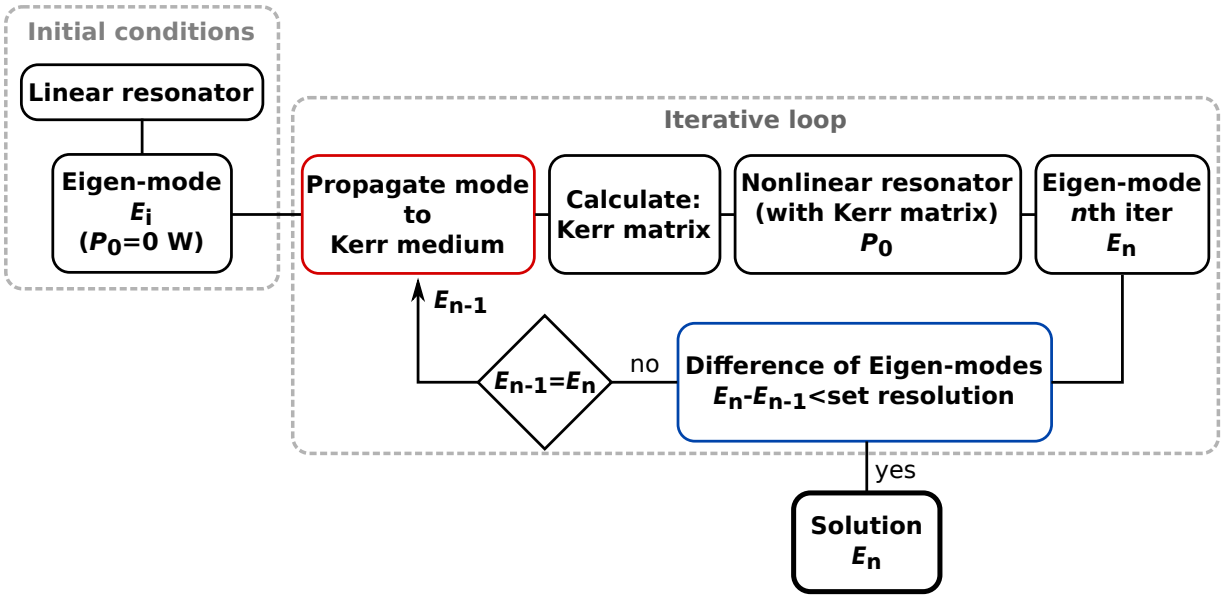

Figure 4.1: Flowchart of the classic approach to the calculation of the nonlinear resonator. The comparison is typically for the mode size. It is a recursive type of algorithm, where newly calculated modes are the inputs of the next iteration. The coloured steps – the *in* (red) and *out* (blue) – of the iterative loop will serve to better understand the next Figure.

of the Kerr medium [117]. As before, λ is the wavelength, n_0 the refractive index and n_2 the nonlinear refractive index. Above this point, the Kerr lensing overcomes the natural diffraction of the laser beam and acts as a self-reinforcing process: as the spatial profile gets smaller, the intensity increases, leading to stronger focusing. Given enough propagation length of a laser with $P_0 > P_{\text{crit}}$ in a medium, all optical Gaussian beams collapse on themselves (if the effects of dispersion would be ignored, i.e. non-changing peak power). This collapse is dubbed catastrophic self-focusing and it results in either damage of the material, or the creation of a filament (more on bulk filaments will be given in Chapter 6). However, both outcomes of the catastrophic self-focusing should be avoided in an oscillator, and when it comes to the computation of the oscillator, if this condition is met while propagating through the Kerr medium, no solution can be found (Figure 4.2 b)). In the case of this work, both fused silica (FS) and sapphire were calculated as Kerr media. Their critical powers are $P_{\text{crit,FS}}$ = 3.9 MW and $P_{\text{crit,sapphire}}$ = 3 MW.

Figure 4.2 gives an overview of the encountered problems at high peak powers. The map shown in a) depicts the influence of the *in* input modes, E_{in}, to the calculated *out* function of the algorithm described in Figure 4.1 (i.e. E_{out}-E_{in}). The phase front

curvatures R_i were the same for all points, being set at the correct solution curvatures. This can also be seen as a brute force approach where one maps the whole space to find which E_{in} yields the solution. The map is for a peak power where P_0 / P_{crit}>15. The solution, a deep "well", is marked. A small step in any of the four dimensions typically yields considerably higher values of the difference calculation although several local minima can be seen in the map. It is possible to identify that most input points yield no solutions (light pink). For example, the approach of the algorithm described above, using the linear resonator as input, yields no solution for the first iteration. It is easy to infer that recursive algorithms have paths which can, at a certain iteration number, fall on the regions where no solutions can be found. The reason for no solutions is either an effective lensing action which does not allow a stable resonator, or catastrophic self-focusing. When the Kerr matrix yields a collapsed beam as the one seen in Figure 4.2 b), it does not allow for solutions of the problem as the beam becomes un-physically "infinitely" divergent at the exit of the plate and the matrix has an effective focal length of zero.

The plot shown in Figure 4.2 c) depicts phase one of the design of a hard-aperture KLM oscillator. In this case, the varied parameter was the position of the Kerr element, a 3 mm fused silica plate. It can be seen that the desirable operation points, δ<0, coincide with the waist of the resonator mode. Understandable, as the intensity is largest at this point. However, no solutions are found for the plate on these positions, most beams simply collapse. Instead, solutions are found displaced on either side of the focus. The effective Kerr lensing for the solutions is also plotted in the same graph. In the laboratory, solutions were found for the positive plate positions, in accordance with the simulations.

The information above shows that the typical approach to the computation and design of KLM oscillators is not sufficient for peak powers in excess of P_{crit}. In the next Sections, a description of the approach taken to overcome these shortcomings when trying to simulate the resonator will be given, followed by selected simulations taking as input measured values.

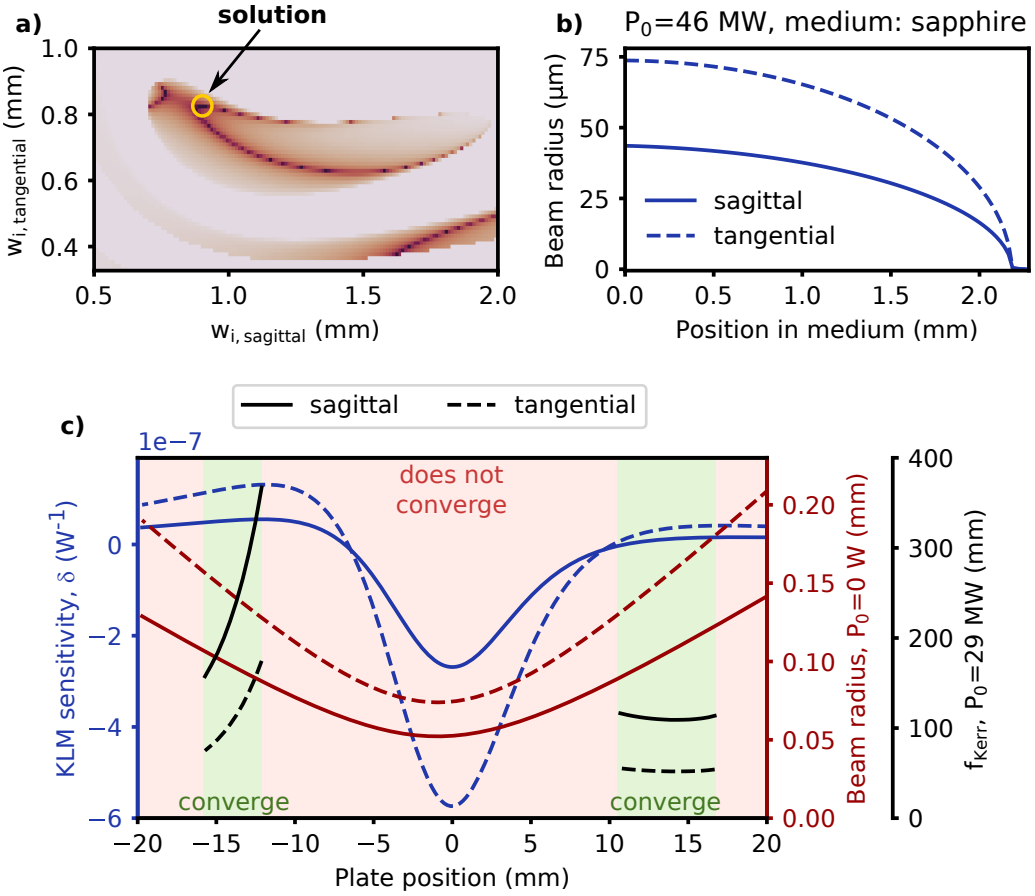

Figure 4.2: Motivation for the application of the differential evolution algorithm to the Kerr lensing problem. In a) a map (for P_0=46 MW) where both R_{sag} and R_{tan} of the solution are fixed while the initial w_{sag} and w_{tan} are varied, the map colour scheme is logarithmic. The solution is a "deep well", marked at the yellow circle. In both b) and c), sagittal and tangential are differentiated via solid and dashed lines, respectively. The example shown in b) shows how the beam collapses on itself for high peak powers. In c) the sensitivity of KLM in function of the position of the Kerr medium (3 mm FS) is plotted (blue) next to the oscillator beam radius (red) for that particular oscillator configuration. Added in black are the calculated effective lenses the Kerr medium introduces, for 29 MW of peak power, and same FS plate. They are calculated from the matrix yielding the Kerr effect. They are extracted from converged solutions of the oscillator with Kerr medium problem. In the red shaded zones no convergence was found.

4.2 Global optimization via differential evolution

For the calculation of the solution of a nonlinear resonator with a Kerr medium where a laser beam with P_0>P_{crit} is circulating, a global optimization algorithm was used. As experimental evidence shows that such oscillators have a solution, i.e. it is possible to mode-lock the systems at extremely high intracavity peak powers. Therefore, a solution has to exist for a simulated oscillator, if the model is accurate enough. As we

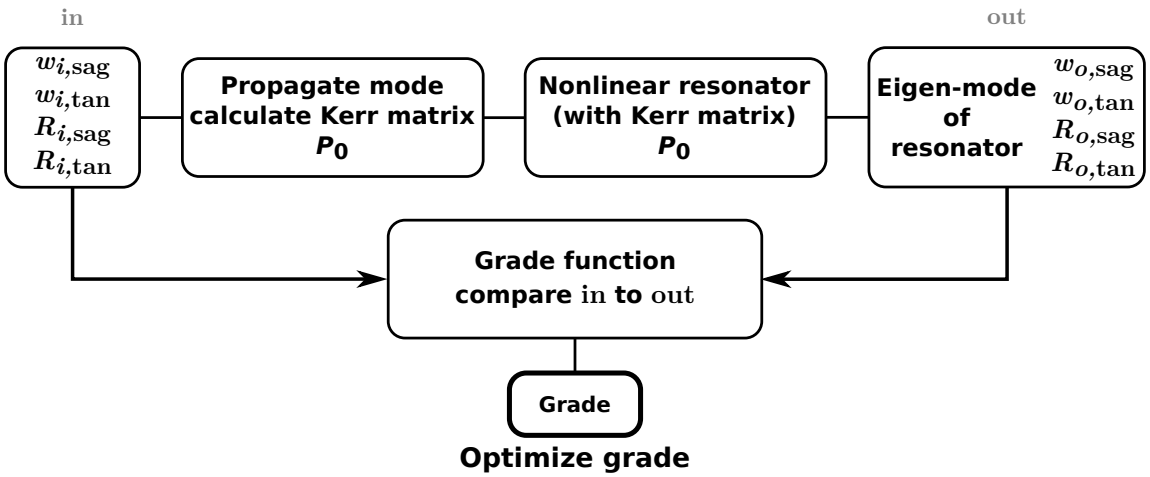

Figure 4.3: Flowchart of the global minimum approach to the calculation of the nonlinear resonator.

are dealing with a resonator, the solution should be an eigen-mode of the problem, or in other words, the eigen-mode yields a Kerr matrix, and the nonlinear element in turn, yields the eigen-mode. There is a one-to-one correspondence between the calculated Kerr matrix and the solution. As a counter-example, in the classical approach, the recursive type of algorithm seen in Figure 4.1, one slowly approaches this solution, however, the first iterations are far from the solution and the input mode yields a Kerr matrix which in turn yields a completely different mode, there is no correspondence between the two.

In this work, instead of recursively applying newly calculated modes, an input mode is fed into the resonator and the resulting eigen-mode calculated from the use of the nonlinear Kerr matrix. The new eigen-mode is then compared to the input mode, as shown in the flowchart of Figure 4.3. The comparison is used as a metric, the closer the two are, the closer one is to the eigen-mode. This allows the use of global minimum finding algorithms, which do not require recursive calculations and potential loss of solutions if on the path to the solution one lands in a no-solution-yielding point.

To grade the two modes, a weighted average was made between the relative errors from beam radius differences (70%) and the reciprocal of the radius of curvature (30%). The reciprocals were used to allow the algorithm to seamlessly go between radius of curvature of $\pm\infty$, as the phase fronts need to be flat at the end mirrors of the modelled

Yb:YAG oscillator. Two close-to-zero valued $\mathrm{erf}()$ functions around the zero point of the reciprocals were also added, and are defined as (with R in millimeters):

$$\left(\frac{1}{R_i}\right)_{\text{penalty}} = 20 * \left|1 + \mathrm{erf}\left(5 \times 10^2 \left(\left|\frac{1}{R_i}\right| - 1 \times 10^{-2}\right)\right)\right|$$

These do not make a big impact to $|R|$>0.5 m but help the algorithm to search only for large radii of curvature. All waists and phase fronts are compared at entrance of the resonator, middle (OC) and after a roundtrip, to ensure that the solution is not disparate and is self-repeating.

At first, the Nelder-Mead [118] (or downhill-simplex) method was attempted. It improved the performance, allowing for solutions to be found for values a few times above P_{crit}. However, the method easily converges to local minima, from which it no longer can escape and a few instructions were added to allow the algorithm to still find the global minimum. But as the peak-power was further increased, the mathematical landscape having "deeper" local minima, the computational time to find a solution was increasing considerably. It was ultimately abandoned for the differential evolution (DE) algorithm [113] which improved the robustness (harder to be trapped in a local minimum) and speed of the calculated problems. An overview of the differential evolution method can be found in the Appendix B.

With an appropriate tool to calculate the propagation of high peak power pulses through a resonator, it was now possible to investigate the behaviour of the Kerr-lens mode-locked oscillator. In the following sections, a quick introduction to the basic hard-aperture KLM oscillator operation will be given, followed by simulations of the experimental results.

4.3 High peak power KLM oscillator modelling

Hard-aperture Kerr-lens mode-locking is a technique where a laser oscillator is tuned in a configuration where low power laser fields observe high losses from a physical aperture placed within the oscillator, while high peak power fields pass through this aperture practically unimpeded. As discussed before, this is the action of the self amplitude modulation (SAM) which saturates at a certain peak power. Now this point is directly tied to the tuning of the oscillator and how the transversal profile of the laser

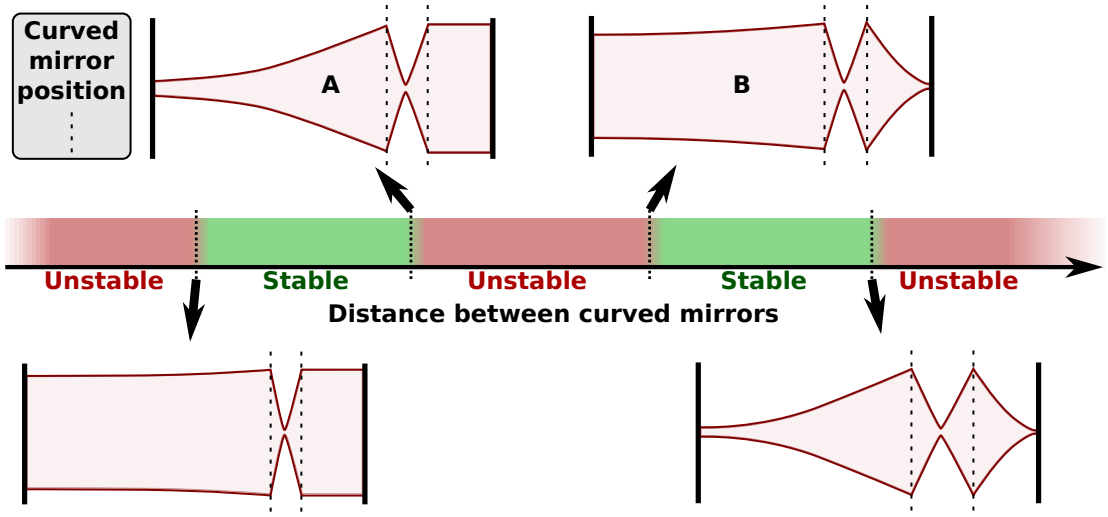

Figure 4.4: Sketch of the stability regimes for a resonator with two curved mirrors and unbalanced arms. The two marked (**A** and **B**) stability edges are the most pertinent for KLM. Not to scale. The large beam modes represent typical roll-off to high beam radii the closer one gets to the unstable condition. The small beam modes roll-off to smaller foci.

within the cavity changes for different peak-powers. In order to increase the saturation power of the SAM in KLM oscillators, it is typical to operate the oscillator close to the point where the resonator becomes unstable[2].

Most KLM systems are linear oscillators with a symmetric focusing section (meaning two focusing mirrors with the same focal distance) and then extended arms on either side of the focusing mirrors. These arms can be symmetric or unbalanced, one arm being longer than the other. As seen in Chapter 3, in this work, the Yb:YAG system is of the latter type, with the thin disk being located on the long arm. Most systems are built like this due to their high reproducibility, as their behaviour was well studied and is well understood [110, 112, 116] and no paradigm shift has occurred yet. One of the most important parameters in such an oscillator is the separation of the two curved mirrors.

As the distance between the curved mirrors is changed, there are two regions where a Gaussian beam will be perfectly confined within the resonator. As one passes from an unstable region into a stable one, the resonator has to transfer from a roll-off condition, being it either infinitely big mode sizes, or infinitesimally small. These are commonly called stability edges. Their behaviour is summarized in Figure 4.4. There are certain edge cases which lend themselves helpful to obtain the right SAM for KLM. These are

[2]Not always, see for example [38].

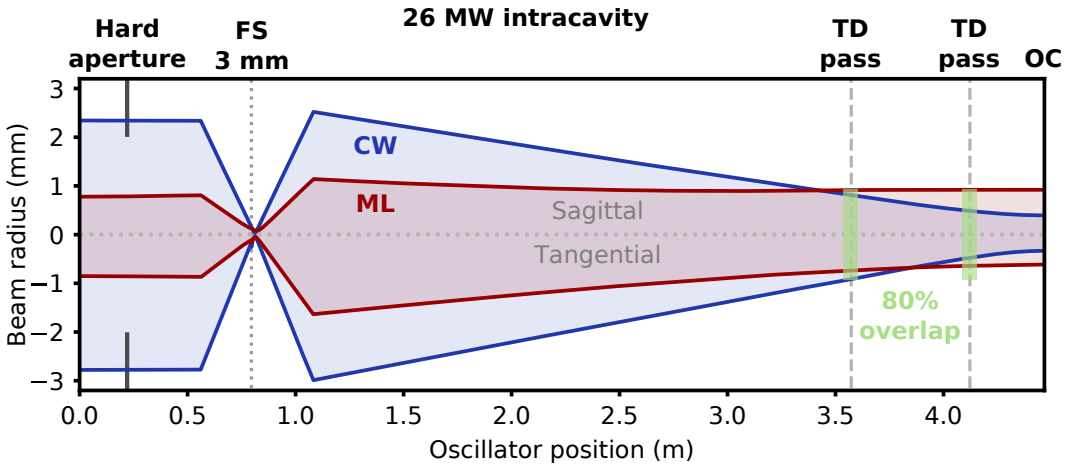

Figure 4.5: Example of a high peak power oscillator at the stability edge **A**. For this configuration the losses at the aperture are greatly reduced and the passes on the thin disk are optimized.

A and **B**: the former is typically used in hard-aperture KLM and the latter for soft-aperture (in the case where the gain-medium is placed close to the focus between the two curved mirrors) [110, 116]. We will only concentrate on the type **A** of resonators, the same one used in the course of this work.

When tuning the resonator to the point **A**, the hard-aperture has the most reliable effects on the short arm, or the large beam mode. This comes from the fact that the laser is mostly collimated in this arm and the action is independent from the location of aperture. Kerr-lensing allows the beam radius to decrease at the hard-aperture side, while increasing at the opposite end mirror.

In the case of this work, the expansion of the beam radius on the long arm can also be used to achieve a better overlap between the mode and the gain region on the thin-disk, further enhancing the obtainable SAM. An exemplifying oscillator close to the stability edge (CW) and its high peak power solution (KLM) as can be found in Figure 4.5.

The reason why the beam is shrunk on both sides (at curved mirrors) is because the Kerr lens element action decreases the divergence of the beam for the first curved mirror while it also pushes the waist closer to the second curved mirror. In the sagittal direction, the Kerr element has an effective focal length of 70 mm while in the tangential direction it is 33 mm. This appears to be counter-intuitive as the beam is larger in this plane, but the intensity is calculated from both the sagittal and tangential beam

sizes and in the end all is completely according to the amount of diffraction experienced by the beams.

With the above introduction to the tuned resonator for an appropriate operation of the KLM, it will be easier to understand the comparison of the simulations to the observed output parameters.

4.3.1 Simulated resonators with experimental data as input

Kerr plate translation

As seen above, the ABCD formalism indicates that the resonator needs to be brought to operate close to the stability edge **A** to increase the SAM. Experimentally however, it is not straightforward to determine this point. To illustrate this, although the ABCD formalism shows that for certain separations of the curved mirrors there should be no resonant condition, the formalism does not take into account diffraction at discrete physical elements, like mirrors etc. and, in contrast, it is indeed possible to operate an oscillator in those forbidden zones, albeit with poor performance. To complicate matters further, higher order transversal modes might be excited while operating the oscillator, specially when closer to any stability edge creating a focus at the end mirror. This makes it hard to conclude that the oscillator is "operating at point X" from simply observing the output properties of the laser system. This serves to substantiate the way the simulations were performed, which do not take as input measured distances but instead focus on the qualitative behaviour. The first presented set of simulations pertain to the measurement shown in Section 3.2.2, where the position of the Kerr element was being translated. Table 4.1 shows a summary of the used input parameters. All other resonator parameters can be found in the Appendix C.

With the arguments presented above in mind, the simulations were done for two distances of the curved mirrors: one was set at ~81% electric field transmission (~96% for intensity) through the hard aperture, and the other, to ~47% transmission of the electric field (~72% for intensity). The former will be dubbed $\mathbf{T}_{\text{hi}}$ and the latter $\mathbf{T}_{\text{lo}}$. The reason on why the electric field is being considered rather than intensity transmission – which is the typical parameter used to describe hard-aperture KLM action [109, 114, 119, 120] – is the following: during the determination of the needed hard-aperture

Table 4.1: List of simulated intracavity peak powers and pulse durations, corresponding to the measured output characteristics shown in Section 3.2.2.

Position (mm)	**Intracavity P_0 (MW)**	**Pulse duration (fs)**
0.0	24	260
0.5	26	258
1.0	28	253
1.5	30	249
1.9	32	245
2.5	36	238
3.0	40	229

size, influence to the output power started at an opening size of approximately 7.5-σ of the beam intensity (w is defined as 2-σ, or $1/e^2$). This is quite surprising as in intensity this corresponds to a near perfect transmission of >99.98% (see Figure 3.7, sagittal only). However, for the electric field, ~0.8% is being diffracted. At an aperture size of ~6-σ, the interference pattern from the diffraction of the blades started to be faint, but apparent (intensity transmission >99.73%, electric field: >96.61%). Hence, considering the electric field for diffractive elements inside a cavity seems a better, empirical, approach: a resonator is an electric-field sensitive device which works on the standing wave principle and disturbance of the electric field affects the roundtrip reproducibility condition[3]. In contrast, the soft-aperture created by the gain region seems to really be more dependent on the intensity of the light rather than on the field as gain is proportional to the intensity.

After a selection of the distance between the curved mirrors, an investigation of the effects that the position of the Kerr medium has on the resonator can be carried out. However, the position of the 0.0 mm point is also difficult to estimate. A certain intracavity peak power converges to a solution for a wide range of Kerr medium positions. Hence, maps of the plate position and the peak power range were calculated and can be seen in Figure 4.6. The holes in the map result from failing to converge. Added to the maps are dotted lines which represent the values of Table 4.1, where the first posi-

[3]After these experiments, it is clear that when building an oscillator, one needs to have clear diameters of at least 9-σ (integral for both directions is different than for just sagittal case) around the beam path to ensure no diffraction losses/shifts.

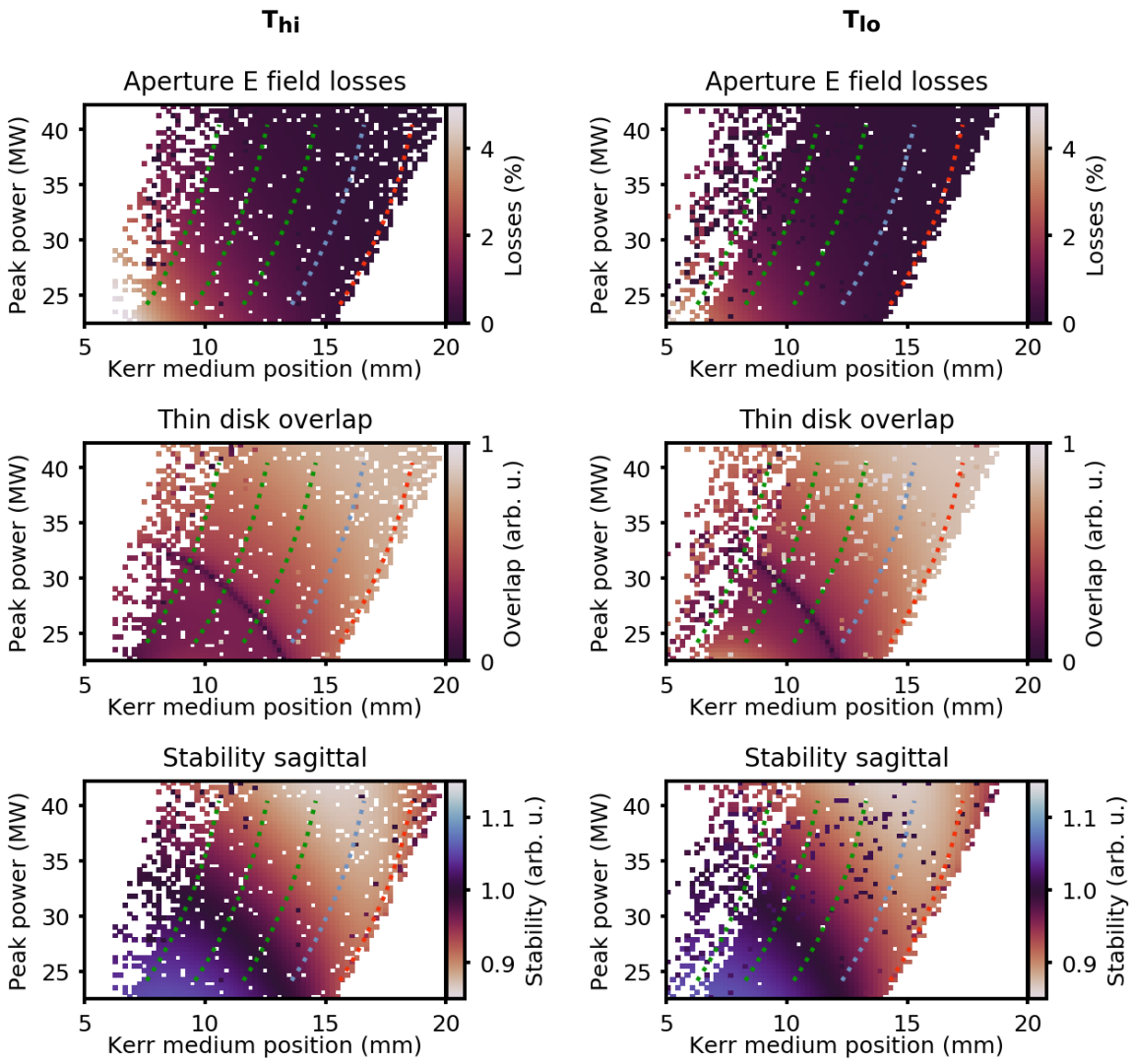

Figure 4.6: Maps of simulated losses, thin-disk overlaps and sagittal stability in function of the Kerr medium position for $\mathbf{T}_{\mathrm{hi}}$ and $\mathbf{T}_{\mathrm{lo}}$. The values of the medium's position are theoretical distances to the focus and higher values mean the plate is closer to the curved mirror/short arm. The overlap is calculated where 80% yields 1, and it is a function of both planes and both passes on the thin disk. The dotted lines represent the values of Table 4.1. They serve as possible paths for the position of the Kerr medium, these are guides to the eye and are separated by 2 mm. The light-blue and red coloured will be explored further below.

tion point (lowest peak power, or 0.0 mm position) is arbitrarily chosen. The light-blue and red cases will be explored further below.

The first apparent feature between both $\mathbf{T}_{\mathrm{hi}}$ and $\mathbf{T}_{\mathrm{lo}}$, is the fact that both display very similar behaviours, although the oscillator is tuned to different positions. The case for the lower transmission requires the medium to be closer to the focus, but the overall results follow the same trend. The upper maps show that as the peak power and distance from the focus increase, so does the electric field transmission through the

hard-aperture. This already hints on why perhaps the output power is higher for Kerr medium positions further from the focus. When analysing the thin-disk overlap maps, another feature is revealed: a dark band, corresponding to a poor overlap between the mode and the gain region. This line is a discontinuity in the sagittal plane, which can be further explained by the stability value of the oscillator above and below this band. This eliminates the green dotted lines as candidates for the actual experimental operability of the oscillator, leaving the region contained between the light-blue and red lines. It is possible to identify that the higher peak powers and further Kerr medium positions have a better overlap with the thin disk, and suffer less losses, allowing for an explanation of the experimentally observed output power behaviour.

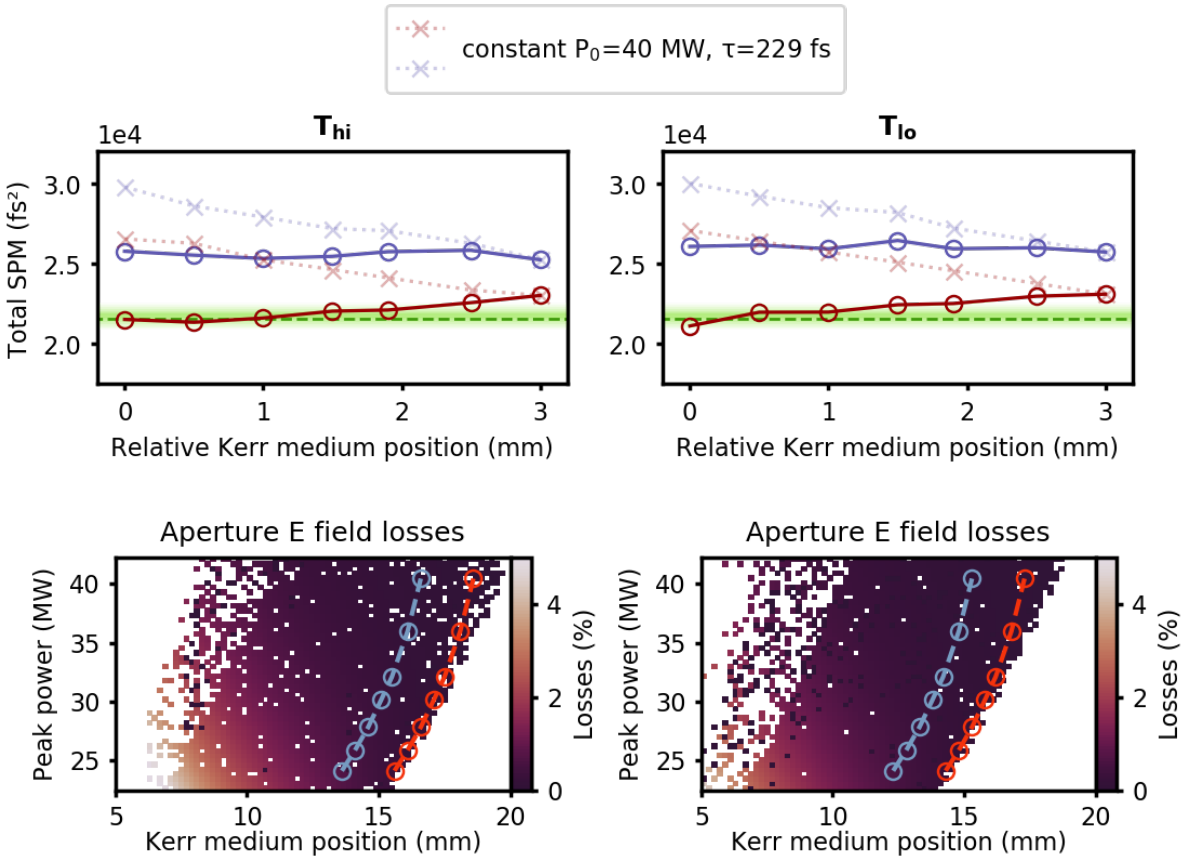

Figure 4.7: SPM calculations for a simulated oscillator. The simulation is for the points of Table 4.1 for the light-blue and red lines in the maps shown in the bottom row, the colours being respective. The zero point was made to coincide, i.e. the Kerr medium position is relative. The simulations are for both $\mathbf{T}_{\mathrm{lo}}$ and $\mathbf{T}_{\mathrm{hi}}$. In shaded green is the absolute value of the introduced negative dispersion into the oscillator (from previous Chapter), with the $21.5 \times 10^3\,\mathrm{fs}^2$ as dashed green. Additionally, a case for constant pulse duration of 229 fs and constant peak power for both starting positions was added to emphasize how SPM is staying roughly constant in this range when using the proper peak power and pulse duration values.

After excluding the green lines as possible stable solutions, the light-blue and red lines remain as the borderline cases for analysis, representing two distinct cases. The light-blue is located closer to sagittal discontinuity and the red one at the edge of convergence of the resonator condition. In order to further understand the behaviour of the measured output characteristics of the oscillator, the observed pulse duration is added to the analysis of these lines. This is achieved by calculating the total nonlinear phase accumulated by the pulse as it travels through the resonator, as the converged solutions allow to retrieve the mode size throughout the whole oscillator. The total SPM within a roundtrip is then converted to fs^2 units using the soliton area theorem:

$$\phi_{\text{nl}} = \frac{\gamma\, E_p}{4\tau} = \frac{|D|}{\tau^2}$$

where $\tau_{\text{FWHM}} = 1.76\ \tau$, D the dispersion, γ the SPM nonlinear coefficient, E_p pulse energy and ϕ_{nl} the SPM nonlinear phase [61, 63]. This effectively includes the pulse duration into the analysis.

Figure 4.7 shows how the SPM, when introduced via the pulse duration, stays fairly constant for all the analysed cases. The solitonic condition dictates that the nonlinear phase contribution for the pulse has to remain the same as one moves the Kerr medium, as the intracavity negative dispersion is fixed. Moreover, as seen in the maps, as the overall thin-disk overlap and the losses improve along the lines, the peak power is allowed to increase, and therefore the pulses have to be shorter to keep satisfying the solitonic condition. As a contrasting situation, if the peak power and pulse durations would be fixed, SPM increases as the Kerr medium is shifted from high to low, instead of staying constant. By combining the pulse duration, peak power and calculated mode size of the oscillator, one finds a great correspondence to the solitonic condition, where no assumptions for it to exist were made. Lines in the map parallel to the light-blue and red lines are "iso-SPM" lines and arise from the necessity of the oscillator to maintain the nonlinear shift equal to the negative dispersion within the oscillator. It also appears that the convergence corner case (red line) fits the best with the experimentally introduced amount of SPM. In all the simulated points, the nonlinear phase shift from air accounts for roughly 10% of all the accumulated phase (n_2=2.9 $\times$ 10^{-19} W cm^{-2} [121], however the literature values vary strongly, which would affect the relative contribution by $\pm$1%.).

Fused silica plate to sapphire plate

In the previous Chapter a change from a 3 mm fused silica plate to a 2 mm sapphire substrate was shown. The same change was emulated via the ABCD code and will be demonstrated below. The simulated oscillator was tuned to display the same amount of transmission values through the hard aperture, as described above for $\mathbf{T}_{\text{hi}}$ and $\mathbf{T}_{\text{lo}}$. This is done by changing again the separation of the curved mirrors. The results from simulating the FS plate to accumulate 23×10^3 fs^2 (roughly between the two cases shown in Figure 4.7) and then the sapphire with the resonator tuned to the new positions is found in Figure 4.9.

The solutions for the 2 mm sapphire plate accumulate nonlinear phases similar to those of Figure 4.7. By choosing the point also displaying the same amount of SPM yields a very well agreeing resonator, although going from P_0/P_{crit}~8.2 to being >15 times above P_{crit}.

For both Kerr media, the oscillator seems to favour the same initial beam radius through the hard-aperture (<0.2% of electric field losses) and the overlap on the thin-disk is also very similar in both cases. When looking at the focus, its is possible to see the agreement between both media once again. It is quite instructive to observe the effects of the Kerr lensing on the $\mathbf{T}_{\text{hi}}$ case, where, to the left of the plate the divergence has been quite altered when compared to the CW case while to the right, the focus position is shifted further, closer to the curved mirror. As stated before, the curved mirrors now "see" effective foci at different locations, yielding a resonator better suited for the transmission through the hard-aperture and better gain overlap. The focus of the CW case does not display a strong amount of astigmatism. This comes from the choice of angle on the curved mirrors, following the procedure set in [103] for astigmatically compensated foci[4]. However, this only works for the low power resonator, as Kerr-lensing is then a second source of astigmatism. Its effect can be seen in the focus region, and in the complete oscillator. The resonator is well compensated for the astigmatism on the short-arm, but then yields a slightly elliptical beam on the long-arm. Lastly, the nonlinear air contribution went up to approximately 13% of the total for the sapphire plate, as the Kerr medium now covers a smaller volume of the focus.

[4]It was later understood that this is not necessarily a good effect for KLM TDL lasers. This only guarantees a confocal configuration on both planes, but the overall resonator itself is not astigmatically compensated.

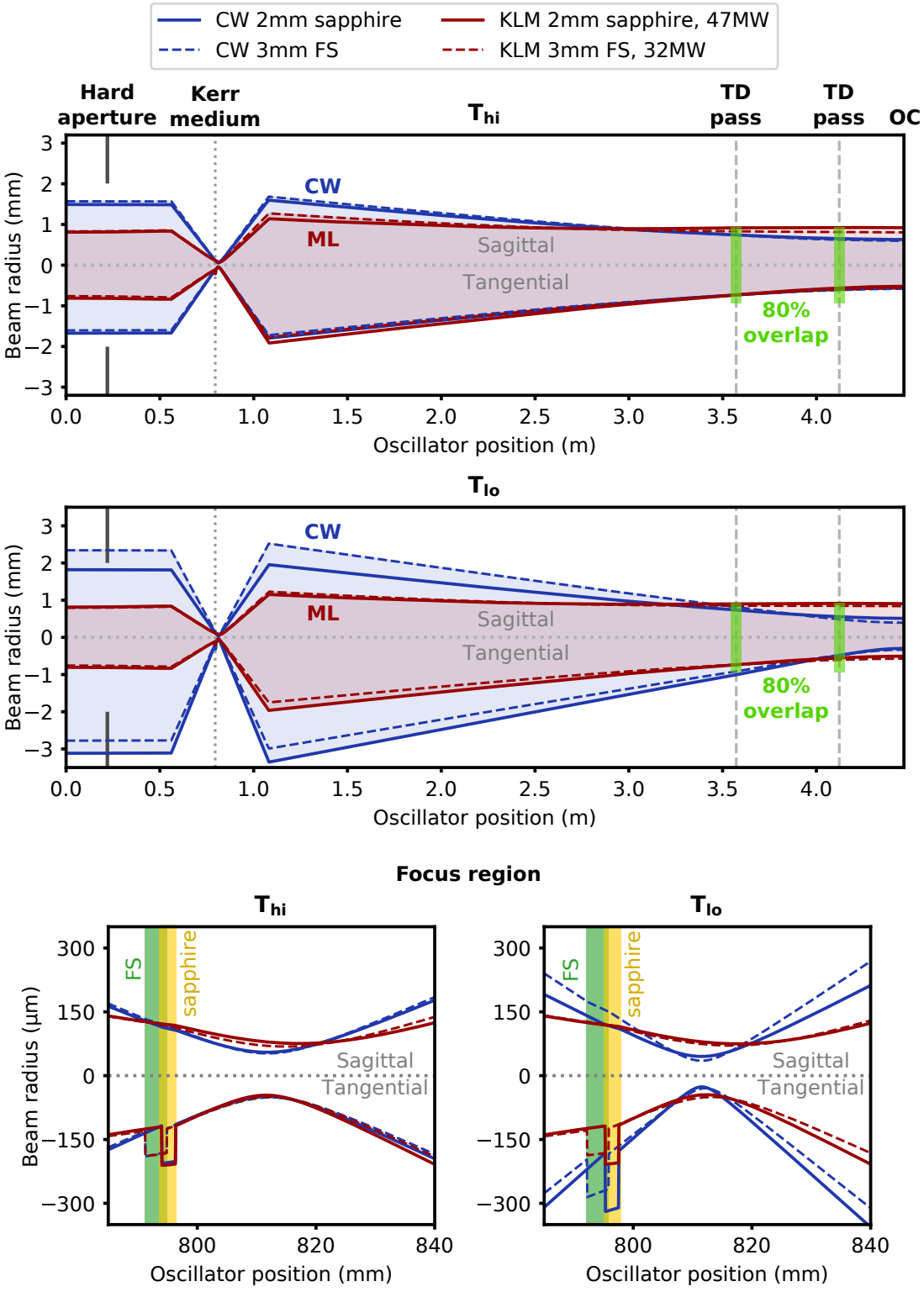

Figure 4.8: Simulated resonators for two different Kerr media. The resonator was tuned to display the same amount of transmission for both media, to emulate the same amount of losses in both simulations. Two tunings of the resonator are shown, $\mathbf{T}_{\mathrm{hi}}$ and $\mathbf{T}_{\mathrm{lo}}$, as described in the text. All four shown ($\mathbf{T}_{\mathrm{hi}}$ and $\mathbf{T}_{\mathrm{lo}}$ for both media) high peak power cases accumulate ~23×10^3 fs^2 of SPM.

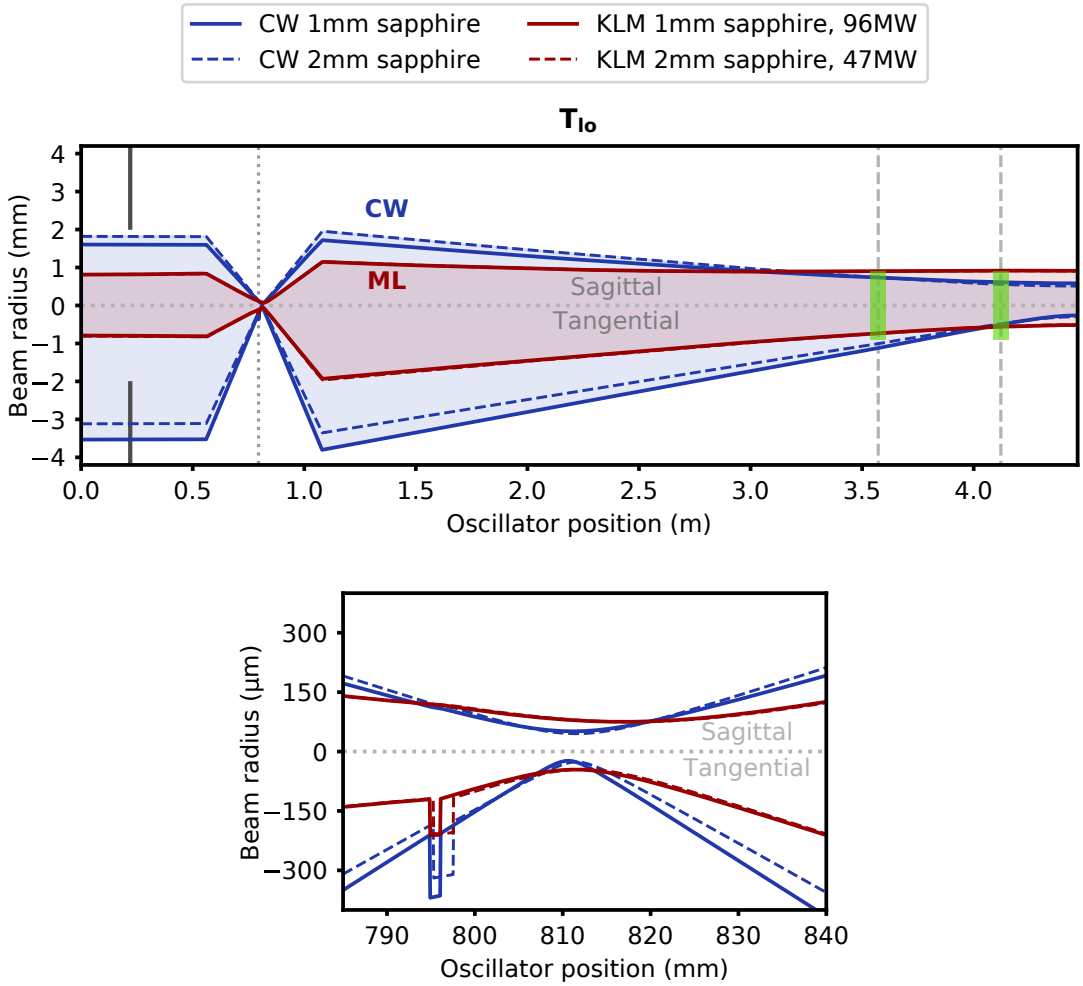

Figure 4.9: Simulated resonators, where the 1 mm sapphire case is equivalent to P_0/P_{crit}=32. In this case the scaling, being the same material follows that one presented in Section 3.2.3, the two high peak power oscillators being indistinguishable.

4.4 Outlook

The above presented resonators using the ray-transfer matrix, and their application to experimentally obtained results show that the formalism, although not taking into account every pertinent light propagation effects, still seem suitable to help on the design of resonators confining peak powers many times above that of catastrophic self-focusing for the materials contained inside of the resonator.

As an example, following the scaling done in Chapter 3 for the plate exchange, the shown 2 mm sapphire was compared to that of a 1 mm sapphire plate, and doubled peak power for $\mathbf{T}_{lo}$. The result can be seen in Figure 4.9.

In this case, as the material is the same, both linear and nonlinear astigmatisms seem to result in the same oscillator. The beam size is also the same in both crystals

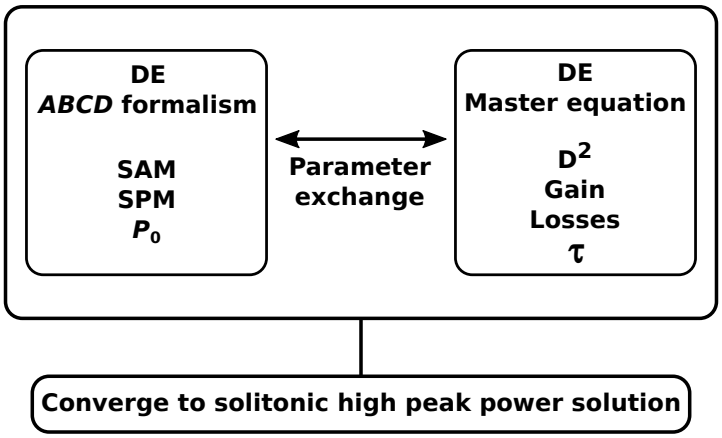

Figure 4.10: Proposal for a computer aided design software for high-peak power laser oscillators.

and as the peak power scaled according to the size scaling, the resulting resonator is practically identical. However, the SPM was not the same in this case: for the higher peak power air now contributes with ~23% of the total nonlinear phase while the one produced in the Kerr medium stayed the same for both cases. This would, in principle, mean that the peak power would be fixed, but the pulse duration would decrease to accommodate for the additionally generated nonlinear phase. In this sense, from this simulations, it would be expected that the pulses would decrease to ~225 fs and the output power would be 125 W for an intracavity average power of ~830 W.

For further scaling, one of the most interesting aspect of this tool is the investigation of resonators which would be much more complex in design. All the simulations shown in this Chapter are for one of the simplest cases of resonator, but it is not far-fetched to think that in the future, for proper scaling, one will need to investigate truly complex resonator geometries to increase the robustness of the operation at high peak powers. Although this would be one of the logical future next steps to the use of this software, it also has many applications on the optimization of already existing oscillators. As an example, it should perform greatly in the optimization of the focus for oscillators driving intracavity high-harmonic generation [122–124].

And lastly, as the formalism shows a moderately good agreement with SPM calculations, it would be of great interest to pair this approach with the mode-locking master equation [60,66]. From the ABCD formalism one can model the losses and gain overlap for a certain peak power, while with the master equation one can find other needed parameters like dispersion and needed gain. Typically, the mode-locking mas-

ter equation is solved recursively, like the original problem of this Chapter, starting with a guess set of parameters and allow the system to slowly converge to a steady state. This type of problem is also very well adapted to a heuristic algorithm like the one shown here, to guess the steady state parameters instead of waiting for a convergence. This also allows to lock a few parameters – for example SPM and SAM – and look only for solutions of the master equation for different pump values and linear losses. A rough proposal of such a design tool is sketched in Figure 4.10. This kind of software could potentially then distinguish the points for which the ABCD resonator has solutions but would not yield master equation results.

5 | Sub-200-fs Yb:LuO KLM thin-disk oscillator

The never ending pursuit of higher average powers while attaining shorter pulses, effectively scaling available peak powers at a certain repetition rate, tends to call for new laser gain media. Host materials promising the same or better mechanical/thermal performance, while surpassing the gain bandwidth of the current widely available high-performers, are then deemed the future of the field.

That is the case of ytterbium doped lutecia (lutetium oxide or Yb:LuO). When compared to YAG, the measured thermal conductivity of the undoped material is already 15% higher, and while increasing doping concentrations in YAG strongly decrease its thermal conductivity, Yb:LuO is mainly unaffected by the amount of ytterbium ions [125]. The density of laser emitting ions in Yb:LuO is also higher than that of YAG (for the same atomic doping percentage) due to the higher density of the material, crystal lattice and unit cell. As an example, in this work an Yb:LuO thin-disk with 3.3 at.% of Yb doping was used, equivalent in cation density to a 6.8 at.% doped Yb:YAG.

In Figure 5.1 the absorption and emission cross sections of Yb:LuO can be compared to those of the well established Yb:YAG. The most striking feature of the lutecia is the prominent zero-phonon absorption peak at 976 nm (2.5 nm FWHM). Additionally, the reduced contrast of the main emission peak, at 1033 nm, increases the gain bandwidth. Thus, Yb:LuO is suitable for the generation of pulses shorter than those supported by YAG. Indeed, the transform limit of the gain bandwidth is ~90 fs, with a FWHM of ~11 nm for full inversion. Notably, the lower emission cross section might be considered a negative feature, as gain is decreased when compared to YAG, but it was proven to not be the case with the demonstration of a Yb:LuO TDL delivering 141 W at 40%

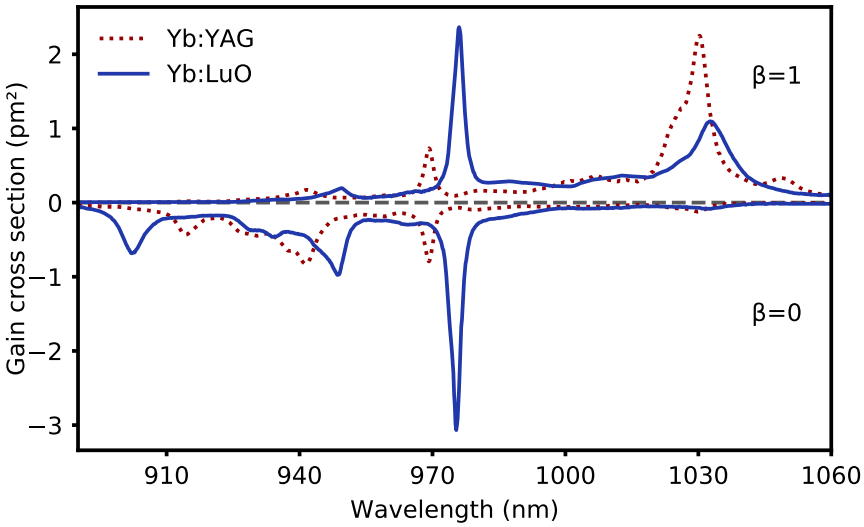

Figure 5.1: Absorption (inversion level β=0) and emission (inversion level β=1) cross section of Yb:LuO Vs. Yb:YAG. The data from Yb:LuO can be found in [126].

optical-to-optical efficiency [41]. This comes as a result from the fact that the absorption and gain cross sections swap roles in Yb:LuO when compared to YAG: it is easier to pump, harder to deplete, while in YAG it is the opposite. This means that thin-disk chambers need less reflections at the ZPL to observe high absorption values.

Oscillators based on Yb:LuO thin disks proved that they can achieve shorter pulses than YAG when using a SESAM to mode-lock the system, demonstrating a pulse duration of 140 fs at 7 W of average power [42]. But despite this fact, the promises of tens of watt of average power at the 100 fs level had not yet been fulfilled. Around the same time, KLM had pushed the notion that Yb:YAG is definitely not limited to the >500 fs range in the high-power regime, a notion which was held for many years as attempted scaling failed to deliver high-power systems under 700 fs [127]. Which lead to attempts at using KLM on Yb:LuO TDLs as well. However, these attempts at mode-locking Yb:LuO TDL through Kerr lensing proved unsuccessful, in that no clean mode-locking was achieved and the pulses were >400 fs [128].

The work presented in this manuscript was meant to unlock the potential of this material in the tens of watt power regime, while achieving close to gain-bandwidth-limit pulses. The following sections show the early and first ever results of a cleanly Kerr-lens mode-locked Yb:LuO thin-disk laser, which were able to meet the state-of-the-art SESAM mode-locked output parameters at the time (140 fs and 7 W). This in itself is already impressive, considering that the obtained results are of a preliminary

nature, before optimization. This showed the potential of this material by confirming that indeed it is possible to use KLM to substitute SESAM without compromises.

Below an overview of the system will be first given, followed by the mode-locked pulse characteristics and finally a small outlook with mentions to some of the difficulties observed while performing these first trials. The work shown below was done as a joint effort between the author and the colleague Bernhard Kreipe. While Bernhard Kreipe focused on the CW characterization, pre-mode-locking troubleshooting and post-scaling, the work shown below was enabled by the author's experience with the Yb:YAG TDL system. All measurements were jointly made unless if stated otherwise. The rest of the characterization done by Bernhard Kreipe will be available soon in his own doctoral thesis [129].

5.1 Disk and oscillator configuration

The disk, as mentioned before, has an atomic doping concentration of 3.3% and is ~240 µm thick. It is soldered onto a copper heat sink and the whole pump chamber is an in-house design. After soldering and polishing, the measured curvatures were 52.6 m and 25.9 m in each orthogonal direction, making it almost flat.

The used pump was an un-stabilized laser diode emitting between 968 nm and 980 nm, with a maximum of 125 W deliverable to the thin-disk pump chamber. For an efficient absorption of the pump, the water cooling temperature had to be manually changed in order to meet the requirements of pumping at the zero-phonon line[1], however the linewidth of the pump diode emission was still >2 nm. The pump was reflected 12 times on the disk for a total absorption length of 24× the thickness of the material and the pumped region had a diameter of approximately 1.6 mm.

A sketch of the oscillator built around the thin-disk can be found in Figure 5.2. The disk, like in the Yb:YAG TDL, was used four times as an active mirror per roundtrip. The smaller pumped region on the thin-disk and the relatively long focusing section (20% or the total distance) meant that a small compromise between both thin-disk passes had to be made, not allowing for both of the reflections to fulfil the 70~80%

[1]The pump diode has in meantime been swapped by a VBG stabilized laser diode, and the performance differences are immense.

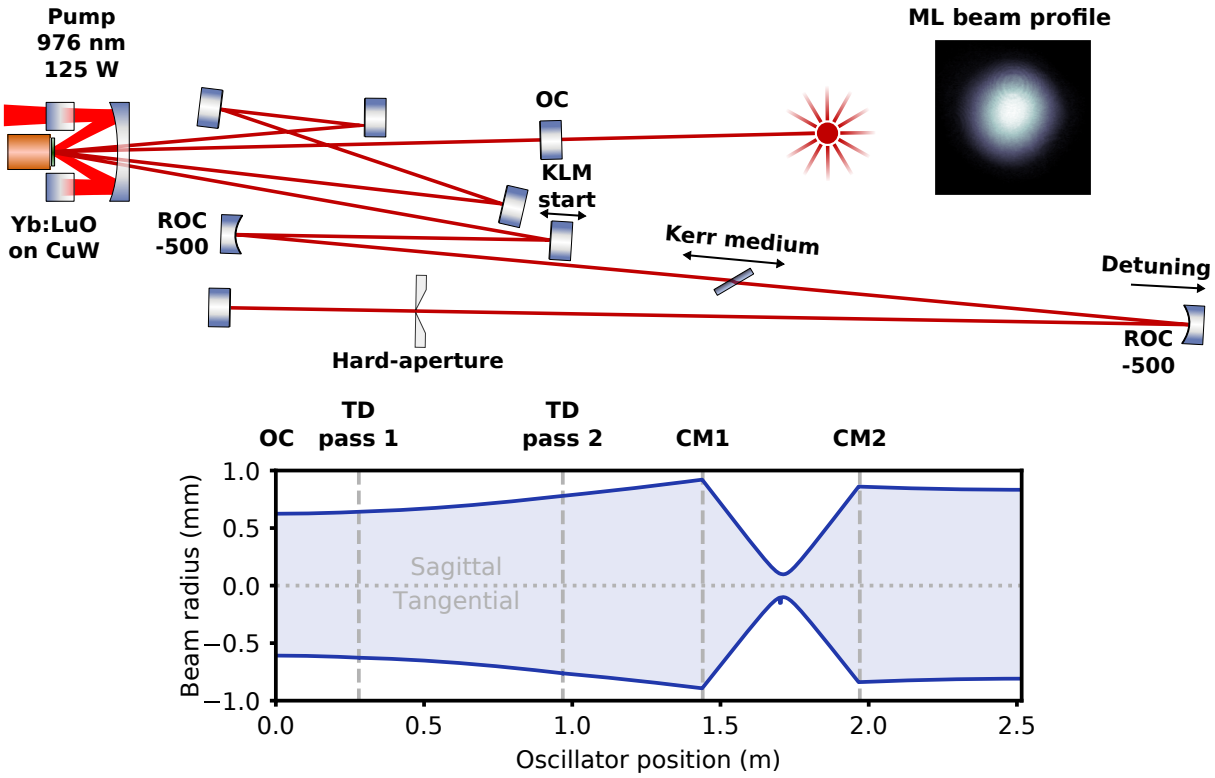

Figure 5.2: Sketch of the Yb:LuO oscillator and an ABCD transfer matrix simulation of the CW operation beam. CM1 and CM2 refer to the curved mirrors.

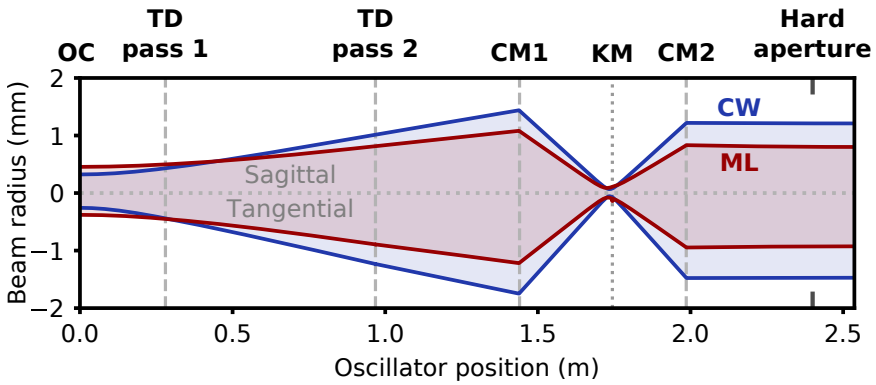

Figure 5.3: Ray-transfer matrix simulations in both transversal planes for the detuned cavity in CW operation and a possible solution to the Kerr lensing action by calculation of a thin-lens based on the peak power (for the 6 W, 160 fs case) and beam radius. There is an intensity transmission difference of 3.5% (16.6% electric field transmission difference) between the ML and the CW with virtually no losses to the ML mode.

of coverage of the pumped region. More information about the whole system: the challenges posed by the pump laser diode, disk source, disk quality, pump chambers, CW performance etc. can be found in the excellent and meticulous work done by my colleague Bernhard Kreipe [129].

5.2 Mode-locking results

The procedures used for the Kerr-lens mode-locking of the system shown above were the same as the ones followed for the Yb:YAG TDL: measurement of the estimated hard-aperture size needed (Figure 3.7) and detuning of the system closer to the stability edge **A** (refer to Chapter 4). An exemplary configuration of the oscillator can be seen in Figure 5.3.

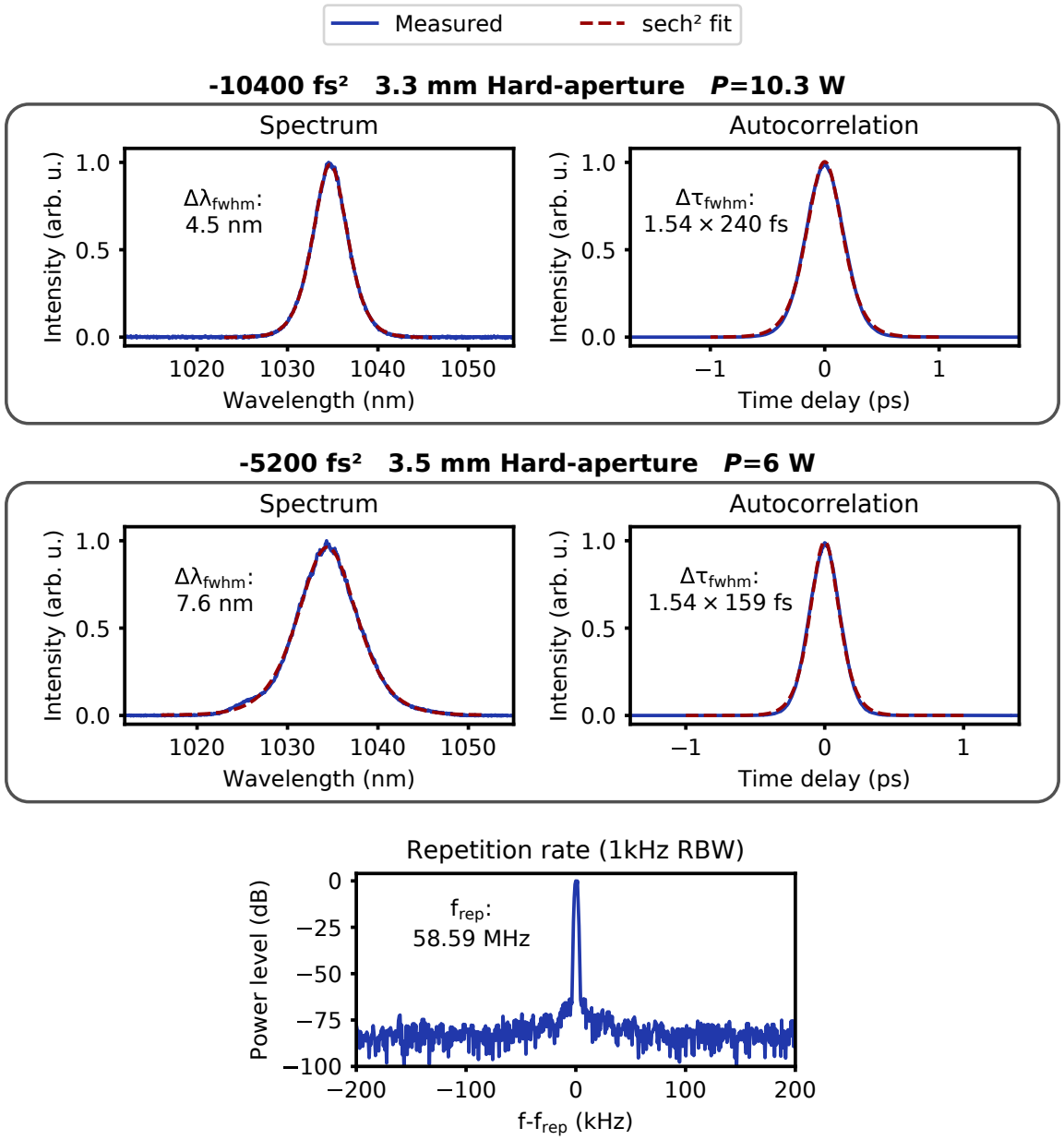

Figure 5.4: Two different Yb:LuO TDL output parameters, for two different sets of oscillator configurations. In both cases the OC had a transmission of 5%. The repetition rate was the same in both cases and the RF spectrum shown is for the shorter 160 fs pulses.

Two key KLM operational points are identified, one targeting a higher output power of 10 W with longer 250 fs pulses, and another at lower 6 W of average power but shorter 160 fs pulses [130]. The parameters used to achieve these were the introduced total negative dispersion of the oscillator and the aperture size. The output parameters are summarized in Figure 5.4.

Both configurations had a repetition rate f_{rep}=58.6 MHz. The higher output power configuration had an intracavity peak power of ~12.6 MW, slightly higher than that of the shorter pulses (at 11 MW), to account for the slightly smaller aperture. The pulses with the 7.6 nm spectrum had a TBP of 0.34. The other configuration displayed the solitonic limit with unchirped pulses. The most impressive aspect of the 160 fs output lies on the fact that, at the time of the measurements, it met the characteristics of the published shortest pulses from Yb:LuO TDLs. Since April 2012 that the results from a SESAM mode-locked system outputting 142 fs pulses at an average power of 7 W with a repetition rate of 64 MHz had been unchallenged [42].

The efficiency and stability, probably owing to the free running pump laser diode and its broad emission bandwidth, were lower than those of the Yb:YAG thin-disk system. The measured integrated RMS noise for the 160 fs case was 0.9% RMS (from 100 Hz to 1 MHz). The measured efficiencies were 10.5% and 7.6% for the 10.3 W and 6 W cases, respectively.

5.3 Further scaling

While working with the system, there were three identified elements which seemed to hinder a better operation of the system, being the pump diode characteristics, the thermal lens induced at the thin disk and the dispersion profile of the negative dispersion mirrors.

The first, the pump module, was the most detrimental. Above 85 W of pump power the emission spectrum broadened considerably as it can be attested by the spectrogram of Figure 5.5. Additionally, change and stabilization of the cooling water temperature also hindered a fast working pace, meaning that different pumping regimes could not be easily explored, creating a bottleneck when trying to ramp up the system.

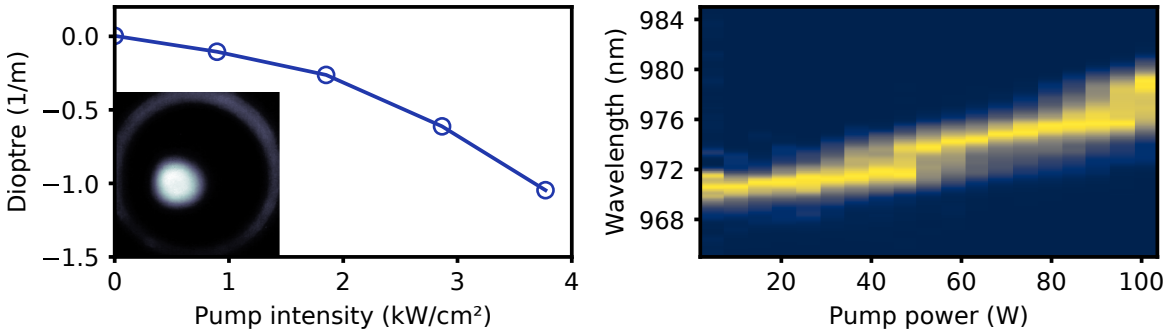

Figure 5.5: Yb:LuO thermal lens and pump diode spectral shift (measured by Jintao Fan and Bernhard Kreipe, respectively). The dioptre changes were measured for pumping with no lasing. The small inset shows a picture of the fluorescence of thin disk (larger circle) and the pumped region during operation. The spectrum was taken from the back reflected pump light at a static water cooling temperature.

In second place comes the thermal lens of the thin disk. The measured dioptre change from the thermal lens of the used disk is considerable, going from a flat and slightly concave disk to display <−100 mm of focal distance at 3.8 kW cm^{-2} (or 76 W of pump power). This creates a multitude of problems in both the design of the oscillator and in its operation. It was quite common to see that if the cooling effect from lasing was not present that the cavity would no longer be stable and allow lasing. Only after reduction of the pump power and subsequent mitigation of the thermal lens would the system emit radiation again. This effect was detrimental when trying to find mode-locking points by perturbation of a cavity mirror. As the loss of lasing performance from this action allowed the thin disk to heat more, it was possible for the thermal lens to go above the maximum dioptre change that still allowed a stable cavity. Moreover, the thermal lens could also act as a mode-locking inhibitor: while building a mode-locked field the lasing becomes more efficient, and consequently there is a strong thermal lens change which might have a counter-effect to that of Kerr lensing. Notwithstanding, this could also be used as a mode-locking reinforcing effect, albeit leading to truncated peak-powers and efficiencies. This effect was not explored in detail, but should be mentioned for future investigations in scaling of such systems.

Lastly, from the different negative dispersion mirrors that were tried, it seemed that the pulse duration and the TBP were highly affected by the design and quality of the coatings, specially by the flatness of the GDD curve at the gain bandwidth. This is explored in more detail in [102, 129]. A strong indication that in order to push the limits of short pulse formation, optimization of all cavity parameters is crucial.

Several of these problems were afterwards addressed by other scientists and the obtained results were impressive. By using a stabilized pump diode and a diamond mounted Yb:LuO, the current state of the art, shortest pulses, have a duration of 35 fs at 1.6 W of average output power (61 MHz) [37]. Additionally, in the sub-100-fs regime 21 W (48 MHz) with 91 fs of pulse duration were also recently demonstrated [38]. It is expected that this material will be able to deliver >100 W at sub-100-fs – maybe even sub-50-fs – in the near future.

5.4 Conclusion

The first cleanly Kerr-lens mode-locked Yb:LuO thin-disk oscillator results were shown [130]. They marked a point where scaling of thin-disk systems based on this gain material seemed to be hindered by the SESAM technology, as it was not possible to unlock outputs using the whole gain bandwidth. By demonstrating that KLM can readily achieve state-of-the-art performance values – 6 W with a duration of 160 fs – also the doors to further scaling were unlocked.

6 f_{CEO} stabilization via depletion modulation of a thin-disk laser oscillator

Frequency combs are nowadays recognized as one of the biggest milestones in spectroscopy [8]. Since the first demonstration that the spacing of the modes of a mode-locked laser are extremely well behaved [131] that harnessing their properties is of great interest [72]. Control of the properties of the electric field exiting an oscillator not only allows the generation of frequency combs but it also opens the doors for applications relying on CEP stability, i.e. isolated attosecond pulse generation [132], pulse synthesis [133] or efficient THz generation [134].

On the one hand, as mentioned in the Introduction, a shift from Ti:sapphire based CPA and OPCPA systems to lasers based on Yb doped media was enabled by technological maturity. Currently, Ti:sapphire are the workhorses of stabilized waveforms. On the other hand, telecommunication-wavelength fibre-lasers took over the commercial comb side. Yb based media intends to become a solid alternative to both these technologies, by overcoming their shortcomings: complexity of Ti:sapphire and their difficult average power scaling problem and on the fibre side their low pulse energy delivery. This shift comes with the need to demonstrate that this route can also cover all the applications enabled by Ti:sapphire lasers and fibre combs. Hence, several CEP stabilization methods have been proposed and shown to work on TDLs, achieving performance levels that rival the best performing systems to date showing an in-loop residual integrated phase-noise below 100 mrad [52].

However, this does not mean that their stabilization is straightforward. Due to the worse noise performance of the highly multimode pump diodes, great care needs to be

taken on the choice of power supplies [48], to decrease as much as possible the intensity noise being coupled to the oscillator, which ultimately affects the φ_{CEO} via the intracavity SPM/self-steepening [135,136]. One of the most attractive points about high-power Yb thin-disk lasers is also one of their downfalls, but is not an insurmountable obstacle as proven several times. Additionally, the water cooling concept of thin-disk lasers is also a strong noise source for the f_{CEO} [48, 50, 53] in TDLs, as it will be demonstrated below. It is also postulated that a deeper mode-locking modulation depth is of great importance when wanting to stabilize the φ_{CEO} of a thin-disk oscillator [48], as it allows the system to be more robust against external interference, not allowing for any kind of background radiation to grow and influence the φ_{CEO}. This is one of the most important aspects of CEP stabilization of TDL systems as it becomes a considerable hurdle for high power SESAM mode-locked systems and in this sense, KLM is an approach that can offer quasi-instantaneous response and high modulation depths without the need to increase the non-saturable losses, as is the case of the current SESAM technologies [67].

Nonetheless, TDL stabilization is possible with outstanding performance when the noise sources are appropriately controlled. So far, most of the reported f_{CEO} stabilized TDLs have achieved it via modulation of the current driving a pump laser diode: either the main pumping laser [47–49] or via a secondary laser diode, dichroically combined with the main pump laser [51]. The single other alternative until this work was the use of an AOM within the oscillator to modulate the losses and effectively lock the f_{CEO} [50,52]. It is foreseeable that in the near future a system using opto-optical modulation, where a SESAM is used as a source of variable reflectivity while being controlled by a CW laser, will be used to stabilize the carrier-envelope offset frequency of a TDL [137].

The above mentioned works all used custom parts, either home-built electronics capable of delivering current to the pump diode in parallel to the main PSU [47–49], in-house coated dichroic mirrors [51] or specialty AOMs [50, 52]. In this Chapter the introduction of a new method for the stabilization of the f_{CEO} and subsequently φ_{CEO} of thin-disk lasers is presented. It is based on the modulation of the gain via depletion, using a small part of the laser itself as the source for modulation. The scheme strips down the requirements for locking to the bare minimum: locking electronics and an

unspecified AOM[1]. The presented work opens up the possibilities for all other laboratories without the capabilities available to other groups to attempt to lock their own lasers and unlock the potential of stabilized waveforms. With that in mind, the Chapter is divided into a detailed description of the whole process needed for a successful lock of the parameter: the self-referenced detection of f_{CEO}, the analysis of its noise behaviour and lastly a description of the locking mechanism and its implementation.

When it comes to the detection of the f_{CEO}, the chosen route to obtain an octave spanning spectrum to feed the f-$2f$ will be given: from nonlinear temporal compression to supercontinuum generation in bulk. After a description of the technical aspects of the f-$2f$ interferometer, the analysis of the free-running noise of the f_{CEO} – for long and short time-scales – will be shown along with the applied methods to mitigate the noise displayed by the system. Finally, the self-contained depletion modulation approach will be described and its performance will be compared to the proven method of pump modulation. A model describing the dynamics is introduced to efficiently compare the observed performance with two other systems from the literature which also use depletion as a gain control parameter [138, 139].

6.1 Self referenced f_{CEO} detection

For the self-referenced detection of the f_{CEO} in an f-$2f$ interferometer, it is fundamental to have access to an octave spanning spectrum. Higher-order offset-frequency-detection interferometers, e.g. $2f$-$3f$ [140], do not require an octave, however they suffer from other limitations, for example the low efficiency of the third-order nonlinearity for an already low-power signal, or, in the case of this system, the need of a high-gain, broad-response-bandwidth UV detector. Below, a detailed account of the planning and implementation of an f-$2f$ setup for the >250 fs pulses of the Yb:YAG TDL is given. It starts with a description of the necessary criteria for the generation of a coherent octave, followed by the steps taken for its generation and ends with the technical details of the built f-$2f$.

[1] Needless to say, it needs to minimally work.

6.1.1 Octave spanning spectrum

In this work, supercontinuum generation (SCG, or white-light generation, WLG) in bulk [141] was the chosen method for the generation of a spectrum which spans more than an octave. Every currently reported technique for the production of a coherent octave, directly from oscillators, requires pulses with durations lower than 150 fs (maximum reported pulse duration 140 fs [42]). To the best of the author's knowledge, all octave spanning spectra from TDL oscillators, mainly for CEP stabilization, were obtained via highly-nonlinear fibres (HNLF) [142]. The necessity of <150 fs pulse durations using this method lies on the fact that due to modulation instabilities there is a direct correlation between a strong loss of spectral coherence of the newly generated supercontinuum and the driving pulse's duration [143]. This can be offset by using all-normal-dispersion (ANDi) fibres, which rely mostly on spectral broadening from SPM rather than from soliton fission [144]. However, in the case of CEP stabilization of TDLs, trying to use a supercontinuum driven by 250 fs pulses directly from the oscillator in an ANDi fibre was attempted by Seidel et al. but also proved fruitless [51]. Some underlying mechanism[2] prevented the detection of an f_{CEO} beating in the f-$2f$ interferometer. Despite not opening the doors to f_{CEO} detection directly from >150 fs pulses, in that same work, while driving the supercontinuum with shorter 25 fs pulses, the ANDi fibre demonstrated a superior robustness to noise in the f_{CEO} detection when compared to HNLF [51].

In this particular work, a choice was made to avoid the use of a highly-nonlinear fibre, as in the case of the output parameters of the oscillator, there is an alternative for the generation of an octave: SCG from bulk. On the one hand, the experimental setup for SCG is considerably easier to align, as HNLF have core sizes typically in the few micrometer range [142]. Moreover, handling of fibres is also prone to specific problems, e.g. cleaving and realignment of damaged and/or contaminated fibres (the air-gap capillaries can be slowly contaminated with water condensation, decreasing guiding capabilities), and in the case of collapsed fibres, it is imperial to avoid damage. On the other hand, white-light from bulk needs to be driven at high peak powers if one intends to have an octave [141]. This means that in contrast to bulk WLG, the use

[2] It is not explicitily mentioned why no signal was found, if a loss of coherence, lack of optical power or some other mechanism.

of HNLF for f_{CEO} detection typically uses a small fraction of the laser power to do so, allowing for greater useful laser power for applications.

Nevertheless, regardless of the route chosen for the generation of an octave, both methods require pulses shorter than those delivered by the oscillator. The case for HNLF was discussed above. For the case of WLG directly from the oscillator, the needed average power to drive the process is prohibitively high, and more information will be given below. To circumvent these problems one would first require a nonlinear compression stage. Although the motivation for such a stage was mainly the f_{CEO} self-referenced detection, its creation is a welcome feature: the generation of a high peak power and short pulse duration beamline is highly beneficial due to its versatility, with a myriad of potential applications. To this end, in the following sections, first, a detailed choice process for the SCG in bulk for f_{CEO} detection is given, which leads to a set of parameters that need to be met. Afterwards, the planning and implementation results of a cost effective nonlinear compression stage meeting the set requirements will be presented.

Filamentation regime

For the onset of SCG in bulk, one needs to be above the threshold for catastrophic self-focusing. As it was explained in Chapter 4, this extreme self-focusing is stopped either at damage of the medium or the creation of a filament [141,145–147]. The spatio-temporal propagation dynamics of a filament are complex and are discussed in detail in References [146–148]. In a general way, as the generation of ionized particles (i.e. plasma in gaseous media, excitation of electrons to the conduction band in dielectrics, etc.) hits a certain density, the refractive index change is able to defocus the light and counteract the self-focusing effect. The two terms then balance each other and a narrow channel for propagation is created: a filament, seen in the sketch of Figure 6.1.

Henceforth, only the planning aspects of the creation of a filament in bulk media will be given, being slightly different from those in liquids or gases. For the initiation of the filament, as one often focuses the pulses into the medium, attention needs to be paid to the used numerical aperture (NA). A too high value usually hinders the generation of the filament, as the beam is focused both from normal diffraction and self-focusing, the achieved intensities at the microscopic spot usually lead to damage

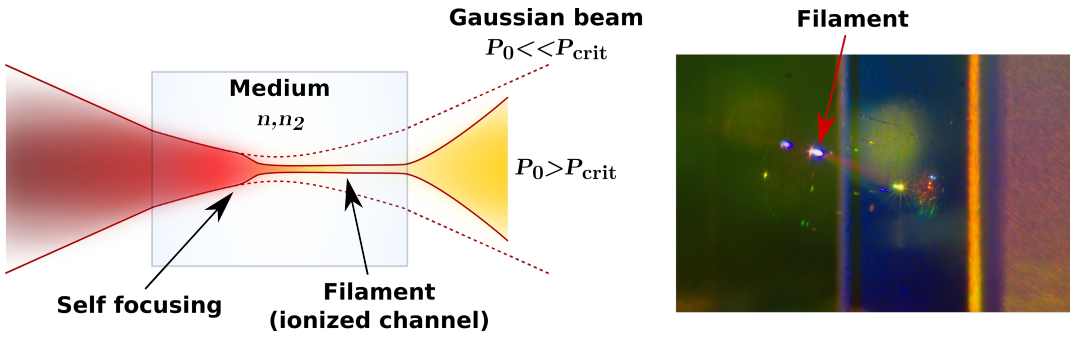

Figure 6.1: Sketch of a filament in bulk. For peak powers above P_{crit} the self-focusing can drive the light above the ionization threshold of the material. In dielectric bulk, this means excitation of electrons to the conduction band. A self-guiding ionized channel is created, allowing for extreme nonlinear phenomena. A photograph of the filament generated in the course of this work is also shown.

of the medium. In [149] it is shown that for NA < 0.08 it is possible to ignite filaments with no damage to the bulk for 60 fs pulses centered at 800 nm and a repetition rate of 1 kHz.

A second important point for consideration when it comes to the application of the generated filament, is the material. Extensive research has been done to quantify and predict the spectral broadening resulting from filamentation [150, 151]. A strong relationship between the material's bandgap and the properties of the emerging spectra has been observed. Firstly, the filamentation, and subsequentely the broadening, can be hindered by materials with bandgaps lower than three times the pump photons. As the process relies heavily on three-photon processes, if the sum of three photons already lies in the conduction band, an increased density of ionized electrons defocusses the light[3]. And secondly, the cut-off of the generated higher frequencies and the total broadening also increase monotonically with the bandgap [151].

Although the sole requirement for the self-referenced f_{CEO} detection is a coherent octave – easily obtainable via SCG in bulk – signal strength is a second important requirement for the stabilization of the carrier-envelope frequency. Thus, with the f-2f detection and stabilization in mind, one needs to consider which wavelength at the shorter end of the spectrum one wants to detect. This automatically determines the longer wavelength as well, one octave below. These two parameters depend both on the material's bandgap. In the case of this work, the higher frequency should lie

[3] Although this assumption is sensible, and earlier attempts failed to go past this point, nowadays, WLG is had up to the two-photon limit, as SPM and self-focusing are driven by two-up, two-down photon processes [152, 153]. But more care needs to be taken [154].

Table 6.1: Material properties for filamentation for various crystals (taken from [141] unless if stated otherwise).

	Sapphire	**YAG**	**KGW**	**YVO_4**
$n_2 \times 10^{-16}$ ($cm^2\,W^{-1}$)	3 [96]	6.9	11 [156]	15
n_0	1.755	1.815 [155]	2.01 [157]	1.96
P_{crit} (MW)	3	1.25	0.78	0.53
Cut-off (nm)	440	470	500	550

close or above the driver's second harmonic at 515 nm, when considering f_{CEO} signal strength. As one needs to generate the second harmonic of the fundamental field for the self-referenced detection, the low energetic content of the newly generated longer wavelengths through filamentation is not suited for efficient SHG. It is best to use part of the initially present driving spectrum, which has a considerably higher power. Leading to a choice of the cut-off around 515 nm, at the minimal bandgap possible – as n_2 and hence P_{crit} are inversely proportional to the material's bandgap – led us to YAG [141]. An overview of other considered materials can be seen in Table 6.1. YAG has a refractive index of n_0 = 1.815 [155] and nonlinear index of n_2 = $6.9 \times 10^{-16}\,cm^2\,W^{-1}$ [141], the critical power for self-focusing is P_{crit} = 1.25 MW. Although KGW also meets the criteria for SCG, it was reported unstable already at 5 MHz of repetition rate with 50 fs pulses [141] and so was deemed not suitable. Yttrium orthovanadate (YVO_4) has the cut-off above our limit and the jump to sapphire would require ~2.5 times the peak power than that needed for YAG.

The TDL having an output peak power close to 3 MW, WLG with pulses straight out of the oscillator should be possible, as there had also been several works showing SCG at multi-MHz repetition rates and longer pulses (<400 fs at 4 MHz [158] and 1.1 ps at 3.3 MHz [159]). The reported damage threshold fluence for 250 fs pulses (centered at 800 nm and a repetition rate of 1 kHz) in undoped YAG is $4\,J\,cm^{-2}$ [160]. This entails a minimal waist size of 3.5 µm at P_{crit}. Reported filament diameters range from 10 µm to 25 µm [141, 151], it seemed that all conditions were met for efficient WLG with no damage. However, even observing low NAs (0.01 to 0.02) resulted in damage around P_{crit} and no stable filament formation. In principle this results from a cumulative process, where the energy deposited by successive pulses can raise the temperature above several important structural material points, e.g. annealing or straining temperatures, although a single pulse is not able to achieve such results [161], ultimately leading to

damage. However, at these high-repetition rates and ultrafast time scales, the underlying mechanisms can be rich in light-matter interaction physics [162–164], and the author believes that more investigations at variable repetition rates and at the onset of damage should be made. But these fall out of the scope of the present work and are just a suggestion for future work.

These first trials at attempting to generate SCG directly from the oscillator were done as the envisioned method for SCG is straightforward to implement, and if successful, would have driven the construction of the f-$2f$ interferometer for the detection of the f_{CEO}. The average power of ~13 W needed to efficiently drive WLG directly from the oscillator was however prohibitively high. The failed attempt at SCG and the high demand for power prompted the design and implementation of a nonlinear compression stage preceding the SCG. This decreases the necessary average power significantly. In the next section the steps for the design and implementation of a cost effective nonlinear compression stage to meet the SCG in YAG will be given.

Nonlinear compression using a large-mode-area fibre

In order to achieve the WLG in YAG yielding the required octave, the ~270 fs pulses from the oscillator needed to first undergo nonlinear spectral broadening, and secondly, linear compression. It is therefore possible to have temporal compression ratios higher than the relative energetic losses, effectively increasing the peak power of the pulses. Although there are several ways of achieving nonlinear spectral broadening (e.g. XPW [165], phase-mismatched SHG [166]) SPM was the chosen nonlinearity [167, 168]. To that end, the pulses were launched into a large-mode-area (LMA) fibre, which is a photonic crystal fibre designed to have a single-mode guiding region larger than that of conventional step-index fibres. This is achieved via the photonic crystal condition, which leads to an endlessly single-mode fibre [169], a fibre which does not display higher-modes. This way, using an LMA fibre, it is possible to generate a broad spectrum via SPM from high peak powers without reaching a single-mode guiding limit.

With the SCG in YAG in mind it was necessary to have a slight head room above P_{crit} after compression so a target of 2 MW was made. Additionally, there was a constraint on the maximal bandwidth that would be possible to linearly compress with the

available compressor unit consisting of SF10 prisms. This limited the transform limit to sub-40-fs when considering the needed dispersion to compensate the introduced nonlinear and linear phases.

An overview of the built setup for the supercontinuum generation can be seen in Figure 6.2 a). All the relevant parts necessary for the generation of the SCG are depicted in the schematic. The LMA-25 fibre has a length of 5.5~6 cm and had a cost of €10.5. This fibre length was chosen via preliminary simulations using a commercial fibre propagation software (Fiberdesk) to achieve our peak power and pulse duration targets. The length is close to the minimum length possible to cleave with the tools available in the laboratory, so the process is also being driven close to the maximum possible obtainable peak power. The spectrally broadened pulse is compressed via the SF10 prism pair and its performance was verified through the d-scan technique [170–172] and the details of the measurement done in this work can be found in the Appendix D. The measured trace and the retrieved spectrogram are found in Figure 6.2 b) c), respectively, the retrieval was done by Dr. Ayhan Tajalli through a differential evolution algorithm. The reconstructed pulse, as seen in Figure 6.2 e), has a duration of 37.5 fs and despite a small 250 fs pre-pulse pedestal, it is close to the transform limit of 37.1 fs. Additionally, in Figure 6.2 d), a simulation solving the pulse propagation through the fibre for the experimental input parameter (150 nJ, 275 fs) is also shown. The numerical algorithm is a simple split-step method implemented in python calculating SPM, self-steepening (using a fixed scalar coefficient) and full spectral propagation through the LMA-25 fibre, loosely based on [59, 142]. The simulation results show and excellent agreement with the observed spectral broadening, and it indicates that there is little to no contribution of the self-steepening, hinting on the reason of the high compressibility of the pulses. Noting the energetic efficiency of 68% and a temporal compression factor of 7.3, there is a five-fold increase in peak power from input to output, enough to drive SCG in YAG with the pulses from the oscillator at lower average powers. A typical visible side of the white-light spectrum driven by a 1030 nm source[4] can be seen in the Figure 6.2 as well.

As concluding remarks to the 2.4 MW pulse used for SCG, it can also be used in many other applications needing short pulses or high peak power. The last half-wave

[4]This was driven by a pulse P_0/P_{crit}~2.5. Data from Sven Kleinert [173]. Thanks!

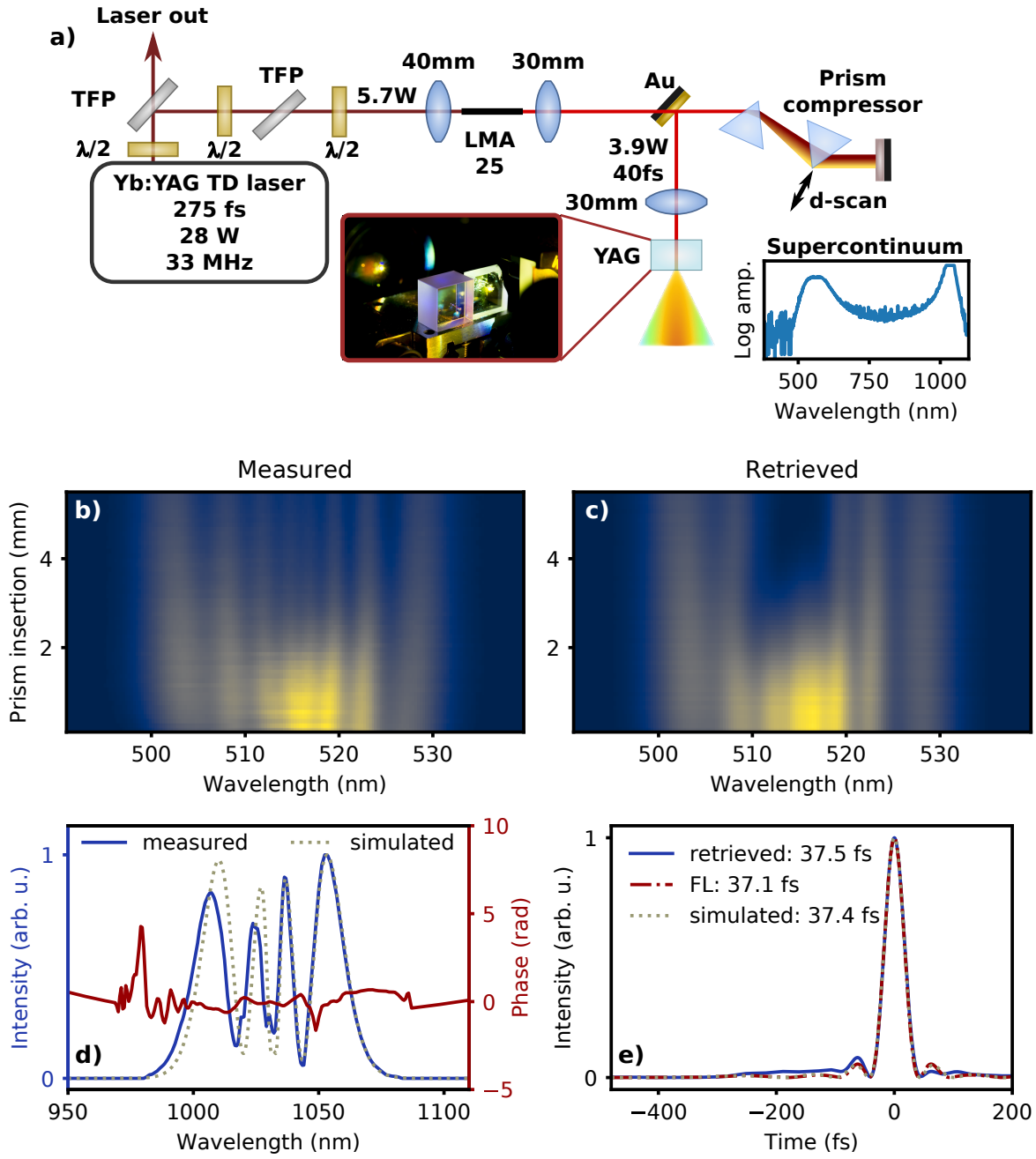

Figure 6.2: Compression and supercontinuum generation. Depicted in a) is a schematic of the setup for the generation of the supercontinuum, based on a nonlinear compression stage. The TFPs are thin-film polarizers and the $\lambda/2$ are half-wave plates. The focal distance of each lens is shown next to it. The visible side of a typical supercontinuum spectrum driven by a 1030 nm pulse in YAG can be seen in the inset (courtesy of Sven Kleinert). The d-scan measurement can be seen in b) along with the retrieval in c). In d) the measured spectrum (blue) along with a simulated broadened spectrum (dotted grey) from launching the pulse into the LMA-25 are shown, the phase from the d-scan retrieval is traced in red. Plotted in e) are the Fourier-limits of the measured spectrum (red dash-dot) and of the simulated nonlinear broadening (grey dotted). The experimental pulse is plotted in solid blue. Details about d-scan and the simulation can be found in the text.

plate serves as an attenuator, as the 8 surfaces of the prism compressor each shed part of the light when it is not p-polarized, allowing to have a tuning knob to the amount of power at the experiment without the need of a broadband half-wave plate and polarizer combo, albeit with a slight rotation of the polarization direction. It is also more than three times the current highest reported peak-power from a KLM TDL outputting pulses with the same duration [37]. Together with the additional >22 W of the oscillator, the possibilities for applications are endless.

6.1.2 f-2f

For the detection of the f_{CEO} the supercontinuum is steered into a Michelson-type interferometer. The setup can be seen in Figure 6.3a). A 45° hot-mirror (ThorLabs M254H45) separates the beam into near-infrared and visible components. The intense NIR, that will be used for frequency doubling and generate the $2f$ signal, is attenuated and temporally delayed using an uncoated fused silica wedge on a translation stage. The visible part passes twice through a zero-order polymer quarter waveplate, and afterwards is recombined with the attenuated NIR through a second pass on the hot-mirror. The used waveplate is insensitive to the incident angle but displays a low damage threshold, which is however tolerable for the broad and low power visible of our f-2f. The 2 nm wide band-pass filter at 560 nm choice was two fold: to relax the WLG conditions, being further from the cut-off wavelength while still being close enough to the second-harmonic of the high-power fundamental; and to circumvent possible losses of coherence or introduced phase noise from amplitude/phase fluctuations at the pump wavelength. The second effect comes from the phase discontinuity typically displayed by SCG at the pump wavelength [174, 175], a consequence of the extreme SPM experienced by the pulse during filamentation [174, 176]. A simulation of the effect can be seen in Figure 6.3b), where the GD of the resulting phase from extreme SPM driven by the compressed spectrum is shown (3 mm propagation in YAG with a diameter of 20 µm and 5 W of average power).

A typical RF spectrum is shown in Figure 6.3c). The f_{CEO} signal is typically 35~40 dB above the noise floor for a resolution bandwidth (RBW) of 100 kHz. High signal-to-noise ratios are desired as locking performance scales with this number [177]. In essence, more photons in the signal allow to better resolve the f_{CEO} sideband, which

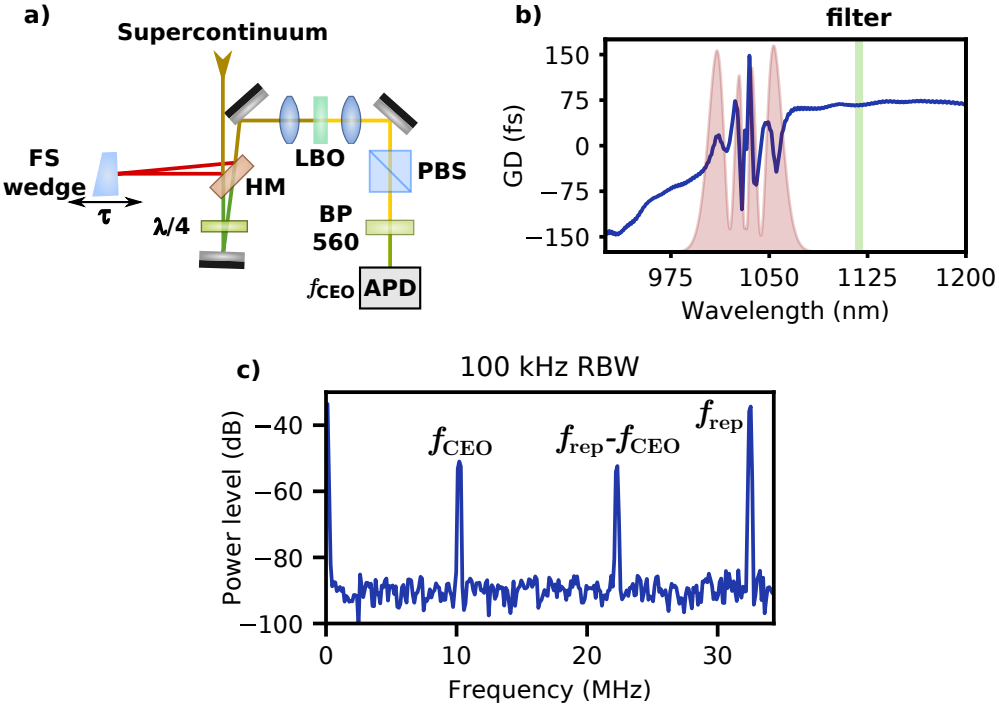

Figure 6.3: f-$2f$ schematic, WLG phase discontinuity and an example of a free-running RF spectrum. In a) the fused silica wedge is mounted on a translation stage and allows the temporal overlap of the two components at the avalanche photodiode (APD). The HM is a hot-mirror (cut-off at 700 nm) and $\lambda/4$ a polymer zero-order quarter-waveplate for 546 nm. The LBO has an unspecified cut and thickness. The polarizing beamsplitter (PBS) is broadband for the visible. BP 560 is a band-pass filter at 560 nm, chosen to relax the WLG conditions and avoid the complicated phase around the driving field. In b) the shaded spectrum drives extreme SPM and the resulting GD is shown with the filter, after SHG of that component, marked. A typical RF spectrum of the APD signal is shown in c).

in turn enables an efficient way of reducing the small noise peaks and shoulder. The detected signal contrast of 40 dB signifies that the shot noise limited lowest possible obtainable integrated phase noise is ~20 mrad [177]. The spectrum always contains a peak corresponding to the f_{CEO} and one corresponding to the $f_{rep} - f_{CEO}$, however, they are usually indistinguishable, i.e. the high frequency peak can be f_{CEO} and the lower one $f_{rep} - f_{CEO}$. This results from the loss of information regarding the spectral phase when going from the electric field to the intensity, both frequencies resulting in the same interference pattern. It is possible to distinguish them though if one introduces dispersion with a known sign into the oscillator and records in which direction the peaks move [178]. In the case of this system, this method is used not to determine which needle is the f_{CEO} but to move it to the locking position. This is accomplished

by translating one wedge of a fused silica wedge pair inserted in the oscillator for this effect.

6.2 f_{CEO} and φ_{CEO} stabilization via depletion modulation

From the detection of the f_{CEO} signal, its stabilization follows. The next section will provide information regarding the phase-lock loop (PLL) and the electronics, its implementation and the challenges posed by this laser.

As seen in Section 2.3, the mismatch between v_p and v_g and the coupled noise does not allow a stable φ_{CEO}. Acting on any oscillator parameter can lead to a shift of one or both of these velocities leading to a different phase slippage condition. The real mechanism behind the changes is still subject of ongoing debates and investigations [136, 179–181]. It is commonly accepted that within an oscillator there is a strong amplitude-to-phase coupling, this can be anywhere from, e.g. SPM, to the phase shift induced by different absorption/emission level in the gain medium (Kramers-Kronig relations). In references [136, 181] a good agreement between the effective time shift created by self-steepening and an f_{CEO} change was shown, when changing the intracavity power. Nonetheless, the full complex intracavity dynamics can lead to shifts of pulse energy, duration, spectrum etc. and knowing beforehand the obtainable f_{CEO} shift for a given shift of another parameter is challenging.

In spite of those challenges, the proposed equations (from the dawn of comb lasers) that govern the phase change from a dispersion change [178] were followed to aid in the design of a pair of wedges to coarsely shift the f_{CEO}. An angle of 4° for ~5 cm fused silica wedges was calculated to be able to achieve control over the whole 33 MHz span of the laser oscillator. Ultimately, the calculation underestimated the achievable shift by their insertion/removal in the oscillator. Although this was not detrimental for the control – less movement was needed for an f_{CEO} shift to the desired location – the introduced losses from the deviations from Brewster's angle resulted in each surface reflecting ~3.5 W, for an approximate total loss of 11~12%. The useful laser average power went down to ~28 W, a 27% reduced power output from the oscillator with no wedges. Besides power loss there were no other detrimental effects on the laser performance, the pulse duration was slightly shorter due to the added dispersion, but

as one can tune the duration via the Kerr medium position, it was possible to achieve the same spectrum and duration.

As stated, the wedges were used for coarse control of the f_{CEO}, for the actual locking, a new method for the stabilization of the f_{CEO} and its phase of TDLs was developed and it will be shown in detail later in this Chapter. However it was necessary to first investigate the high intrinsic f_{CEO} free-running noise displayed by the system.

6.2.1 f_{CEO} free-running noise

Locking of the f_{CEO} of the Yb:YAG ultrafast thin-disk laser proved to be a hard task. This stems mainly from its free-running noise which is much higher than the TDLs presented in the literature [47–52], the sole exception being the Yb:YAG system shown in [48].

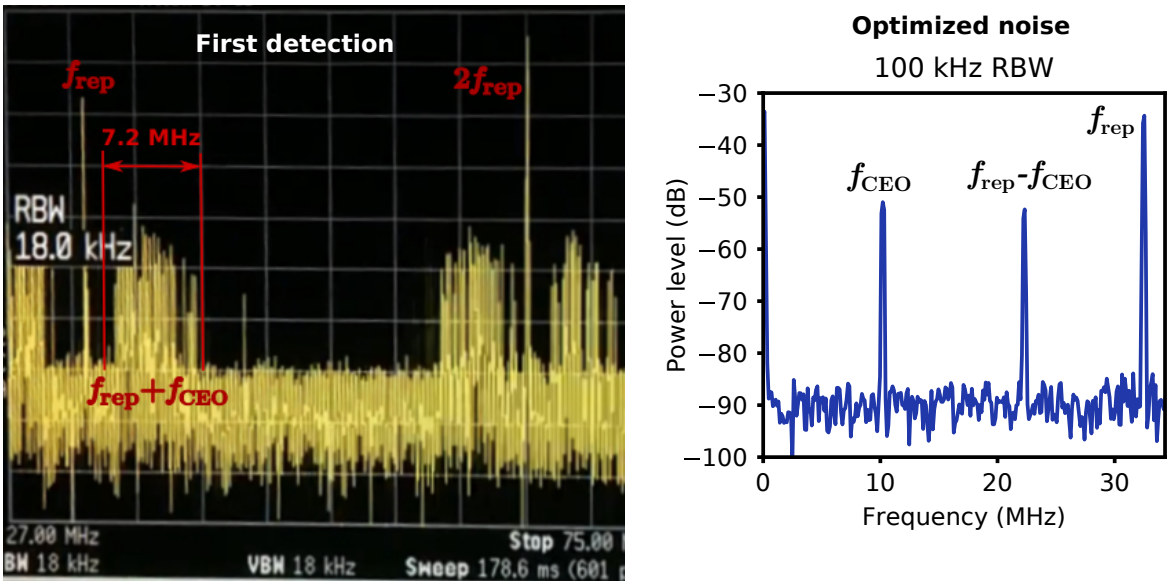

Figure 6.4: First f_{CEO} detection and the free-running noise. Screenshot from video. The sweep time is 178 ms and during this time the f_{CEO} moved in a band of >7 MHz. Next to it is an RF measurement much later, after the noise had been diminished.

In Figure 6.4 a screenshot from a video taken during the first detection of the f_{CEO} shows the immense noise the system had. As shown in Figure 3.6, the noise PSD of the pulse train is low, and such a behaviour was quite surprising. Similar RF sweeps as the ones shown in Figure 6.4 quite often showed bands of more than 9 MHz, and the centre point would also move by extreme amounts. These first measurements suggested that locking the f_{CEO} of this system would be a challenging task, because first, the available

locking electronics had a $\pm 500\,\mathrm{kHz}$ of detection range and secondly, while attempting to change parameters of the oscillator there were no means of having a direct feedback on the noise characteristics, besides f_{CEO} RF spectra measurements, as no method or apparatus could follow such excursions.

Pronin and co-workers argued that the two knobs that allowed to achieve a low enough f_{CEO} noise were the reduction of the water flow on the back of the thin-disk and the position of the Kerr medium [50]. In the case of our system, only the former resulted in an improvement, while the latter was inconclusive. To control the coolant's noise contribution, the water flow was limited from the manufacturer's recommendation of $2.5\,\mathrm{L\,min^{-1}}$ to $0.8\sim1.2\,\mathrm{L\,min^{-1}}$. Additionally, a $9\,\mathrm{kg}$ concrete block fitted with water hoses was used in an attempt to diminish pump vibrations transmitted through the hoses. The flow change made improvements to the excursions, while the concrete block did not seem to have an impact on the noise. After diminishing the flow the f_{CEO} needle seemed to both display a smaller band of 2 to $4\,\mathrm{MHz}$ and the centre point did not move as much as with $2.5\,\mathrm{L\,min^{-1}}$. From the usage of the concrete block, which eliminated transversal vibrational noise, leads to the possible conclusion that mostly longitudinal water noise impacts the f_{CEO} excursions, which is sensible.

Regarding the attempt at moving the Kerr medium, the environmental noise, created from opening the laser box, overshadowed any possible effect. The behaviour of the RF spectra seemed similar after allowing the oscillator to settle, as every time one opens the oscillator box the f_{CEO} needles make excursions in excess of $20\,\mathrm{MHz}$. Attempting to move the cooling finger back and forth, suffered from the same difficulties. Major changes to the cooling finger were not attempted as several projects depend on the healthy status of the oscillator, and to avoid damage to any components, these efforts were kept to a minimum.

None of the mentioned approaches gave evidence of a proper solution the problematic CEP jitter. A reinstallation of a thin disk and cooling finger unit, following the destruction of the previous disk due to a cooling circuit malfunction, allowed for a breakthrough. Everything points to the resistance and pressure drop caused by the cooling finger when mounted behind the thin-disk, which was un-optimal with the previous disk, meaning that the position of the cooling-finger has a major impact on the noise together with the water flow. The author postulates that the carbon-foam

helping with the water spread behind the thin-disk might also influence the noise, creating different kinds of turbulent flow depending on shape, thickness etc. but this was not possible to attest. With the new disk, a more in-depth investigation of the noise was now possible as the f_{CEO} needle no longer displayed high frequency excursions, the RF spectrum looking now like the one presented in Figure 6.3. However, it was still not possible to lock the system, as there were still excursions stronger than the capabilities of the locking loop.

Long time scales

The relationship between the f_{CEO} excursions and the long time laser output amplitude variations were investigated. Before showing analysed traces, the author would like to remind the reader that the excursions of the f_{CEO} needle are not absolute when following noise sources, i.e. as f_{CEO} and f_{rep}-f_{CEO} are not distinguishable, the direction of the movement depends on the state of the oscillator at the time of the measurement and on which needle is sampled. However this fact does not invalidate the general behaviour of the f_{CEO} excursions, and the trace data was treated to reflect the way f_{CEO} and the noise are correlated (if instead the opposite needle had been taken, the excursions would had been mirrored about $f_{rep}/2$). First, an analysis of a free-running trace of both the f_{CEO} peak location and the laser output power fluctuations will be given.

In Figure 6.5a) a snippet of an hour long measurement is shown (the total trace can be seen in the Appendix Figure H.2[5]). In this measurement, the f_{CEO} had regular excursions with 1.1 MHz of amplitude within <30 s. While in the totality of the trace, the peak-to-peak amplitude was 2.7 MHz, following the output power.

The snippet of the trace shown in Figure 6.5b) serves to show that the f_{CEO}, in time scales of ~200 s, trends to move in an opposite fashion to that of the laser output power. This is emphasized by the dashed lines in Figure 6.5b). The trend of the dashed lines was often observed, and they also seem related to abrupt opposite excursions of power and f_{CEO}, marked by the green dashed ellipses. It is important to understand that this is one of the displayed trends. Another trend – in contrast to the one just mentioned – is that of spikes in <20 s, where spikes of the f_{CEO} seem to follow spikes in amplitude. This can be seen both in Figure 6.5b) and c), with the latter showing clearly the syn-

[5]It is insightful in the sense that it shows that the f_{CEO} follows the output power for time scales in the order of hours.

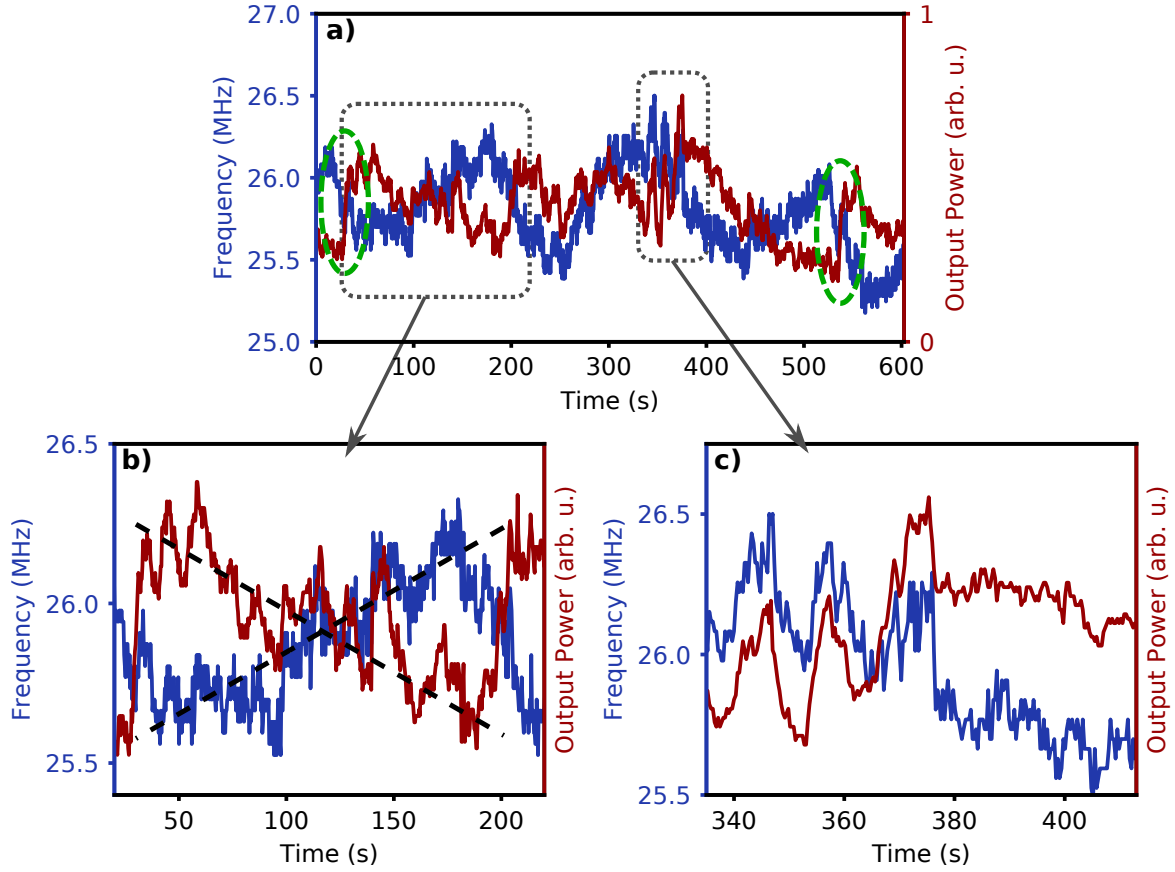

Figure 6.5: Excerpt from a long time series tracking of the f_{CEO} and power fluctuations. In a) a 10 min snippet with two highlighted zones, each plotted in b) and c). Analysis in the text. It must be said that the laser still displayed an RMS amplitude noise of <0.5%.

chronization of the laser output variations with the f_{CEO} excursions. This measurement allows us to conclude that there is a strong relationship between f_{CEO} noise and amplitude noise of the oscillator[6]. However, the f_{CEO} excursions display two contrasting correlations with the amplitude noise of the oscillator: when both of these unknown sources increase the output power of the oscillator, one shifts the f_{CEO} negatively while the other shifts it to higher values. In a simple mathematical (non-physical) analogy:

$$P_{\mathrm{out}} = \langle P_{\mathrm{out}} \rangle + A + B,$$
$$f_{\mathrm{ceo}} = \langle f_{\mathrm{ceo}} \rangle + \alpha - \beta,$$

[6]Several other methods to were used to see their relationship, e.g. correlation plots and Fourier analysis, but ultimately, these were much harder to interpret than just looking at the raw traces, which also give directionality of the correlation.

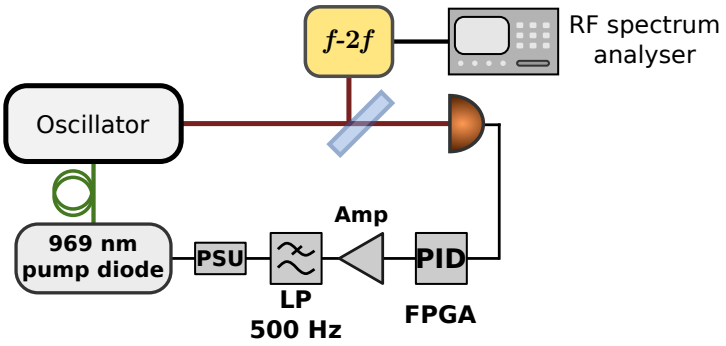

Figure 6.6: Setup for output power stabilization. The LP is a low-pass filter at 500 Hz, the FPGA was used to work as a PID servo to stabilize the output power of the system.

where A and α pertain to one source of noise and B and β to the other. This shows that if the average output power of the oscillator is stabilized (applying $-A-B$ to P_{out} and the system), then one noise source of the f_{CEO} is negated while the other is amplified (in this simple picture $f_{\text{ceo}} = \langle f_{\text{ceo}} \rangle + \alpha - \beta - \alpha - \beta = \langle f_{\text{ceo}} \rangle - 2\beta$).

With that in mind, the system's average output power was stabilized. To that end a field programmable gate array (FPGA) was used to act as a digital proportional-integral-derivative servo as seen in Figure 6.6. The FPGA output signal was amplified and summed to the voltage controlling the output current of the PSU, via a low-noise home-built isolated amplifier chain. The power output was successfully stabilized under our time-dependent detection sensitivity, for frequencies lower than 500 Hz. And indeed, with a constant output power, a noise source of the f_{CEO} was isolated and amplified. The excursions of the f_{CEO} showed a stable saw-tooth shape, as seen in Figure 6.7 b).

The effects of the stabilization are apparent: turning on the PID increased the excursion amplitude from ~1 MHz to ~1.3 MHz, but it also improved the f_{CEO} behaviour, staying locked around 25.8 MHz. It indeed seems that one source of noise had been diminished greatly, while another had been amplified. The saw-tooth signal seemed to be coming from a two-point-control and it was soon noted that the maxima and minima occurred at the same time that the temperature of the water cooling the thin-disk was hitting its maxima and minima as well.

Taking a time-series spectrogram while allowing the water to warm up, while also having the average power stabilized, showed how the water temperature can influence the f_{CEO}. The measured slope with the PID on was 3.4 MHz K^{-1}. As this measurement was taken while stabilization was on, this is in principle a worst case scenario.

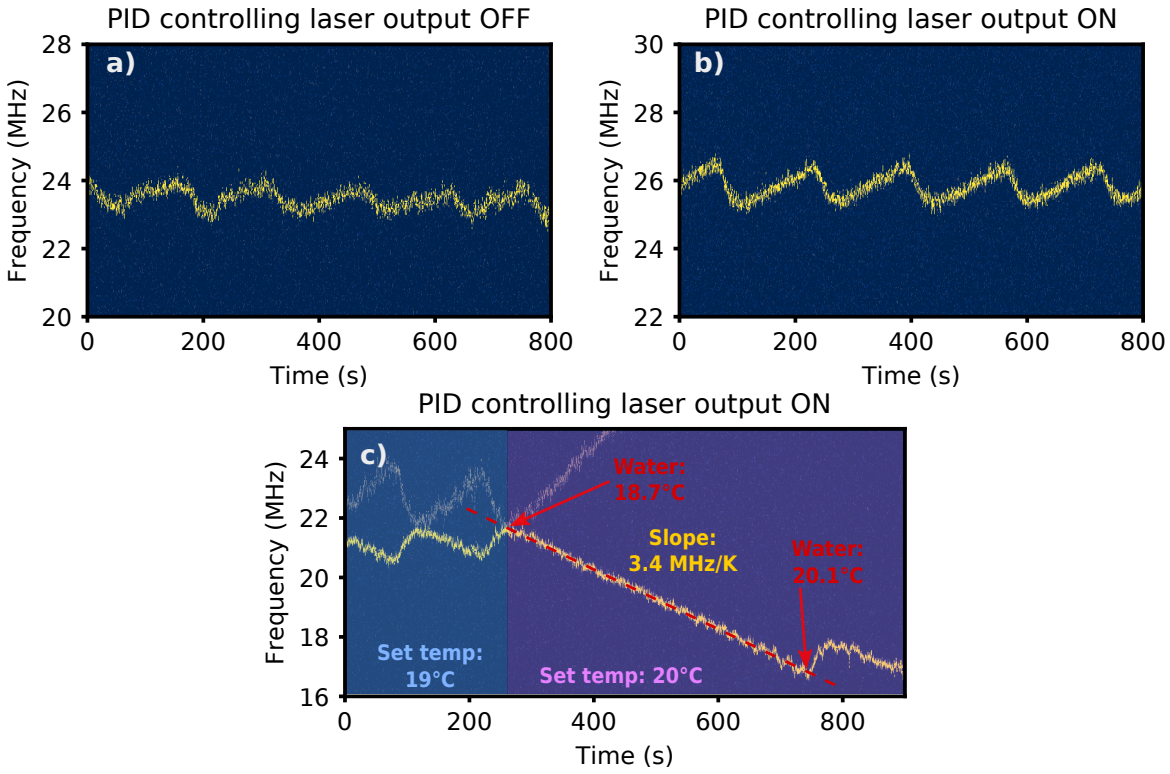

Figure 6.7: f_{CEO} drifts a) with and b) without an applied PID servo to the output power. In c) a plot illustrating the thin-disk water cooling temperature dependence of the excursions. The fainter signal in c) is the nonlinear mixing term between all f_{CEO} needles and its slope is exactly negative two times that of the slope of the f_{CEO} as it will be explained in Section 6.2.2.

Nonetheless, this meant that it is of utmost importance to have water temperature drifts under control, in the case of this system <0.3 K of amplitude just to be within the locking electronics range. But for long term stability and ensuring that there is no saturation of the integral components in the stabilization electronics/feedback, the temperature amplitude has to be even more confined. In our case, we decided to have a target of <0.1 K and with our custom home-built water-temperature-control chamber the temperature was usually stabilized to less than 50 mK of peak-to-peak amplitude (typically 30 mK). The chamber was also designed to try to minimize mechanical noise by having the water travel through a spiral. The effectiveness of this spiral was not possible to attest. After implementation of this chamber, it was possible to lock the f_{CEO} reliably, as will be demonstrated later in this Chapter.

On a curious note, through the whole process of designing, building and implementing the water-cooling solution, it was found out that the thin-disk needs far less cooling than usually supplied. For the hundreds of watt of pump power usually used

in these systems, it is easy to find water-cooling systems capable of several kW of heat management. Although operated 1~2 °C above room temperature, at an output of 30 W and pumped by >100 W, the thin disk water was stabilized by applying a mere 5 to 7 W of cooling through the Peltier element, and this is a cooling system which is definitely not fully optimized[7]. Designs using thermo-electric coupling (TEC) as the sole cooling method for the thin disk should be highly desirable for CEP stabilization, and in light of the low cooling power needed, its not necessary to sacrifice a lot of average power. The noise will be much better managed as there are no mechanical vibrations from turbulent water flow and TECs can achieve stabilities in the tens of mK. It is quite interesting to see that Dausinger+Giesen GmbH now offers thin-disk chambers with TEC cooled disks and also mounted on solid copper bodies which allow for low-noise laminar water flow in a much larger area, instead of a water shower. It would be interesting to investigate the gains in noise performance from these chambers.

Short time scales

For observation times ~200 ms the observed noise was considerable. As shown above, for the first f_{CEO} measurements, excursions of up to 9 MHz were seen in this short span of time. Notwithstanding, after all the efforts to manage the noise coming from the water temperature and water mechanical noise, the behaviour improved considerably and it was possible to stabilize the f_{CEO}, albeit with a performance limited by the free-running high-frequency noise.

The frequency noise power spectral density (FN PSD) of the free-running laser for an observation time of 170 ms can be seen in Figure 6.8. All FN PSD of the f_{CEO} where taken using the method described in [51] and the method is summarized in the Appendix E. It is based on a time sampling of the f_{CEO} signal and then process it to derive the FN PSD. This measurement technique has several advantages and drawbacks to traditional digital phase detection (DPD) analysis. As pros, with this measurement technique it is possible to analyse the fast moving f_{CEO} signal without a specialized RF noise analyser, there is a precise measurement of the instantaneous f_{CEO} and it is insensitive to signal amplitude modulations, meaning that only the phase and its noise are being targeted. The disadvantages lie on the lack of instantaneous feedback to the

[7] It also falls in place with the zero-phonon line pumping, at 100 W, 6 W of heat would be generated.

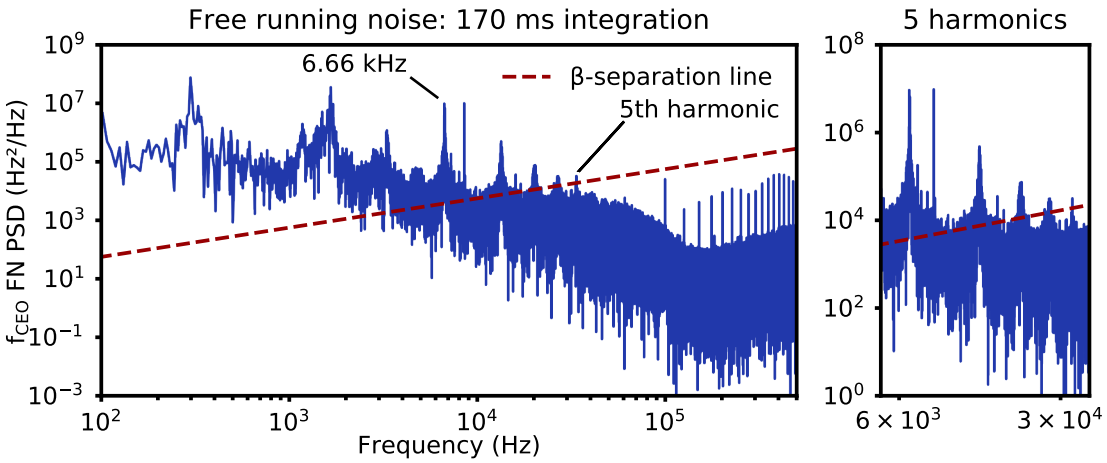

Figure 6.8: Frequency noise power spectral density (FN PSD) of the free running f_{CEO}. Marked is the 6.66 kHz peak and its 5th harmonic, which is the last frequency above the β-separation line. The harmonics can be seen again on the right, in narrower plot of the FN PSD.

user and an overestimation of the low frequency noise due to the limited sampling (the reason why all plots are truncated to 100 Hz).

In the plot, the FN PSD is compared to the β-separation line [182]. The line separates noise regions which contribute to the linewidth, i.e. frequencies above the line, from those contributing mainly to the spectral wings. In essence, frequencies below the β-separation line are typically attenuated by more than 30 dB when compared to the carrier. The line helps to visualize the necessary bandwidth for a feedback loop, as it shows up to which frequencies the feedback loop must be effective for a tight, low noise lock: it needs to target all frequencies above the line. Analysis of the plot reveals that an effective bandwidth in excess of 33 kHz is required to tightly lock the f_{CEO} as the 5th harmonic of a strong noise peak at 6.66 kHz is the last frequency above the β-separation line. This noise peak and its harmonics appear several times in the literature. They are present on references [48, 49, 52]. Although they are not distinguishable in references [50, 51], there is still a pronounced noise contribution close to 7 kHz. The true reason for these peaks was not investigated, but it was proposed by Emaury and co-workers in [48] that they originate from the power supply unit, as they are clearly visible in the RIN of the output of the pump laser diode. In Seidel's PhD studies [135], however, both the PSU and diode output intensity noises do not display such spikes but then they appear in the mode-locked intensity noise spectrum. The used PSUs by Emaury, Seidel and this work are from Delta Elektronika (but maybe different mod-

els). Furthermore, in the work of Hakobyan et al. [183], regarding the generation of a GHz comb, investigations of the PSU noise show similar peaks and the implementation of a low-pass RC filter between the PSU and pump diode seems to kill all noise peaks from the pump diode's intensity noise, but then again the ~6 kHz spike appears in the f_{CEO} noise spectral density, albeit with no harmonics. In the case of our system an RC filter was also built in but the effect seems less pronounced. The origin of these peaks is an open question for the author, if it is just an alignment issue, or perhaps a multimode beating originating from the back reflected pump light from the thin-disk chamber, or truly electrical noise coupled to the pump to which the f_{CEO} is extremely sensitive to. The truth is that these peaks drive the noise from the flicker- and highly attenuated noise (the background clearly goes under the β-separation line at ~10 kHz, like the intensity noise shown in Figure 3.6) to higher values in the case of our system.

Additionally, to effectively lock the f_{CEO}, not only the bandwidth is needed, but sufficient amplitude as well. The standard deviation of the signal measured in the free running PN PSD (Figure 6.8) is 53.4 kHz. If we consider that for an effective lock a minimum of 5 to 6-σ need to be compensated, then we get ~275 kHz of amplitude needed (99% interval or 5.15-σ). To understand the implications of this, it is perhaps simpler to consider the case of a feedback loop with an amplitude limited to the standard deviation. In this case there is a ~30% chance that the instantaneous f_{CEO} signal will lie outside the amplitude control range, losing the lock, without guarantees of being in pull reach of the feedback control afterwards. Hence the choice of at least 5.15-σ for the amplitude when considering the standard deviation of the signal.

The analysis of the short-term noise gives then an insight on the needed frequency and amplitude response of the feedback mechanism. For an effective tight lock, where all noise components are pulled under the β-separation line the feedback system will require a minimum bandwidth of 33 kHz and an f_{CEO} amplitude change of >275 kHz. In the following section a detailed look on the electronics, f_{CEO} actuation modes and phase-lock loops used to bring most of the noise below the β-separation line will be given, along with a discussion of the performance.

6.2.2 In loop f_{CEO} and φ_{CEO} locking

To be able to lock the f_{CEO} via a feedback scheme, one needs to measure the error between the desired and current operation points and then actuate on the system to diminish this error in a timely manner. The measurement is given by feeding the f-$2f$ signal along with a reference to a digital phase detector. The actuation on the system, as mentioned before, can be done in many ways. In the case of this work a novel scheme was developed as there was no other means to lock the f_{CEO} without specialized equipment. The method is presented below followed by the discussion of its performance.

Gain control via depletion

By exploiting stimulated emission driven by a small part of the laser output it is possible to shift the total gain of the laser medium. Accurate control is achieved by modulating the amplitude of this small portion of the output (the control beam) via an AOM and shining it on the pumped region. This way the gain can be increased (decreased) by decreasing (increasing) the power of the control beam. As a result, the intracavity pulse train will also have its amplitude modulated and the f_{CEO} position shifts accordingly. To achieve this, the large solid angle over which the thin-disk can be accessed was exploited. The plane of incidence of the control beam is not coplanar with the plane where the laser was built, in a similar fashion to the pump's path, which impinges the thin-disk from many non-coplanar incidence planes. The pumped region is easily seen and so alignment is rather straightforward (see Figure 6.9 a)).

The effects of a single pass of the control beam on the f_{CEO} and amplitude of the laser can be seen in Figure 6.9 along with a schematic of the setup. The obtained effective bandwidth of 10 kHz, marked in Figure 6.9 c) is not meeting the sufficient requirements of 33 kHz for a tight lock of the f_{CEO}. However it seems sufficient to compensate for most of the flicker noise from the oscillator. To measure the effects of the control beam on the f_{CEO} a square wave was fed to the AOM, modulating the beam between 0 and 3 W. As the f_{CEO} jumped between two values a slow RF measurement aliases the signal, capturing both frequencies in a single sweep. The change of the f_{CEO} for this case can be seen in Figure 6.9 d) and from works showing that the effect is linear [48, 183], a change of 340 kHz/W per pass on the thin-disk is expected. The

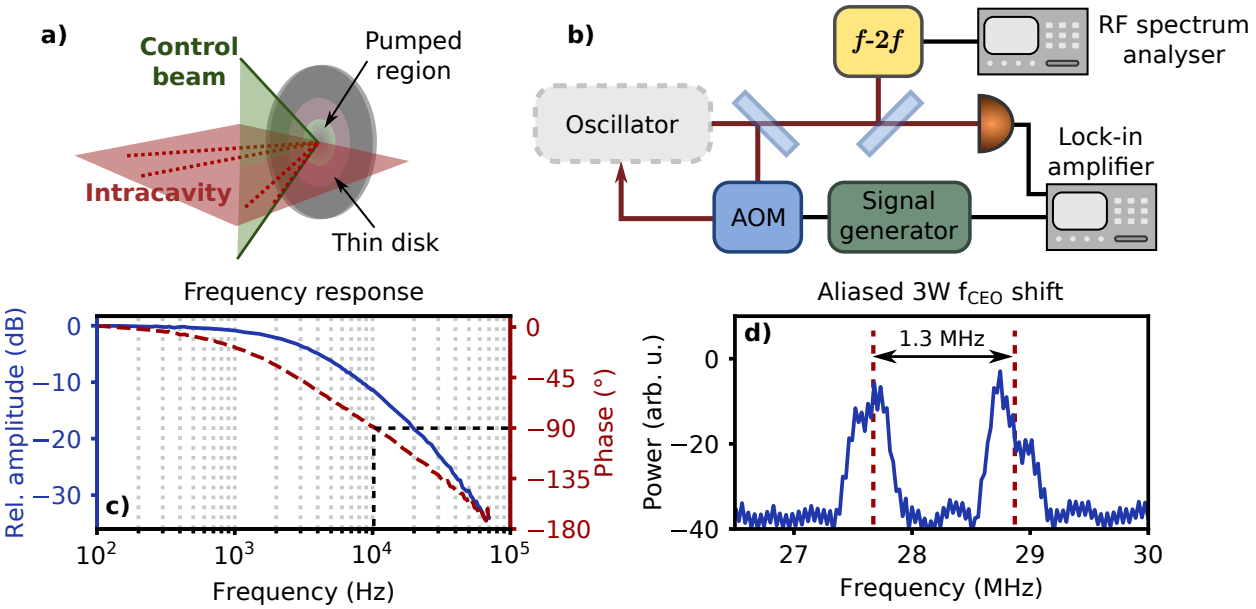

Figure 6.9: A schematic of the depletion control beam can be seen in a), where the two perpendicular planes, one of the laser oscillator and the other used for the control of the gain are shown. In b) a schematic of the measurements is presented, from the lock-in one obtains c), the bode plot of the response of the laser's amplitude to a signal applied to the AOM where the zero phase was set to a modulation of 20 Hz. The effective modulation bandwidth is shown by the 90° lag point. To obtain d), a low frequency square function was modulating the control beam by 3 W, and the RF measurement was aliased, a sweep time longer than the period of the square modulation. This was done in a single pass and so the change of f_{CEO} is 1.3 MHz/3 W~340 kHz/W per pass.

measured shift is not as strong as the reported change for pump modulation [51], but that was to be expected as a single pass through the gain medium has little effect due to the thickness of the crystal.

Although using for example a single pass of the control beam with an AOM that can achieve 100% diffraction efficiency running at 1±1 W should be, in theory, enough to lock the system, it leaves no leeway to pull the f_{CEO} and the integral term of the servo would rapidly reach saturation. So a decision needed to be made regarding the total amplitude on which the feedback system can act on the f_{CEO}. Ultimately, a target of at least ±500 kHz of peak-to-peak f_{CEO} shift, to cover all possible states, was made. With the beam diameter through the AOM fixed at 1.3 mm, chosen based on the AOM's manufacturer rating of a maximum bandwidth of 1.1 MHz for this beam size, the incident power was capped at 3 W. The limit was imposed by wanting to avoid non-linearities (<1 mrad cumulative phase) from the propagation through the 42 mm long quartz AOM. Lastly, to ensure that the AOM is working in a linear slope of diffraction

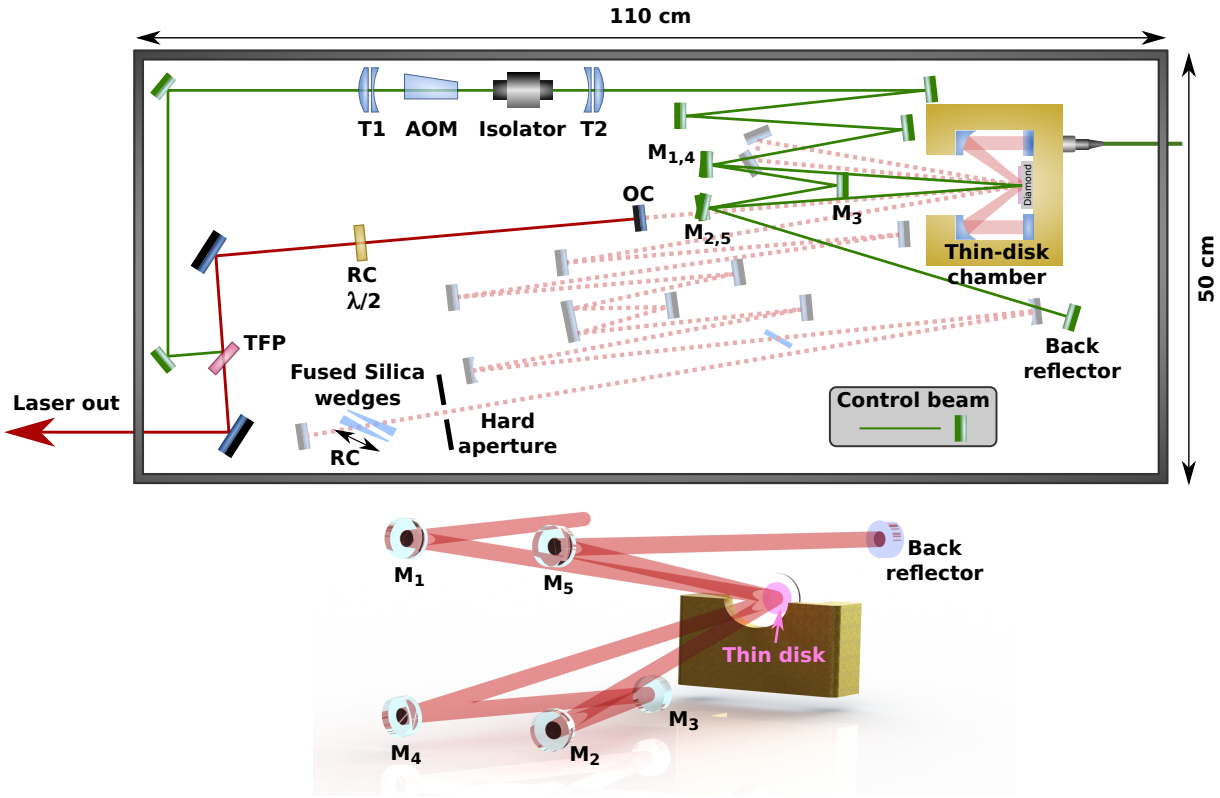

Figure 6.10: Schematic of the laser box (not to scale) including the oscillator and the control beam passing four times on the thin-disk. The portion used to control the gain and hence the f_{CEO} is drawn in green. Both the half-wave plate and one of the fused silica wedges are remote controlled (RC). T1 and T2 are Galilean telescopes to manage beam sizes through the apertures of the AOM and isolator and subsequently image the correct beam size for shining on the gain region of the thin-disk. The HR mirrors used in the folding are labelled through their order as subscripts of M. In the bottom render the same mirror labels are used, to have a better understanding of how the laser beam was folded on the gain region.

efficiency, the working point with 3 W incident power should be at 1.5±0.5 W. With the control beam parameters fixed, to achieve the targeted f_{CEO} shift it was then necessary to fold the control beam on the thin disk. At least 3 reflections would be needed, however the geometrical constraints within the oscillator make it easier to have 2 incidences on the thin disk and then back reflecting the beam for a total of 4 reflections.

Control beam with four passes on the thin disk

To ensure a sufficient modulation amplitude affecting the oscillator gain dynamics, the control beam was shone four times on the gain region: two in the forward direction and then a back reflecting mirror doubles the passes, also allowing to extrapolate the scalability of the approach.

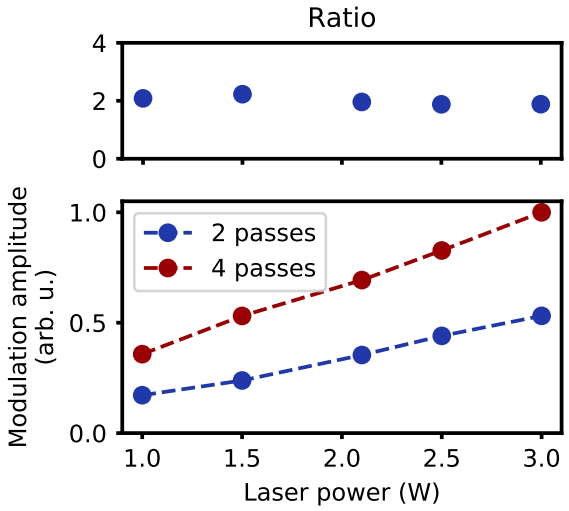

Figure 6.11: Effect of control beam for different power levels and passes. In the top the ratio between four and two passes for each measurement is shown. The deviation from the expected value of two can be explained by power measurement inaccuracies.

Its implementation is shown in Figure 6.10. While for the single pass only one plane was used, the four passes used two other planes of folding. The folding could have also been accomplished with 45° HR mirrors replacing mirrors $M_{2,5}$. The telescope T2 guarantees that the whole pumped region is covered, to ensure a more uniform depletion of the disk. Here one can see where the wedges for the coarse control of the f_{CEO} were installed and they were made to be remote controlled in order to prevent the necessity of opening the laser box for their adjustment. The effects of such a multipass approach were investigated to ensure that the mode-locking would not be affected and that the concept is scalable. Investigation of the behaviour of the output amplitude of the laser was recorded for several power settings of the control beam up to 3 W for both cases of two (blocked back reflector) and four passes. Lock-in detection was done at 100 Hz, still in the region without phase lag, and the amplitudes for the different cases compared. The measurements presented in Figure 6.11 showcase the linearity of the control, which was to be expected due to the high saturation energy of thin-disk gain media.

Both slopes are seemingly linear. Dividing the amplitude of the four passes by the ones obtained for two passes confirms the linear gain of amplitude by staying approximately at 2. It is safe to assume that at this power levels and number of passes one retains linearity and no saturation effects are present. Up to the power setting at which

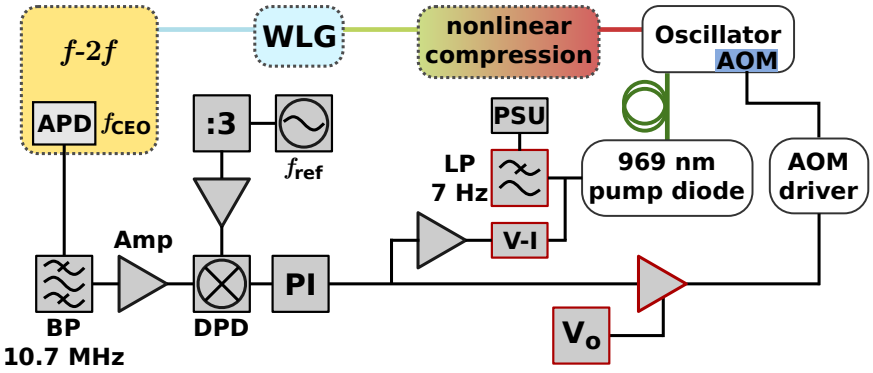

Figure 6.12: Schematic of the loop used to lock the f_{CEO} with a focus on the electronics. The components with a red border are home-built components. APD: avalanche photodiode; BP: band-pass filter; AMP: amplifier; DPD: digital phase detector; PI: proportional-integral amplifier; V-I: voltage-to-current converter; LP: low-pass filter; PSU: power supply unit; V_o: low-noise offset voltage generator.

3 W using 4 passes were shone on the disk, no disturbance of the mode-locking was observed. In this case, the effective 12 W amount to just 1.6% of the intracavity power. Trusting the linear transfer of laser amplitude modulation to the f_{CEO} [48, 181], a total of $\pm$2 MHz of frequency shift would be achieved for a 100% modulation depth using 3 W and four passes. But as stated above, these would not be the true totals, as locking will only be efficient around a linear diffraction slope and for the used settings at least $\pm$680 kHz of f_{CEO} shift are expected, which meets the set requirements of 500 kHz.

With an appropriate feedback mechanism in place, the last step needed to lock the φ_{CEO} is the implementation of the phase-lock loop electronics tying the f-2f signal back to the oscillator. The next sections will present the electronics and the locking results.

Phase-lock loop and electronics

The main electronics for locking of the f_{CEO} used in this work are from MenloSystems. An overview of all the electronics involved in the locking are shown in Figure 6.12 and an introduction to the digitally assisted PLL is given in the Appendix F.

Originally, it was planned to lock the system to a third of the repetition rate f_{rep}. This way every third pulse would display exactly the same CEP, which can be of use for applications sensitive to the carrier-envelope phase. However, while measuring the f_{CEO}, it was noted that the beat frequency between all f_{CEO} needles (the first low frequency ones and all the subsequent needles offset by their f_{rep} harmonics) was detri-

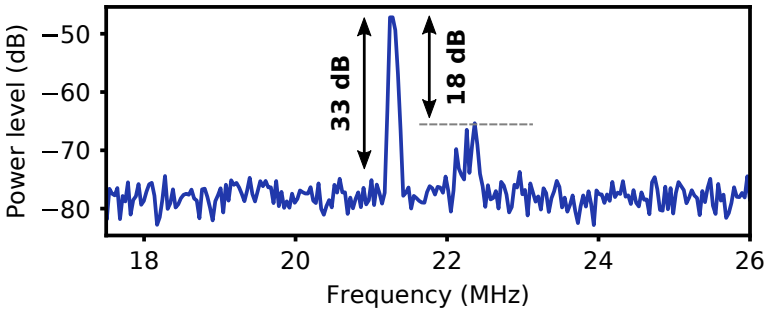

Figure 6.13: Example of the f_{CEO} high term mixing. Although the signal is ~30 dB above the noise floor, the mixing term peak is only 18 dB below the maximum of the f_{CEO}.

mental to the performance of the system. It is easy to show that the beat note between all these frequencies is at one third of the repetition rate if we allow f_{CEO}=$f_{\mathrm{rep}}/3$:

$$\begin{aligned} f_{\mathrm{beat}} &= \sum_n \Big[\big((n+1)f_{\mathrm{rep}} - f_{\mathrm{CEO}}\big) - \big(nf_{\mathrm{rep}} + f_{\mathrm{CEO}}\big)\Big] \\ &= f_{\mathrm{rep}} - 2f_{\mathrm{CEO}} \end{aligned}$$

This meant that a broad noise pedestal is created at the mixing frequency, as besides the factor of two, the higher harmonic needles have the added phase noise of their f_{rep} harmonic, and this phase noise scales with the square of the harmonic. This effect was already seen in Figure 6.7, and an exemplifying RF spectrum can be seen in Figure 6.13. The detrimental aspects to the noise can also be found in the Appendix (Figure H.1) of a plot of the frequency noise power spectral density with the added noise bump. Despite being possible to mitigate and even completely eliminate this higher-order mixing term, by lowering the amplification of the APD, doing so meant being below the signal strength needed for an accurate DPD detection. Nonetheless, the divide-by-three electronic module to set f_{ref}=$f_{\mathrm{rep}}/3$ was still used, as the output was a square wave, beneficial for the digital counting in the DPD.

To close the loop and lock the offset frequency, the error signal was amplified through a proportional-integral (PI) circuit and applied to the oscillator as a feedback in three ways: pump modulation, gain modulation via depletion and both simultaneously. The former was achieved via a voltage-to-current converter (V-I), designed and built by the scientific team of the Laboratoire Temps-Fréquence from the University of

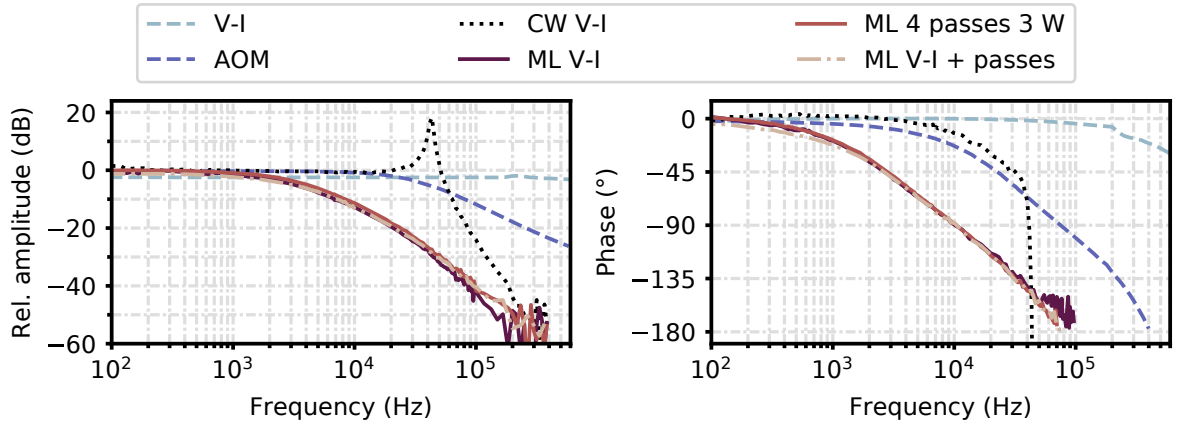

Figure 6.14: Measured frequency responses of the various elements used to lock the f_{CEO}. The dashed lines correspond to signals not measured from the oscillator: the response of the AOM (light blue) detected through the control beam and that of the current produced by the voltage-to-current module (V-I, purple). The dotted black line corresponds to the laser in CW operation at the same pump level for mode-locked (ML) output. The responses of the mode-locked laser to pump modulation via the V-I is in dark red and the control beam using 3 W and four passes is in light red. In dashed-dotted is the response when both the V-I and control beam are used simultaneously.

Neuchâtel[8], the same one used in [49]. The converter is able to supply the pump diode with ± 1 A via a conversion of -100 mA V^{-1} in parallel to the main high current DC source. This type of feedback was used as a benchmark to the depletion modulation method.

All amplitude responses are summarised in Figure 6.14. The voltage-to-current (dashed light-blue) has an extremely broad response of >1 MHz. An assured way of meeting the bandwidth requirements for locking. The AOM trace, taken by measuring the signal of the control beam after the AOM shows a surprisingly low bandwidth of just 80 kHz, as the expected bandwidth based on the manufacturer ratings ought to be >1 MHz[9]. However, this is sufficient for locking as shall be demonstrated below. The continuous-wave (CW) measurement was done with the V-I module while pumping the disk with ~100 W, the required amount for the mode-locked (ML) operation. The system clearly shows the relaxation oscillations frequency with a spike around 43 kHz

[8]Thank you so much Norbert Modsching, Stephane Schilt and Marc Durrenberger!

[9]The AOM response seemed to fluctuate between 80 and 100 kHz, depending on work point. Additionally, the measurement was done at a much later time than the other response plots and locking experiments, and the alignment was different than the original experiments. The source of discrepancy has to either come from the driver electronics, alignment issues or used photodiode (which had to fit in the extremely small space available for measurement).

accompanied by a 90° phase lag, as this is the resonant frequency[10]. For the mode-locked frequency responses, both the V-I and the control beam display the same behaviour. In absolute terms, an offset of 180° should exist between the two, as each acts in opposite directions for increasing signals. However the measurements have the relative phases set to zero at 20 Hz as the phase at the lock-in input is arbitrarily delayed when compared to the signal generator, so they overlap in the Bode plot. Both display a highly attenuated double-pole response, showing how the mode-locked oscillator acting as a low-pass can kill oscillations and be self-stabilizing. Both schemes reach 90° lags at 10 kHz, which is surprising as the first intuition of many laser scientists is to think that acting on the depletion channel would allow for higher bandwidths. This is even exacerbated by the existence of two other works on f_{CEO} locking via depletion which both show a considerable extension of the bandwidth when compared to gain control via pumping [138,139]. Which leads to the use of both the V-I and control beam in tandem as a test to the directionality of the action, i.e. if pumping and depleting had different dynamics when increasing or decreasing gain. As seen by the three overlapping curves, it appears that both methods act exactly in the same way on the system. A theoretical discussion on the performance and comparison to the other depletion based works will be given further below.

f_{CEO} and φ_{CEO} locking

Locking, as expected from the frequency responses, was the same for all three methods. Displayed in Figure 6.15 are the locked state RF measurements, a) and b), show the coherent needle, together with all the side peaks and bands still stemming from the residual noise. Most satellite frequencies are attenuated by 30 dB below the carrier, however it can be seen that several peaks can still reach supra-−20 dBc values. The frequency distribution of the locked state is quite broad, reaching the noise floor only around ±150 kHz, the crossing point between the flicker- dominated noise to mainly white-noise. The steps in the measurements shown in b) stem from the long >3 minute sweeping time and the noise state of the oscillator during the measurement. The true noise floor of the V-I measurement was 5 dB higher than that of the control beam due

[10]There is no measurement for the control beam in CW as the beamline is optimized for the pulsed case, due to different beam size, divergence, M^2 etc.

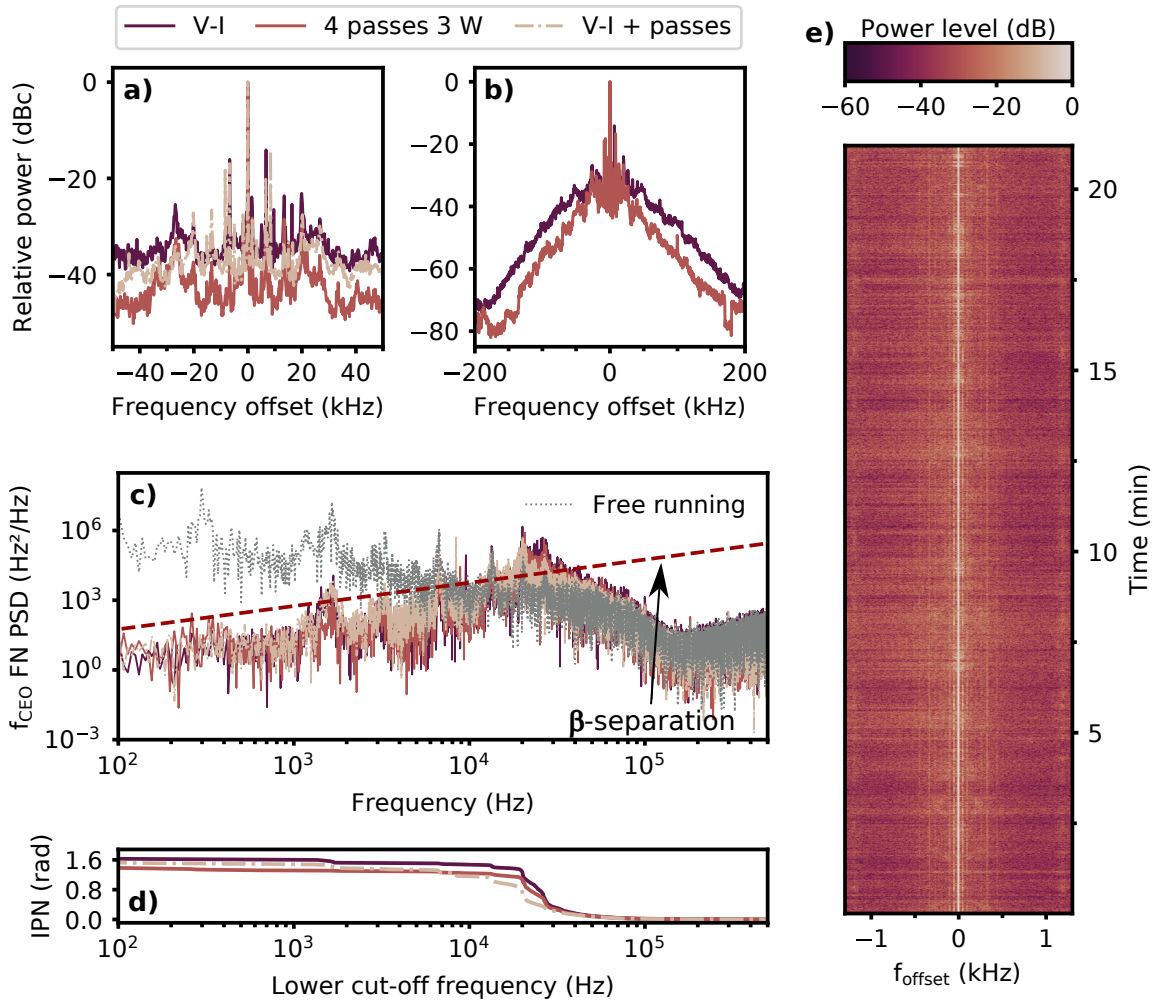

Figure 6.15: f_{CEO} locked stated measurements and performance. The color scheme applies to all plots, dark red for locking using the V-I converter, red for 3 W of the control beam passing four times on the gain medium and lastly the dash-dotted beige line corresponds to using both methods in tandem. In a) and b) are RF measurements with 1 Hz bandwidth resolution, for different spans. Displayed in c) are all frequency noise power spectral densities, along with the free running case (dotted grey) and the β-separation line. The corresponding integrated phase noises (IPN) are shown in d), integrated from 500 kHz down to 100 Hz. A time series spectrogram of a lock using the 3 W control beam and four passes is shown in e). The resolution bandwidth for this last plot was 3 Hz. More details in the text

to a higher amplification setting of the APD during that measurement. The left-right asymmetry of the distribution comes from setting the f_{CEO} at the lower frequency edge of the the band-pass filter, and measuring the RF signal after amplification.

In the frequency noise power spectral density (FN PSD) (Figure 6.15 c)) it is possible to see the effects of the servo loop on the system: most of the <10 kHz in-phase components were pulled under the β-separation line, and the frequencies above 10 kHz, to which the system can still respond, albeit out-of-phase, are pushed to higher noise

values than the free-running case. The so called "servo-bump" peaks between 20 to 30 kHz and as those frequency components are pushed above the β-separation line, they contribute substantially to the noise of the system, specially seen in the integrated phase noise (IPN, Figure 6.15 d))[11]. Despite the issues with the high frequencies, it was possible to have locks lasting longer than 40 min without any slow feedback loop. A consequence of the large amplitude on which four passes with 3 W can work. An example of a long term lock is shown in Figure 6.15 e) where a time series spectrogram of more than 20 min is shown (limited by the number of spectral samples). In this plot, an explanation for the occurring small discrepancies – not equal IPNs or RF spectra – between all shown curves can be deduced. The background noise is constantly shifting and evolving, consequently it is not possible to catch the system in the same state for each of the locks. The minimum time between IPN measurements was 45 min (the time it took to save a trace) and for every new lock the PI settings had to be readjusted. Nonetheless, the IPNs lied consistently around 1.5 rad, ~820 as of jitter, for any of the tried methods.

Along with a stable f_{CEO} the system also displayed, qualitatively, better amplitude noise performance [49, 51, 52]. The WLG was considerably more stable, displaying no flickering, as it is extremely sensitive to amplitude fluctuations. It is a testament to the observed correlation between f_{CEO} and laser amplitude noise seen in Section 6.2.1.

Discussion: performance and outlook

The performance of the locking was mostly hindered by the high amount of noise that the system displays already in the free runnnig case and it was not possible to achieve a sub-radian IPN. This does not mean however that sub-radian integrated phase noise values cannot be achieved by the depletion control. Although not experimentally verified, there is no argumentation, as far as the author knows, that the performance of such a method would be hindered in other systems when compared to pump control, or that it would be a poor performer in systems displaying much lower free-running noise. On the contrary, demonstrating in this system that there is an equivalence to pump modulation entails that this method will perform equally well, regardless of the

[11] The author feels compelled to point out that stating "at frequency X the IPN integrated Y rad" – as often seen in the literature – is erroneous and has no real meaning, as the direction of integration matters! The function is nonlinear, being the square root of an integral, and an example of low-to-high Vs. high-to-low integral can be found in the Appendix (Figure H.3) along with more information.

conditions. It has to be noted that the exact same V-I module was used in [49] and due to the considerably lower free running noise and better servo electronics, the measured IPN was 200 mrad, not far behind several published Ti:Sapphire systems [184, 185]. It is fair to assume that application of the depletion scheme on that TDL would lead to equally low values of the IPN.

The proven equivalence of both methods when applied to Yb:YAG TDLs is also not clear at a first glance. Gain modulation via pump control was shown to be hindered by the effects that the upper-state lifetime has on the gain dynamics of laser oscillators [48, 181]. It is then argued that the "energy storing" effect mitigates the control bandwidth, as lowering the gain (by diminishing the pumping) is a slave to the gain-loss negative exponential, with a time constant proportional to the upper-state lifetime. Effectively bypassing this limitation is an active field of research, as larger bandwidths result in better performance of these laser tools. On first inspection, it is assumed that gain modulation through depletion can effectively bypass the upper-state lifetime bottleneck. The response of the gain is supposed to respond instantly with an amplitude proportional to the control pump power. Notwithstanding, in this whole argumentation it is neglected that the whole system is ruled by gain-loss mechanisms which are all coupled together within an oscillator. The theoretical background for the oscillator dynamics of three distinct control mechanisms (pump, depletion and losses) which can influence the f_{CEO} will be explored below.

For further discussion, the presented system is considered together with two other systems from the literature following the approach of depletion as a gain control mechanism for locking of the f_{CEO} [138,139]. In both these other works the bandwidth of the amplitude frequency response is widened considerably. In the case of the utilization of cross-gain modulation in a three-level Yb system [139] – closest to the presented TDL – the 90° lag point was extended from 30 kHz to 0.5 MHz. However, the used system was a fibre laser, which lies in the opposite extreme of energy saturation when compared to thin-disk lasers, which affects some of the oscillator time constants. Meanwile, the findings from the work by Karlen et al. [138] using Er:Yb:Glass, might be not suitable for a one to one comparison with the author's system. The gain medium from the publication has a very different energy structure influencing drastically the laser dynamics [186–188].

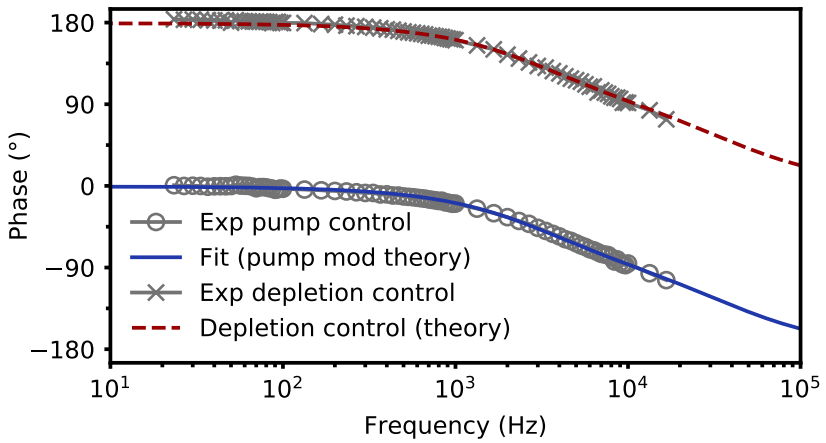

Figure 6.16: Comparison between experimental and theoretical transfer functions. The open circles are measurements of the system response to pump modulation and the blue solid curve a theoretical model [181] where the parameters related to nonlinear modelocking losses were retrieved from a fit to the data. Using the retrieved and known coefficients, the red dashed curve was obtained from the model introduced in the Appendix G which models the gain via a depletion control mechanism. Then the experimental data for the control beam transfer function was added as crosses.

Despite the differences, it is essential to understand why those systems display an enlarged control bandwidth, while the presented TDL system does not, as this knowledge might push the noise performance of TDL based combs to record levels. To answer this conundrum, the approach to the transfer functions of the laser amplitude in function of pump modulation presented by Matos and colleagues [181] was improved to also include depletion modulation and losses modulation. In this case the derived equations can be found in the Appendix G.

As seen by Figure 6.16, the agreement between the theoretical model to describe a depletion control method (dashed red) and the experimental data (crosses, that can also be seen in Figure 6.14) is excellent. To obtain the red dashed curve of Figure 6.16 according to Equations G.3 and G.4, all coefficients were either known or retrieved from fitting the model from [181] to the pump modulation data (circles: data; solid blue: fit of model). Ultimately, it appears that pump modulation and depletion control lead to the same bandwidths as they act, in practical terms, to the exact same laser level, specially if one pumps in the zero-phonon line.

Testing now the model against the data from References [138, 139] using the same approach, an enhanced bandwidth to a depletion control was also not obtained as seen in Figure 6.17. In the case of the Yb:Er:glass, this is understandable as the sys-

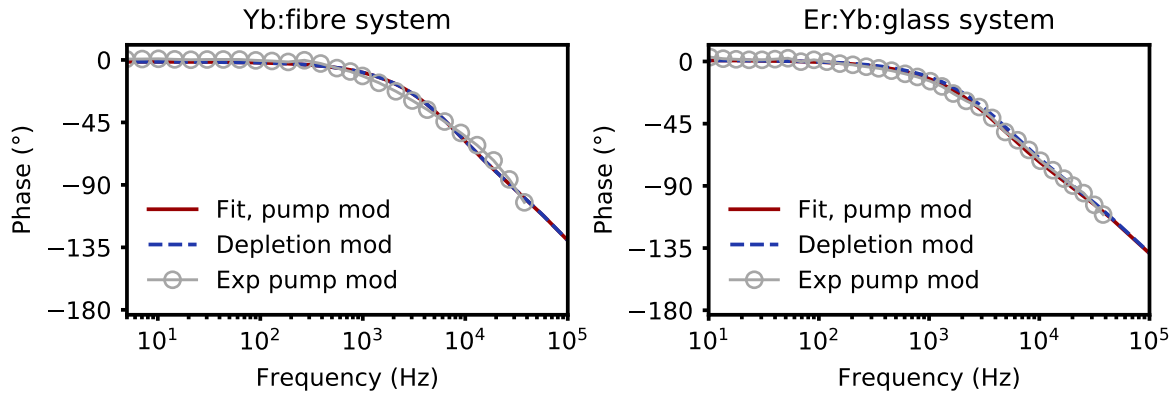

Figure 6.17: Comparison between experimental and theoretical transfer functions of other systems. The open circles are measurements of the system's response to pump modulation and the red solid curve a theoretical model [181] where the parameters related to nonlinear modelocking losses were retrieved from a fit to the data. Using the retrieved and known coefficients, the blue dashed curve was obtained from the model introduced in the Appendix G which models the gain via a depletion control mechanism. The depletion control is shifted by 180° for better visualization of the overlap. The Yb:fibre system is from [139] and the Er:Yb:glass from [138].

tem should probably display one more pole from the special energy level scheme of this gain medium, and a better model would need to be had. Regarding the fibre system, the data not fitting the model shows that the model is not suitable to describe the system, however it is not clear why. The author believes that there is one more hidden mechanism (unbeknownst to the authors) behind the results shown by Gürel and coworkers, which would lead to the necessity of adding a third equation to the partial differential equation system[12], allowing to then fully model the system presented in [139]. Additionally, loss modulation was also tested by the model. In Figure 6.18 an arbitrary system, loosely based on the thin-disk laser system of [52] was modelled and the phase-lead is correctly predicted by the theoretical equations, which results from the zero created in the transfer function.

A full in-depth discussion on the possible extension of the bandwidth using this gain modulation control from the analysis of the model can be found in [53]. In summary, and in the lights of the data here collected and model predictions, no enhancement – beyond 1% – should be expected for Yb:YAG TDLs. This does not diminish the practicality or importance of this method. Being an alternative to pump modu-

[12]I cannot disclose more at this point, investigations by other groups also found no evidence of enhanced bandwidth via depletion control on another fibre system.

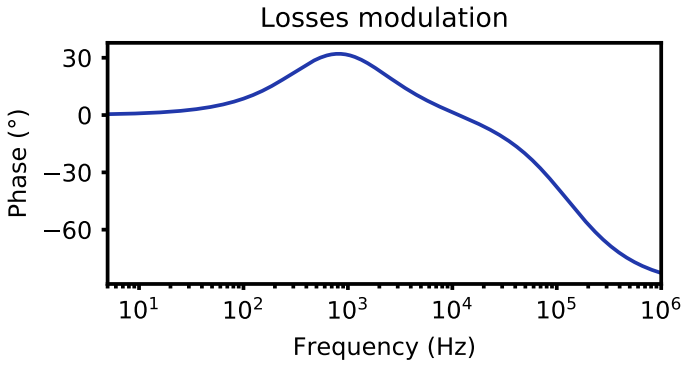

Figure 6.18: Transfer function of a system (loosely based on [52]) using losses as modulation. Losses allow to extend the bandwidth by first having a phase-lead component before entering the phase-lag region. This results from the zero of the transfer function.

lation that uses only "off-the-shelf" optics makes this method incredibly versatile and allows it to be applied as a "poor-mans-job" in its simplest configuration, all the way to a state-of-the-art system if enough effort is put into place.

This is enabled by the capability of parallelization of control beams, number of passes, power etc. Those are all up for the imagination and will of the engineer that sets up a depletion based f_{CEO} locking. As far as optical design considerations go, the most important would be to avoid a back coupling into the oscillator. Back reflections as strong as the modulation beam interfere with the operation of the mode-locked laser (allows the build up of a CW field). In the case of the presented system this was achieved via an isolator, but a quarter-waveplate before the back-reflecting mirror would have been sufficient to then dump the back-travelling light after the TFP selecting the control beam.

As a last remark, the scheme seems fully scalable, specially due to its versatility in design and easiness to scale all necessary optics, the main hurdle being geometric space to accommodate all the necessary beamlines.

7 | Conclusion and outlook

In this thesis, the design and implementation aspects of compact, carrier-envelope phase stabilized, 100-W-level sub-300-fs oscillators, were given. Some of the important technical difficulties when designing and building such systems were shown and discussed, touching briefly on possible solutions for future developments. Although the thesis hinges on hard-aperture Kerr-lens mode-locking of thin-disk lasers and their subsequent CEP stabilization, several of the engineering aspects discussed in this thesis can also be applied to oscillators using different form factors of the gain medium. Namely, the shown ray-tracing – or ABCD – formalism coupled with a differential evolution algorithm for the aided design of high intracavity peak power resonators and the shown f_{CEO} stabilization. Although the stabilization method is best suited to the geometrical aspects of thin-disk lasers, it should also be possible to apply the scheme to bulk or fibre laser oscillators. Inserted in the scaling of compact high-power sub-100-fs ultrafast sources, the first cleanly Kerr-lens mode-locked Yb:LuO TDL was shown. A brief summary of the main results achieved during the course of this work are given below.

High power ultrafast thin-disk oscillators

Several of the parameters impacting the performance of high-power ultrafast thin-disk laser oscillators were studied and shown, along with design and construction pointers for an effective implementation of such systems. Two systems were experimentally demonstrated: an Yb:YAG based TDL generating up to 2 µJ pulses at a repetition rate of 33 MHz (66 W average power) and 250 fs pulses and an Yb:LuO system allowing the generation of 160 fs pulses with an energy of 0.1 µJ at a repetition rate of 60 MHz (6 W average power). Moreover the behaviour of the high power system was investigated through the ABCD formalism. A differential evolution algorithm had to be in-

corporated into the solution seeking software as the typically used recursive algorithm showed limitations when dealing with the high intracavity peak powers encountered in these state-of-the-art laser systems. The inclusion of the differential evolution allowed to simulate systems with peak powers >30 times those of the Kerr medium's critical power for catastrophic self-focusing. The simulated resonators showed behaviours similar to the implemented Yb:YAG system. The excellent qualitative agreement between the solitonic condition and the experimentally measured output parameters coupled to the simulated resonators show that this tool has a tremendous potential in the design of the next-generation of resonators boasting intracavity peak powers several tens – or even hundreds – of times the critical power of the materials used within these resonators.

To achieve shorter pulses, two approaches were attempted and shown. The already mentioned Yb:LuO and nonlinear post-compression. The former, achieved state-of-the-art performance and was a milestone, by showing that KLM scaling of thin-disk lasers based on materials with a broader gain bandwidth was – and is – an approach with great potential to reach compact few-cycle 100-W-class systems. To further overcome gain bandwidth limitations, the pulses from the high power Yb:YAG were spectrally broadened and temporally compressed in an external setup. The nonlinear post-compression was demonstrated to be a robust and cost-effective method to achieve sub-50-fs with high peak power at multi-MHz. It was possible to obtain 37 fs pulses at an average power of 4 W.

Stabilization of φ_{CEO} of thin-disk lasers

For the CEP stabilization of the high power system, three main points were covered: detection of the f_{CEO} for pulses >150 fs; noise characteristics; and stabilization of the φ_{CEO}. As for the self-referenced f_{CEO} detection an octave is needed, hence, a detailed procedure on how to obtain SCG in bulk was given, leading to the world's first shown f_{CEO} detection based on bulk filamentation from TDLs. The noise characteristics of the free-running f_{CEO} were discussed for long and short time scales and a strong source of noise was found to arise from temperature variations of the water cooling the thin disk. The following stabilization of the φ_{CEO} was achieved through three different methods: a novel scheme involving gain modulation via a small part of the laser's own output,

pump modulation and both methods concurrently. The stabilization yielded 820 as of φ_{CEO} jitter. It was also shown that enough modulation amplitude can be had via multiple passes on the disk which enabled locks longer than 40 min without the need of a slow feedback. The newly developed method strips down the requirements for φ_{CEO} locking of TDL lasers to a bare minimum: the detection of the f_{CEO}, the PLL electronics, and any laser amplitude modulation method (in the case of this work, an AOM). This broke the trend of previously shown CEP stabilized thin-disk lasers of using specialized equipment to that end, opening the doors of either stabilized waveforms or optical frequency combs to a more broader scientific community. Moreover, the performance of the shown method was compared to proven methods for the locking of the f_{CEO}, showing that it performs equally well as pump modulation. A discussion on its limitations and comparison to other works was also provided, by the application of a laser modulation theoretical model developed during the course of this work.

7.1 Outlook

The tools that will be used to help on the design of the future high power systems will be invaluable. The ABCD analysis and the approach taken to tackle the high-peak power resonator design shown in this thesis is a great candidate to be such a tool, specially if the necessity to have more complicated resonator designs emerge. And if paired with the mode-locking master equation, it is hoped that the system performance can be evaluated and optimized before deployment of the optical system.

The high-power system showed in this work lacked the necessary thermal management to achieve the state of the art 0.4 GW intracavity peak power, but the groundwork necessary for such an achievement is already laid down. Further scaling through the principles shown in [29] should still be possible.

When it comes to the scaling of the output power of materials with gain bandwidths capable of delivering sub-100-fs pulses, fantastic works have been already presented, with the demonstration of 21 W of average power from a Yb:LuO TDL, boasting pulses with a duration of 95 fs [38]. However, further scaling laser systems which can deliver sub-50-fs will always prove challenging as the observed efficiency from these systems decreases drastically [102] and perhaps a paradigm shift – such as similaritons [189]

or quartic solitons [190] – will be needed to achieve the optical-to-optical efficiency observed by TDLs operating at longer pulse durations, where again, it is hoped that the information provided in this thesis will be of a helpful nature.

However, the most important aspect of these laser sources is their versatility as engineering and research tools. Throughout the course of the work shown in this thesis the author provided support to several other experiments built around the powerful Yb:YAG laser system, which are summarized below:

- The world's first fastly and widely tunable non-collinear optical parametric oscillator (NOPO) operating in the visible [91] (pumped by the third-harmonic of the TDL (340 nm), designed and built by the author with the help of Fabian Placzek, maximum output of 6 W with an efficiency of 21%);

- Fastly tunable double output NOPO in the IR and VIS, via intracavity sum-frequency generation [191];

- Doubly resonant OPO at 2 µm for the investigation of the resonator dynamics [93], for which f_{CEO} stable experiments are planned;

- Generation and characterization of THz radiation [192], inserted in the combined use of the 2 µm OPO together with the TDL for the investigation of light-matter interaction and generation of high-power broadband THz radiation;

- Pumping of an NIR NOPO used in combination with the TDL output for the stimulated Raman spectroscopy detection of microplastics in fluids at video-rates [193];

- Investigation of the optical properties of plasmonic structures (more details below).

The list above shows the tremendous potential of such tools. One single laser system is able to deliver enough power for research in a multitude of scientific areas, from fundamental physics/optics to applications in ecology. This is enabled by its small footprint and reliability.

As a last future research direction, below, some preliminary results on the investigation of the plasmonic properties of nano-antennas are shown.

7.1.1 Bullseye nanostructure

The investigation of the properties of metal and semiconductor nanostructures is a topic which is attracting considerable attention as it will inevitably shape the technologies of the future. As some examples, their characteristics enable: the miniaturization of optical devices [194], their possible integration with electronics [195], applications in quantum computing [196], biological sensors [197] and many others. Thus, their study is of great importance. They can be computationally studied as most of the underlying physical mechanisms are known, however, it is still numerically intensive and the results are challenging to analyse and require experimental benchmarking. Moreover, several factors which are not accounted for in simulation trials and can only be known *a posteriori* end up drastically changing the outcome of experimental results, i.e. the author and Liping Shi investigated the impact of impurities [198], the reshaping of the structures due to the strong electric fields [199] and the disputed origin of third-harmonic generation in gold diabolo nanostructures [200], to name a few.

The in-depth physical description of plasmonics falls out of the scope of this thesis, and can be found elsewhere [201]. Nevertheless, in general, the interaction of the impinging light with materials where the excitation of surface plasmon polaritons (SPP) is facilitated can be further enhanced by structures. This structures can allow the concentration of electromagnetic fields in volumes several times smaller than those of the incident wavelength. In dimer-like antennas, for example, Liping Shi and the author observed that the enhancement of the field can increase the intensities in the hotspots by 600 fold of those impinging the structures [199, 202].

The studied structures in this work, bullseye shaped antennas, allow for such concentration of electromagnetic fields as well as storage of the energy in plasmonic modes [203, 204]. The antennas were milled via a focused Ga^+ ion beam on a crystalline gold film and were provided by the University of Oldenburg. A sketch of the used experimental setup can be seen in Figure 7.1 where a scanning electron microscope picture of one of the structures can be found. The laser source developed in this work has excellent properties to study these structures. Typically, nanoantennas are probed via low power sources and it is not possible to achieve high intensities in large areas, limiting the size of the studied structures. One could use lower repetition rate systems

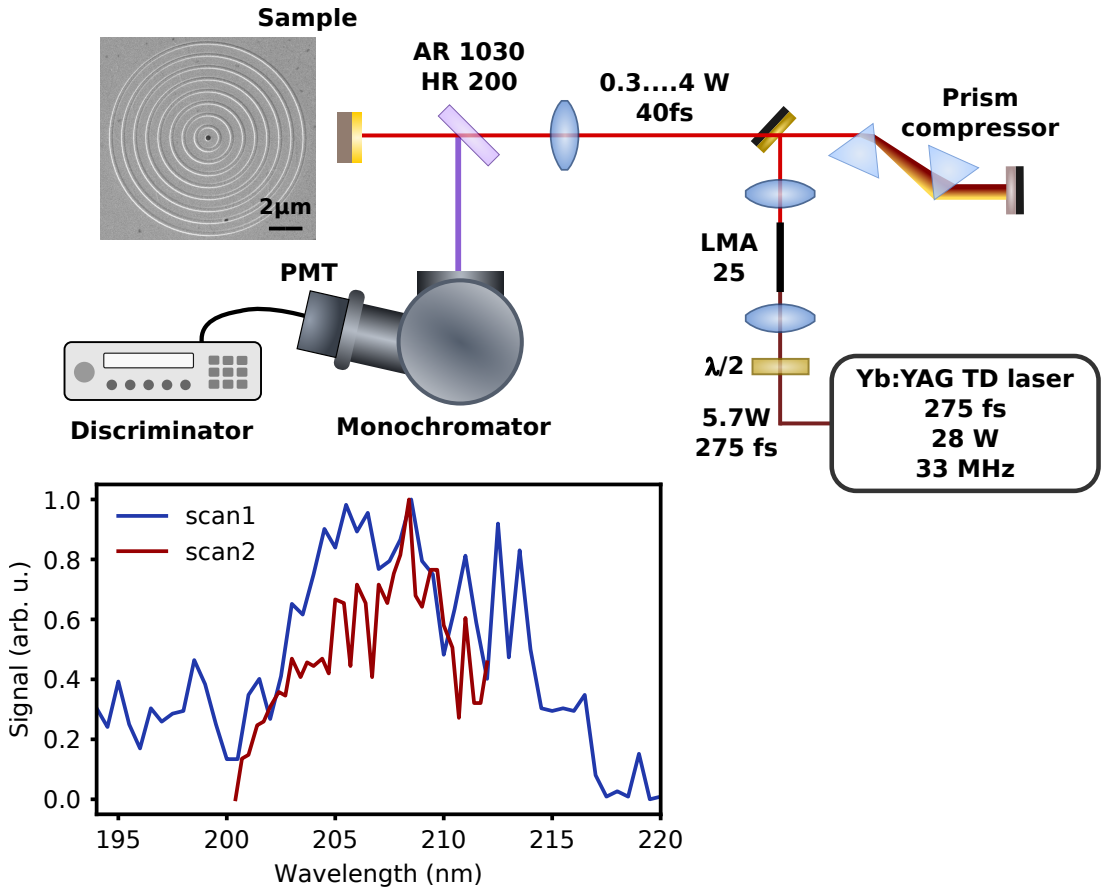

Figure 7.1: Plasmonic experiment setup. The compressed pulses from the system (37 fs) were used due to their high peak power (up to 2.4 MW) and lower fluence to study bullseye shaped nanostructures. The 5th harmonic of the system was scanned. The data has had minimal processing done to it.

delivering higher energies, but the increased events-per-second rate when driven by a multi-MHz source is a very desired feature for faster acquisition times.

These structures' ability to enhance the harmonic generation at an interface is of great interest in the pursuit of more efficient nonlinear interaction and so the 5th harmonic of the source, close to the vacuum UV limit, was investigated. The compressed pulses of the oscillator were used to illuminate the antennas with peak intensities between $1.8 \times 10^{10}\,\mathrm{W\,cm^{-2}}$ and $2.4 \times 10^{11}\,\mathrm{W\,cm^{-2}}$. Some preliminary scans can be found in the Figure. Two scans at what appeared to be the highest intensity with no degradation ($I_0 = 9 \times 10^{10}\,\mathrm{W\,cm^{-2}}$) were done. However it was apparent by the second, higher-resolution scan that indeed there was still a long term degradation of the antennas and the intensity needed to be further reduced.

Already these results show the capabilities of such structures. These were already quite exciting scans and more data collecting is needed to completely investigate the properties of these antennas under intense radiation.

A | ABCD matrices

As it was introduced in the main body, the ray-tracing formalism was used to simulate the resonator condition. Here are the used matrices, for linear propagation of a Gaussian beam. These are the general case matrices. In all of them, n is the refractive index, θ the angle of incidence, d the distance propagated within the material, R the radius of curvature. The plate totals are used for the insertion of a plate, without the need of calculating the waist inside the material. If the waist is needed, in the tangential plane, first the appropriate interface matrix is needed and then the general case propagation is considered.

Both axis (or normal incidence)	**Sagittal**	**Tangential**
	Medium propagation	
General case $\begin{pmatrix} 1 & d/n \\ 0 & 1 \end{pmatrix}$	Plate total $\begin{pmatrix} 1 & \frac{d}{\sqrt{n^2-\sin^2(\theta)}} \\ 0 & 1 \end{pmatrix}$	Plate total $\begin{pmatrix} 1 & \frac{dn^2\cos^2(\theta)}{\left[n^2-\sin^2(\theta)\right]^{3/2}} \\ 0 & 1 \end{pmatrix}$
		Air→material $\begin{pmatrix} 1 & 0 \\ 0 & \frac{n^2\cos^2(\theta)}{n^2-\sin^2(\theta)} \end{pmatrix}$
		Material→air $\begin{pmatrix} 1 & 0 \\ 0 & \frac{n^2-\sin^2(\theta)}{n^2\cos^2(\theta)} \end{pmatrix}$
	Curved mirrors	
$\begin{pmatrix} 1 & 0 \\ -\frac{2}{R} & 1 \end{pmatrix}$	$\begin{pmatrix} 1 & 0 \\ -\frac{2\cos(\theta)}{R} & 1 \end{pmatrix}$	$\begin{pmatrix} 1 & 0 \\ -\frac{2}{R\cos(\theta)} & 1 \end{pmatrix}$

One needs to see that when incident on a material with an angle θ, that the effective length of the material d_{eff} changes to:

$$d_{\text{eff}} = \frac{dn}{\sqrt{n^2 - \sin^2(\theta)}},$$

and hence the matrices. All the above matrices, their derivations and useful information can be found in [73, 103, 205], with the exception of the interface matrices which were derived by the author to obey the correct propagation through the materials in accordance with [73, 205].

A.0.1 Kerr-lens matrix

The Kerr-lens matrix is derived from the parabolic gradient index (GRIN) matrix, where the gradient is dependent on the intensity and n_2 of the material. The derivations can be found elsewhere [58, 112, 115]. The use of the GRIN matrix is justified in the sense that it is self consistent with the Gaussian beam formalism, allowing it to be used just like the other matrices.

For the Kerr matrix the following identities are needed:

$$\begin{aligned} I_0 &= \frac{2P_0}{\pi w_s w_t}, \\ n &= n_0 + n_2 I_0, \\ \gamma &= \frac{1}{\sqrt{w_s w_t}} \sqrt{\frac{4 n_2 I_0}{n}}. \end{aligned}$$

Where I_0 stands for the peak intensity, P_0 peak power, $w_{s,t}$ the beam radius in the sagittal and tangential planes, respectively. Like above, n_0 is the refractive index and n_2 the nonlinear refractive index of the material.

The Kerr matrix is then defined as:

$$[M_{\text{Kerr}}] = \begin{pmatrix} \cos(\gamma d) & \frac{\sin(\gamma d)}{n\gamma} \\ -n\gamma \sin(\gamma d) & \cos(\gamma d) \end{pmatrix}$$

where again, like above, d is propagated distance. In the case of this work, the plate was split into many thin slices and for each slice the matrix was being calculated and

applied to the beam, as γ is dependent on $w_{s,t}$ and these are ever changing in a Kerr medium. It is of great importance that one does not forget to apply the interface matrices, before and after the medium, in the tangential plane.

B | Differential evolution

Differential evolution (DE) [113] is a heuristic optimization algorithm akin to a genetic algorithm. It consists in holding a population of N elements p_i, each in $\mathbb{R}^n$, n being the dimensionality of the problem, and iteratively optimize the overall quality of the population in regards to a fitness function $f : \mathbb{R}^n \to \mathbb{R}$. Needless to say, one wants to find the minimum $\mathbf{m}$ of the function f such that $f(\mathbf{m}) < f(\mathbf{s})$ for any $\mathbf{s}$ in the search space, i.e. the global minimum (although, naturally, this type of optimization procedure does not guarantee that one will do so). Differential evolution allows for any function f to be minimized, without the need of f to be differentiable, as it makes no mathematical assumptions about the problem at hand. This makes this type of algorithm a great choice to the problem of high peak power oscillators where several discontinuities can be found.

The traditional way of implementing DE in a population involves three phases: mutation generation, cross-over and selection. A sketch of the algorithm can be seen in Figure B.1.

For each j-th population member, a mutant is created which has as "parents" 4 distinct members (j, a, b, c). A cross over probability CO dictates how strong mutations can occur for each of the degrees of freedom of the problem. If no mutation occurs for the i-th dimension, then the mutant inherits the original j-th member's value. If a mutation occurs, then the mutant M_j will have its i-th degree of freedom calculated as $M_{j,i} = a_i + F(b_i - c_i)$. The value of F can be a value between 0 and 2. In the case of this work, CO=0.7 and F was always set as a random value $F \in [0, 2]$ per mutation, instead of a fixed value.

After the generation of the mutant, its fitness is compared to that of the original member. If better, then it replaces the original member in the population.

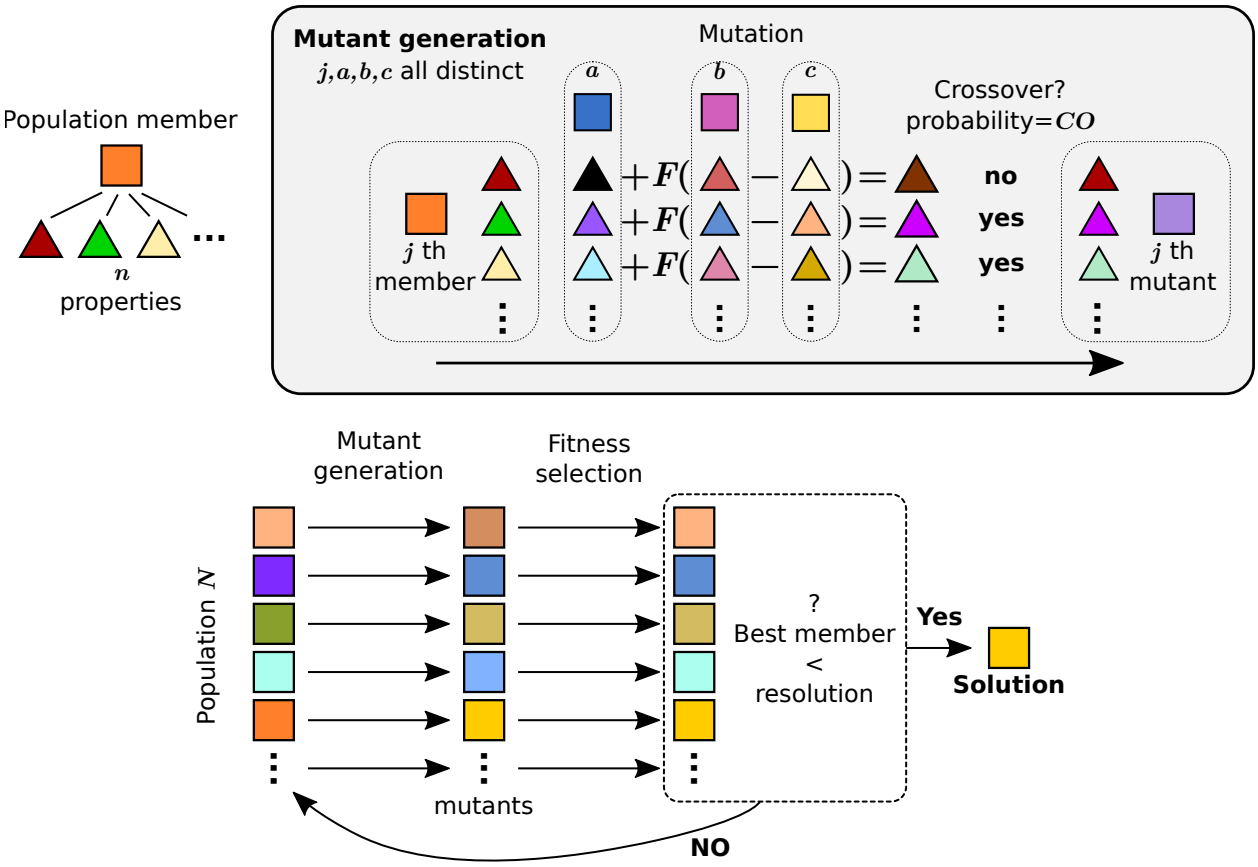

Figure B.1: Schematic of the differential evolution heuristic algorithm.

Lastly, in the case of this work, for most of the simulations, the algorithm was changed to be closer to a genetic algorithm, where all mutants are added to the population, the population ranked and only the better half is kept.

C | Simulation parameters

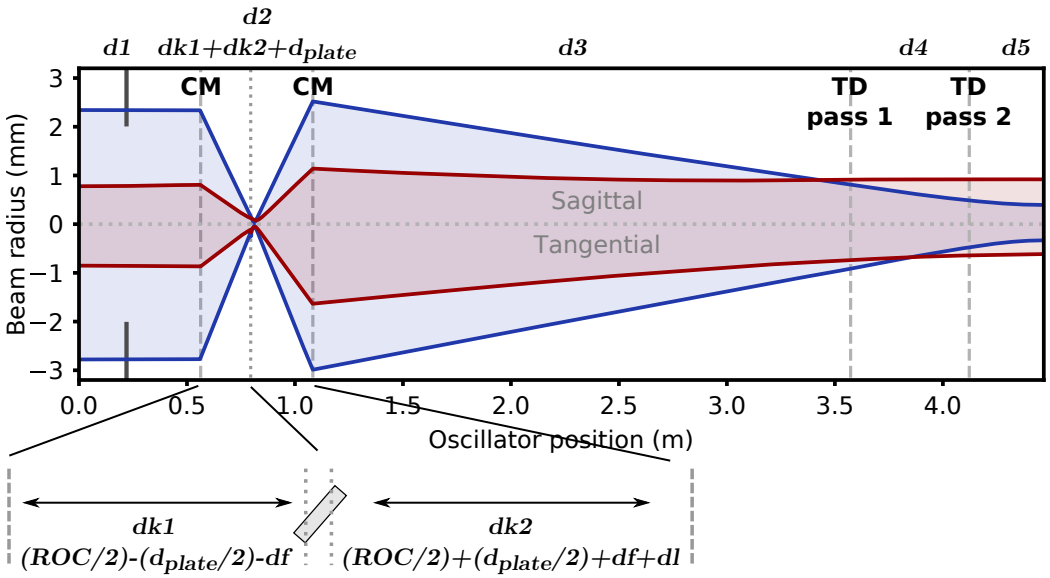

Figure C.1: Schematic of distances for the ABCD simulations.

Table C.1: List of oscillator parameters.

Parameter	Value (mm)
$d1$	540
df	(variable)
d_{plate}	(see Apdx. A)
dl	(variable)
(dl, $\mathbf{T}_{\text{hi}}$ for 3 mm FS)	16.3
(dl, $\mathbf{T}_{\text{lo}}$ for 3 mm FS)	17.2
$d3$	2492
$d4$	549.4
$d5$	345
Mirror ROC	500
Thin disk ROC	18000

Parameter	Value (°)
Plate θ	(Brewster's)
Curved mirror θ	2.94
Thin disk 1st pass θ	5
Thin disk 2nd pass θ	3

D (Self-calibrating) d-scan

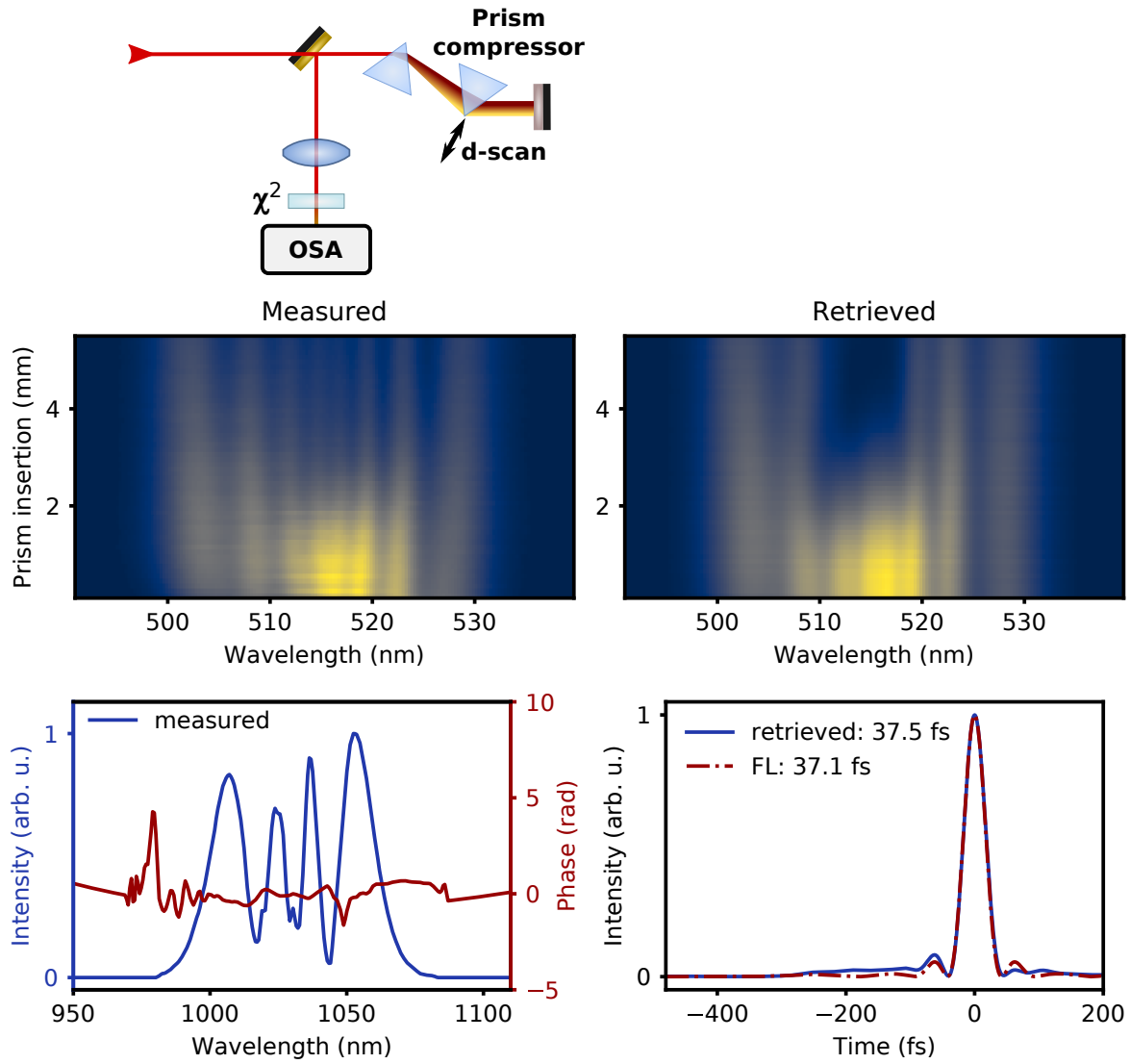

Figure D.1: Self-calibrating d-scan example. One measures the second harmonic response for incremental introduction of GDD and TOD. These will be retrieved by the algorithm.

This method of experimentally extracting the duration of ultrashort pulses has some similarities to FROG [206], namely the variable scanning and iterative retrieval. However, in contrast to FROG, the d-scan optical setup is easier to implement, there is

no ambiguity of the retrieved time axis and it is more versatile (as seen in this work). The basic d-scan concept is to simply have a dispersion resolved spectrogram of a nonlinearity, i.e. introduce different amounts of dispersion to the pulse while recording the nonlinear spectral response. The versatility comes from the fact that in the case of an SHG spectrogram the introduced second and third order dispersions do not need to be known, as they can also be retrieved from the algorithm that processes the scan [171]. This is exactly what was performed in this case, scanning the insertion of the second prism changed the dispersion seen by the pulse, while recording the generated second harmonic. The retrieval was done via a differential evolution algorithm by Ayhan Tajalli [172], with the inputs to the algorithm being the fundamental spectrum and the measured trace, being the spectral phase encoded in the spectrogram. The retrieved scan is then a simulated d-scan using the converged introduced second and third order dispersions; the spectral phase; and the response of the setup to the different optical frequencies. All this information allows, in the end, to reconstruct the pulse at the nonlinear crystal. For more information see [170–172].

E | Frequency/phase noise power spectral density measurement

The measurements of the phase noise power spectral density (PN PSD), and of course by conversion of the data the frequency noise PSD (FN PSD) was measured using the method described in [51].

The method relies on the fact that all the noise is encoded in the real time signal that one wants to analyse. In the case of f_{CEO} detection, the signal is obtained by obeying the Nyquist sampling theorem for the f_{CEO}, but undersampling the repetition rate (while paying attention to possible aliasing of an undersampled f_{rep}). In the case of this work, the signal was also bandpass-filtered, to ensure a higher "purity" of the sinusoidal time series.

For the numerical analysis, one assumes that the signal $s(t)$ can be expressed by a time dependent amplitude A and phase ϕ:

$$s(t) = A(t)\ \cos(\ \phi(t)\ ) = A(t)\ \cos(\ \omega_{\mathrm{s}} t + \varphi_{\mathrm{s}}(t)\ ), \tag{E.1}$$

where the phase is decomposed into the central frequency of the signal ω_{s} and added phase noise φ_{s}.

By analytical continuation of the signal into the complex plane via a Hilbert transform $\mathcal{H}$, one gets the complex signal $\tilde{s}$:

$$\tilde{s}(t) = s(t) + i\mathcal{H}\Big(\ s(t)\ \Big) = A(t)\ \exp(\ i\omega_{\mathrm{s}} t + i\varphi_{\mathrm{s}}(t)\ ). \tag{E.2}$$

Computing the instantaneous frequency in time is straightforward via:

$$f(t) = \frac{1}{2\pi}\frac{d\phi(t)}{dt} = \frac{1}{2\pi}\frac{d}{dt}\Im\left\{\log(\ \tilde{s}(t)\ )\right\}, \tag{E.3}$$

where the identity comes from the fact that:

$$\frac{d}{dt}\log(\tilde{s}) = \frac{\frac{d}{dt}\tilde{s}}{\tilde{s}} = \frac{d}{dt}\log(A) + i\frac{d\phi}{dt}. \tag{E.4}$$

Additionally, the imaginary component can be calculated from:

$$\Im\left\{\frac{\frac{d}{dt}\tilde{s}}{\tilde{s}}\right\} = \frac{\Re\{\tilde{s}\}\,\Im\left\{\frac{d}{dt}\tilde{s}\right\} - \Im\{\tilde{s}\}\,\Re\left\{\frac{d}{dt}\tilde{s}\right\}}{|\tilde{s}|^2}, \tag{E.5}$$

which leads to:

$$\frac{d\phi}{dt} = \frac{s\frac{d}{dt}\mathcal{H}\{s\} - \mathcal{H}\{s\}\,\frac{d}{dt}s}{|\tilde{s}|^2} \tag{E.6}$$

With the above calculation one can arrive to the PN PSD or FN PSD through different means. For example, integrating the $d\phi/dt$ term and calculate the PN PSD, $S_\phi(f)$, from:

$$S_\phi(f) = \frac{2}{T}\left|\mathcal{F}\{\phi(t)\}\right|^2, \tag{E.7}$$

where $\mathcal{F}$ represents a (truncated) Fourier transform and T the sampled time. This is the formal mathematical definition for a single-sided PSD, however care needs to be taken when using discrete Fourier transforms. Alternatively, one can use Equation (E.3) to arrive at the FN PSD $S_f(f)$ and use the following identity:

$$S_f(f) = f^2 S_\phi(f) \tag{E.8}$$

to compute S_ϕ.

As a last step, to calculate the integrated phase noise (IPN) from S_ϕ, the following integral is computed:

$$\mathrm{IPN}(f_{\mathrm{lo}}) = \sqrt{\int_{f_{\mathrm{lo}}}^{f_{\mathrm{hi}}} S_\phi(f)df} \tag{E.9}$$

As last remarks on these calculations, the sampled signal should have a base-two number of points to aid with the speed of the FFT and fast Hilbert transformation algorithms. The derivatives are also done using the properties of Fourier transforms: $du/dt = \mathcal{F}^{-1}\{i\omega\mathcal{F}\{u\}\}$. To minimize numerical differentiation noise, the data is appropriately digital-bandpass-filtered, the filter window larger than the detection noise floor. One should also pay attention to the correct propagation of amplitudes through the FFTs, knowing the type of FFT being performed and having the amplitudes of re-

sulting transforms normalized accordingly as mentioned above. As an example, in the case of the FFT library used in this work:

$$S_\phi(f) = \frac{2}{N\mathrm{S_{ps}}} \left|\mathrm{FFT}\left\{\phi(t)\right\}\right|^2 \tag{E.10}$$

where N is the number of samples and $\mathrm{S_{ps}}$ the sampling frequency (samples per second), effectively making T the dividend, instead of divisor.

F | Digitally assisted phase-locked loop

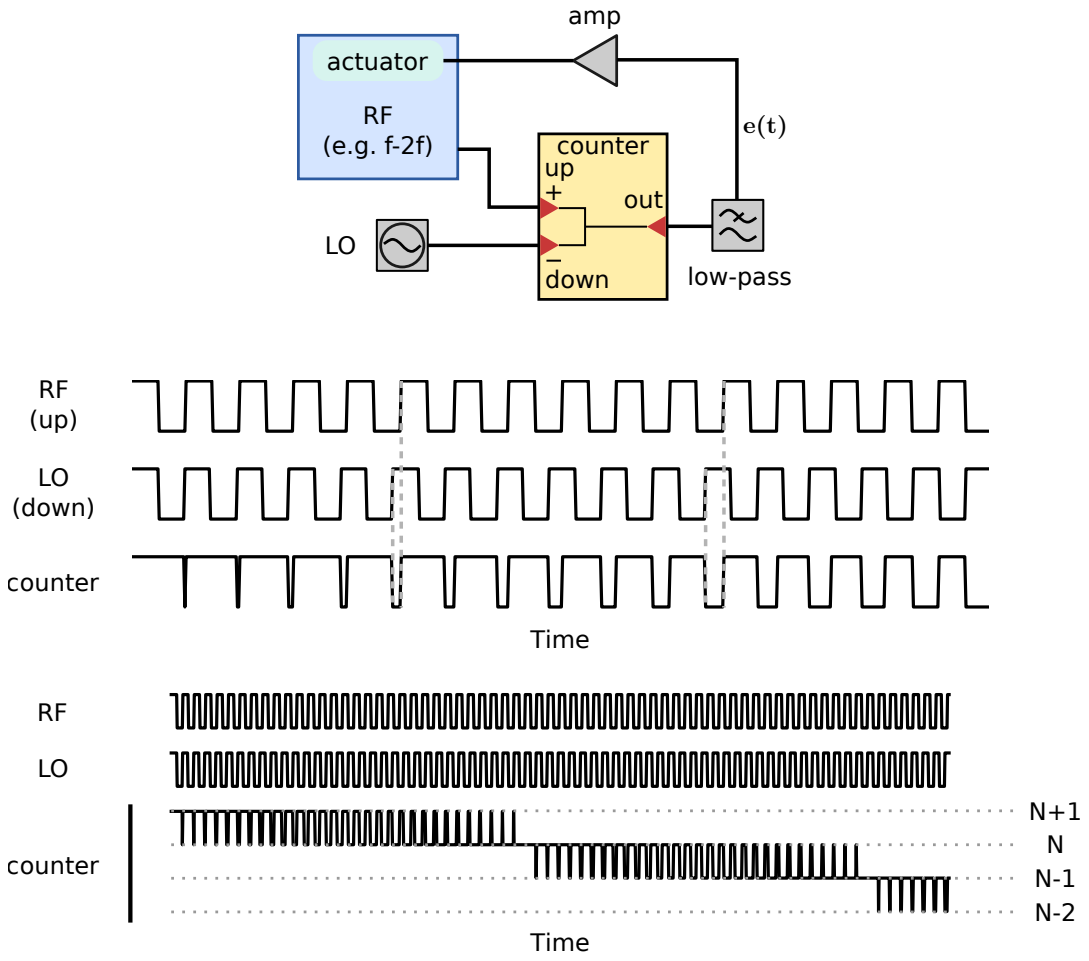

Figure F.1: In this figure a rough schematic of a digitally assisted PLL is shown along with timing charts. In this case there is a counter allowing the PLL to increase the number of countable π-phase jumps before resetting of the signal. The counter works on positive flanks of square signals. RF is a radio frequency signal being compared to the local oscillator (LO, or f_{ref}). In the case above, RF has a frequency slightly lower than that of LO.

In Figure F.1 a rough schematic of a typical digital phase-lock loop in laser science is shown. In this case, instead of analog detection, a digital detection allows one to be insensitive to amplitude fluctuations and phase accuracy is also enhanced. As seen

in Section 6.2.2 the frequencies for feedback are 4 orders of magnitude lower than the detection ones. The basic principle of a digitally assisted phase detection (DPD) is to have a flank sensitive electronic component that will go high for one signal and low for the other. This is usually achieved via flip-flops and three possible states. The phase difference is then encoded in the duty-cycle of the resulting square wave. As seen in the given example, as the local oscillator (LO) has a higher frequency, over time, more "count down" impulses will be seen that the "count up" ones. This leads to the counter to slowly count down. Every time it reaches the next state there is a π phase shift. After low-passing the signal, the square waves are smoothed out and the voltage error signal, named $e(t)$, will be a negatively sloped signal.

It is now easy to see that as $e(t)$ is applied to the system, that the 0 value will only be reached when both signals have the same frequency and are in phase. In the case of this work, the counter had 64 levels, where the 32nd was chosen as zero. This meant that the output of the DPD could count $\pm 32\pi$ phase jumps until hitting the overflow. At the overflow point, the counter just resets the value to the opposite number, i.e. loops around. This means that in the case of this work, the $e(t)$ is a modulo 64π function.

More information on PLL: [207].

G | Transfer function model for modulations

In the work of Matos and coworkers [181], the rate equations describing a solid-state mode-locked laser were used to derive the response of the laser system to a modulation of the pump power. The equations are valid within certain constraints, which can be seen in the reference [181]. The time coordinate is denoted as a capital T to remind the reader that solid-state systems saturate mainly due to average power rather than per pulse, and the dynamics evolve in time scales of several cavity roundtrips, rather than instantly.

We start with Equations (14) and (15) of the article, modifying the latter by adding a term ξ representing the added energy of the control beam shining on the gain medium: a field which interacts with the gain, modifying the steady-state and allowing to modulate the gain term g.

$$T_R \frac{dE}{dT} = (g - l - q(E))\, E \tag{G.1a}$$

$$T_R \frac{dg}{dT} = -\frac{g - g_0}{\tau_L / T_R} - g\frac{E + \xi}{E_{\text{sat}}} \tag{G.1b}$$

Here we have T_R as the caivty roundtrip time, E and g represent the energy of the intracavity pulse and gain of the laser medium, respectively. The losses are broken into two components: l is the linear losses and q (function of E), nonlinear losses arising from the modelocking mechanism. The two remaining terms, g_0 and τ_L are the small-

signal gain and the upper-state lifetime. After linearization of the above equations around the steady state of the system one gets:

$$T_R \frac{d\hat{E}}{dT} = E_\mathrm{s}\hat{g} - E_\mathrm{s}\hat{l} - \partial_q E_\mathrm{s}\hat{E} \tag{G.2a}$$

$$T_R \frac{d\hat{g}}{dT} = -\frac{rT_R}{\tau_L}\hat{g} + \frac{T_R}{\tau_L}\hat{g}_0 - \frac{g_\mathrm{s}}{E_\mathrm{sat}}\left(\hat{E} + \hat{\xi}\right) \tag{G.2b}$$

with ∂_q arising from the slope of $q(E)$ around the steady state keeping solely the first order term:

$$q(E_\mathrm{s} + \hat{E}) \approx q(E_\mathrm{s}) + \left.\frac{\partial q}{\partial E}\right|_{E_\mathrm{s}} \hat{E} \equiv q(E_\mathrm{s}) + \partial_q \hat{E}$$

and r defined as:

$$r = 1 + \frac{\tau_L E_\mathrm{s}}{T_R E_\mathrm{sat}}\left(1 + \xi_\mathrm{s}/E_\mathrm{s}\right).$$

The hats denote the new variable which is being perturbed at the steady state condition. The "s" subscripted elements are the steady state scalar solutions of Eqs. G.1. After having the linearized equations, applying a Laplace transformation allows the analysis of the system in the complex plane. After some algebraic manipulation of the transformed equations, it is possible to write the model with a left side where the expression containing the poles of the system are multiplied with the Laplace space dependent $\tilde{E}(s)$. The right side of the equation contains any possible zero of the space and each of the terms – $\tilde{g}_0(s)$, $\tilde{\xi}(s)$, $\tilde{l}(s)$ – can be independently checked.

$$\begin{aligned}\frac{T_R^2}{E_\mathrm{s}}\Bigg[&\left(s + \frac{1}{2}\left\{\left(\frac{r}{\tau_L} + P_\mathrm{s}\partial_q\right) + \sqrt{\left(\frac{r}{\tau_L} + P_\mathrm{s}\partial_q\right)^2 - 4\left(P_\mathrm{s}\partial_q\frac{r}{\tau_L} + \frac{P_\mathrm{s}}{E_\mathrm{sat}T_R}\left[l_\mathrm{s} + q_\mathrm{s}\right]\right)}\right\}\right)\cdot \\ &\cdot\left(s + \frac{1}{2}\left\{\left(\frac{r}{\tau_L} + P_\mathrm{s}\partial_q\right) - \sqrt{\left(\frac{r}{\tau_L} + P_\mathrm{s}\partial_q\right)^2 - 4\left(P_\mathrm{s}\partial_q\frac{r}{\tau_L} + \frac{P_\mathrm{s}}{E_\mathrm{sat}T_R}\left[l_\mathrm{s} + q_\mathrm{s}\right]\right)}\right\}\right)\Bigg]\tilde{E}\end{aligned} \tag{G.3}$$

is the left side of the equation. $P_\mathrm{s} = E_\mathrm{s}/T_R$ is defined as the steady state power. The right side of the equation reads:

$$\frac{T_R}{\tau_L}\tilde{g}_0 - \frac{g_\mathrm{s}}{E_\mathrm{sat}}\tilde{\xi} - T_R\left(s + \frac{r}{\tau_L}\right)\tilde{l} \tag{G.4}$$

This form is different than the one presented in [53], but allows to better understand where the poles are, and also shows how modulation of the losses leads to a zero of the transfer function. This zero allows the phase to also lead instead of solely lag behind the attenuated double pole system, effectively increasing the bandwidth of the system. It also serves to show how the poles are mostly unchanged unless if r is substantially modified from the presence of ξ. The poles are usually imaginary, split from the real line by a small amount, typical of a stably attenuated double pole system, as is the case of mode-locked lasers via Kerr-lensing. Using SESAMs can bring the poles further from the real line, where the imaginary component is then much stronger, leading to a system displaying a non-attenuated resonant frequency (usually the relaxation oscillation frequency).

H | Additional Figures

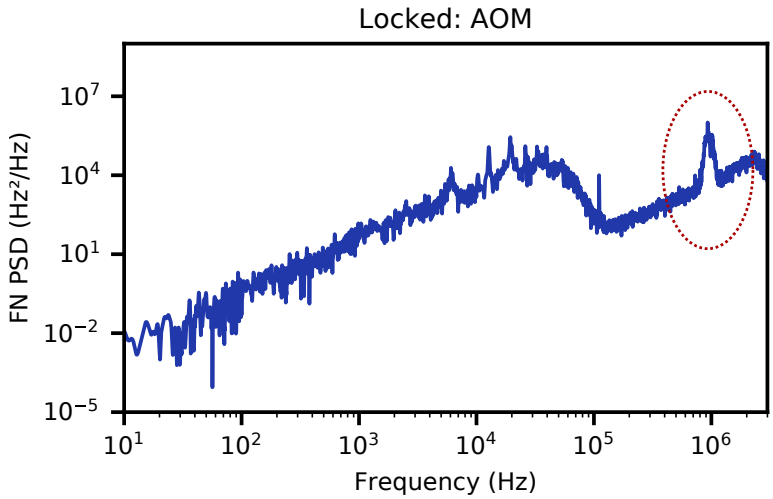

Figure H.1: Here's an example of the effect exposed in Section 6.2.2. The f_{CEO} was approximately 300 kHz away from a third of f_{rep}. The marked peak is the sum of all higher-harmonic f_{CEO} peaks.

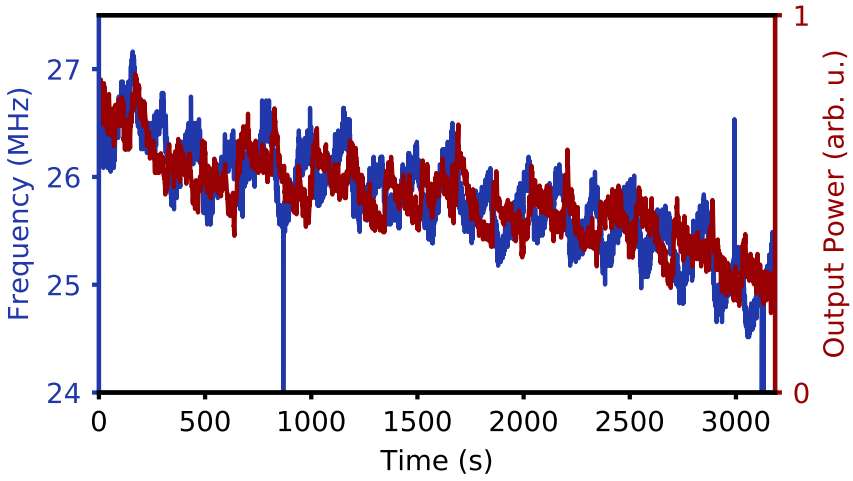

Figure H.2: Here is the total trace of the 10 min snippet of Figure 6.5 (from 1300 to ~1900 s). The overall trend of the f_{CEO} is to move with the output amplitude. However most of the mid term, 200 s excursions (usually from lower to higher frequency) show the opposite trend to that of the amplitude, seen by the two traces crossing.

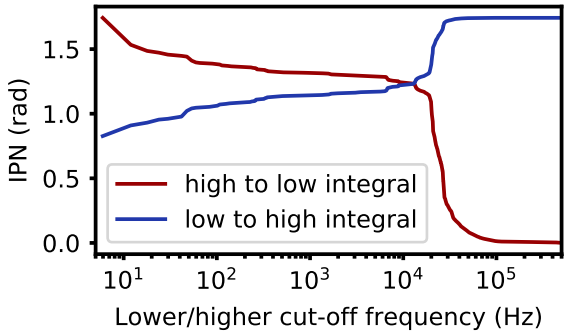

Figure H.3: IPN of the f_{CEO} lock using the control beam, using the low to high or high to low integral. Naturally both will integrate to the same value, as the end integral is of the whole function, however, the direction matters when it comes to the "shape" of the curve. Hence the footnote regarding the bad interpretation of such plots. The only true reading from these plots is the end integral and one could argue that looking at the steps is also giving information, but as one can see they are completely relative. This comes from the fact that as the integral is growing, the relative step becomes smaller after the square root. Take a certain step of the integral of the PN PSD (phase noise PSD) to be $\Delta\phi$. The end IPN step will either be $\Delta\theta_1 = \sqrt{\phi_1 + \Delta\phi} - \sqrt{\phi_1}$ for one integral, or $\Delta\theta_2 = \sqrt{\phi_2 + \Delta\phi} - \sqrt{\phi_2}$ for the integral in the opposite direction. If $\phi_2 > \phi_1$ then $\Delta\theta_1 > \Delta\theta_2$.

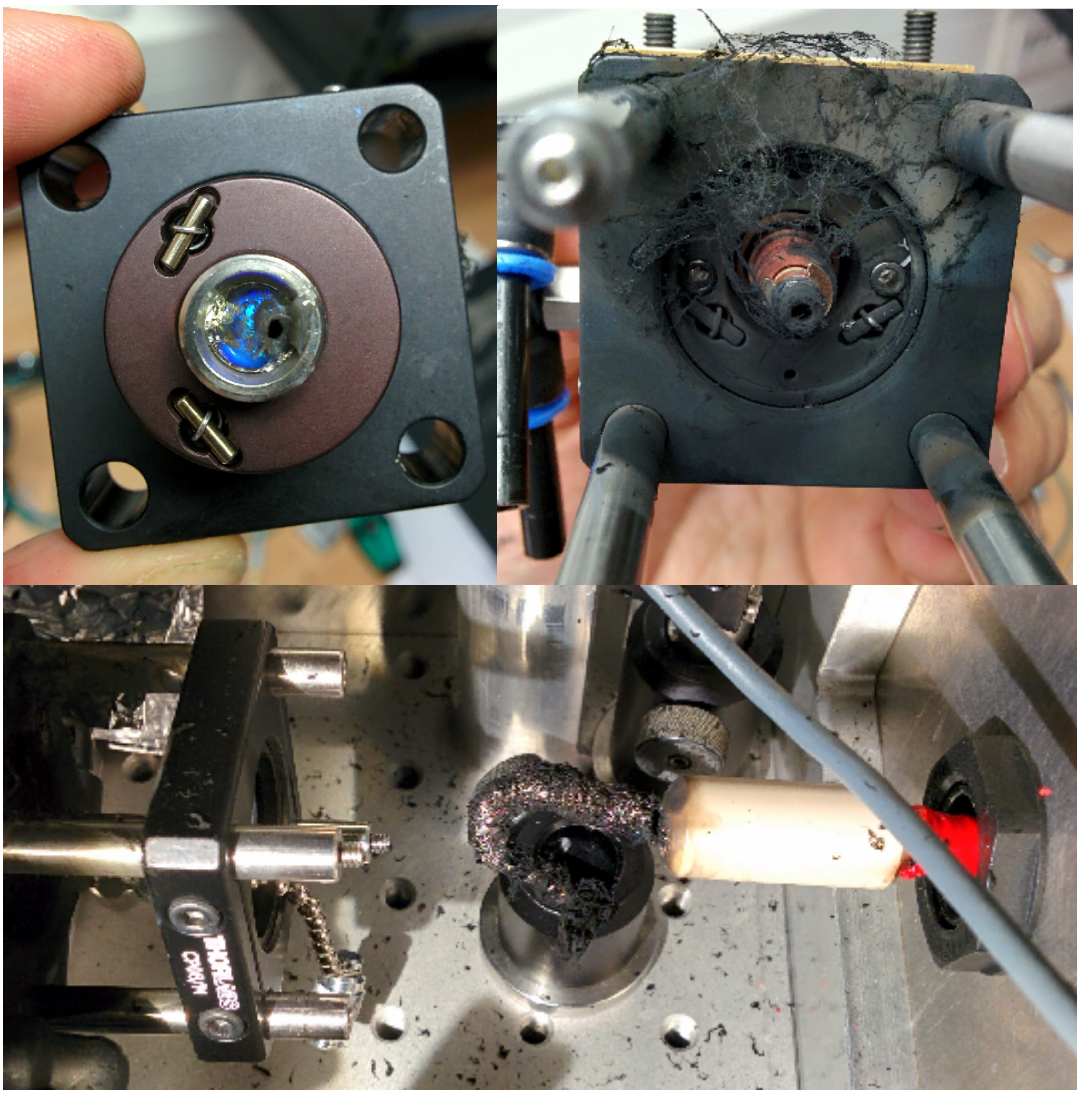

Figure H.4: Damage from ~110 W of pump power on the pump optics. Don't play with lasers kids!

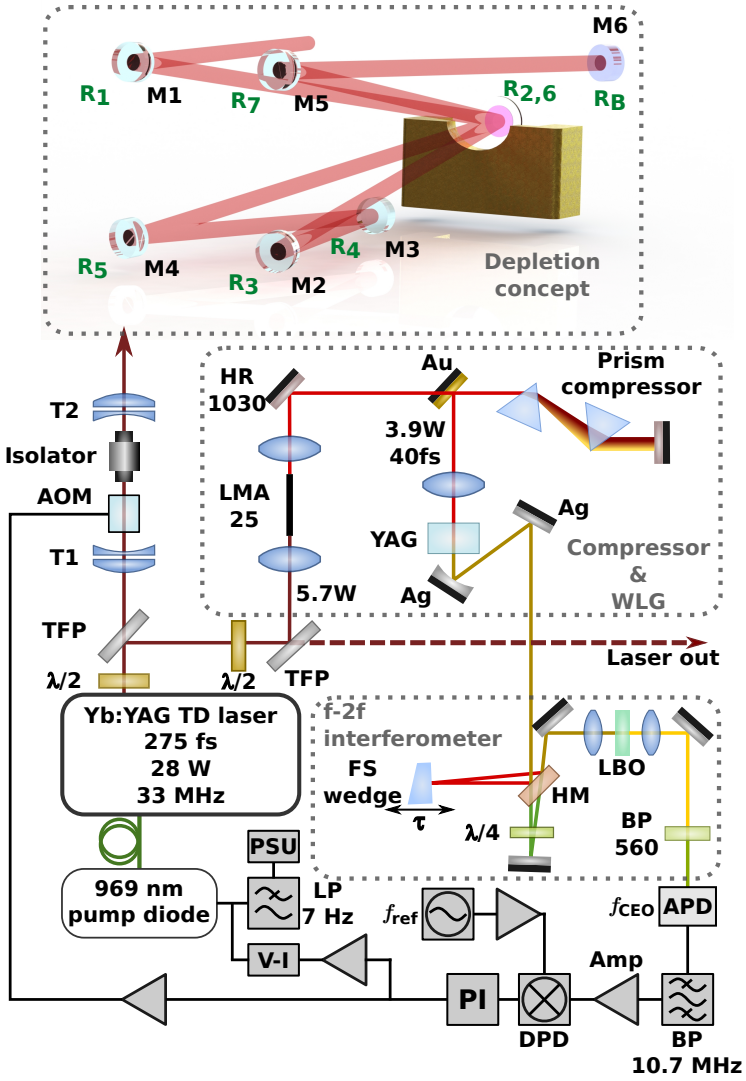

Figure H.5: Full schematic of the CEP stabilized laser

Bibliography

[1] B. N. Chichkov, C. Momma, S. Nolte, F. von Alvensleben, and A. Tünnermann, "Femtosecond, picosecond and nanosecond laser ablation of solids," *Applied Physics A*, vol. 63, pp. 109–115, Aug. 1996.

[2] I. Ratkay-Traub, T. Juhasz, C. Horvath, C. Suarez, K. Kiss, I. Ferincz, and R. Kurtz, "Ultra-short pulse (femtosecond) laser surgery: Initial use in LASIK flap creation," *Ophthalmology Clinics of North America*, vol. 14, pp. 347–355, viii–ix, June 2001.

[3] M. Ang, S. S. Chaurasia, R. I. Angunawela, R. Poh, A. Riau, D. Tan, and J. S. Mehta, "Femtosecond Lenticule Extraction (FLEx): Clinical Results, Interface Evaluation, and Intraocular Pressure Variation," *Investigative Ophthalmology & Visual Science*, vol. 53, pp. 1414–1421, Mar. 2012.

[4] N. Jowett, W. Wöllmer, R. Reimer, J. Zustin, U. Schumacher, P. W. Wiseman, A. M. Mlynarek, A. Böttcher, C. V. Dalchow, B. B. Lörincz, R. Knecht, and R. J. D. Miller, "Bone Ablation without Thermal or Acoustic Mechanical Injury via a Novel Picosecond Infrared Laser (PIRL)," *Otolaryngology–Head and Neck Surgery*, vol. 150, pp. 385–393, Mar. 2014.

[5] M. Baumgartl, M. Chemnitz, C. Jauregui, T. Meyer, B. Dietzek, J. Popp, J. Limpert, and A. Tünnermann, "All-fiber laser source for CARS microscopy based on fiber optical parametric frequency conversion," *Optics Express*, vol. 20, pp. 4484–4493, Feb. 2012.

[6] S. W. Hell and J. Wichmann, "Breaking the diffraction resolution limit by stimulated emission: Stimulated-emission-depletion fluorescence microscopy," *Optics Letters*, vol. 19, pp. 780–782, June 1994.

[7] A. H. Zewail, "Femtochemistry: Atomic-Scale Dynamics of the Chemical Bond Using Ultrafast Lasers (Nobel Lecture)," *Angewandte Chemie International Edition*, vol. 39, no. 15, pp. 2586–2631, 2000.

[8] T. Udem, R. Holzwarth, and T. W. Hänsch, "Optical frequency metrology," *Nature*, vol. 416, pp. 233–237, Mar. 2002.

[9] D. Strickland and G. Mourou, "Compression of amplified chirped optical pulses," *Optics Communications*, vol. 56, pp. 219–221, Dec. 1985.

[10] T. L. Cocker, D. Peller, P. Yu, J. Repp, and R. Huber, "Tracking the ultrafast motion of a single molecule by femtosecond orbital imaging," *Nature*, vol. 539, pp. 263–267, Nov. 2016.

[11] E. Goulielmakis, Z.-H. Loh, A. Wirth, R. Santra, N. Rohringer, V. S. Yakovlev, S. Zherebtsov, T. Pfeifer, A. M. Azzeer, M. F. Kling, S. R. Leone, and F. Krausz, "Real-time observation of valence electron motion," *Nature*, vol. 466, pp. 739–743, Aug. 2010.

[12] F. Lureau, O. Chalus, G. Matras, S. Laux, C. Radier, O. Casagrande, C. Derycke, S. Ricaud, G. Rey, T. Morbieu, A. Pellegrina, L. Boudjemaa, C. Simon-Boisson, A. Baleanu, R. Banici, A. Gradinariu, C. Caldararu, P. Ghenuche, A. Naziru, G. Kolliopoulos, L. Neagu, B. D. Boisdeffre, D. Ursescu, and I. Dancus, "10 petawatt lasers for extreme light applications," in *Solid State Lasers XXIX: Technology and Devices*, vol. 11259, p. 112591J, International Society for Optics and Photonics, Feb. 2020.

[13] U. Keller, W. H. Knox, and H. Roskos, "Coupled-cavity resonant passive mode-locked Ti:sapphire laser," *Optics Letters*, vol. 15, pp. 1377–1379, Dec. 1990.

[14] D. E. Spence, P. N. Kean, and W. Sibbett, "60-fsec pulse generation from a self-mode-locked Ti:sapphire laser," *Optics Letters*, vol. 16, pp. 42–44, Jan. 1991.

[15] L. E. Hargrove, R. L. Fork, and M. A. Pollack, "LOCKING OF He–Ne LASER MODES INDUCED BY SYNCHRONOUS INTRACAVITY MODULATION," *Applied Physics Letters*, vol. 5, pp. 4–5, July 1964.

[16] H. Fattahi, H. G. Barros, M. Gorjan, T. Nubbemeyer, B. Alsaif, C. Y. Teisset, M. Schultze, S. Prinz, M. Haefner, M. Ueffing, A. Alismail, L. Vámos, A. Schwarz, O. Pronin, J. Brons, X. T. Geng, G. Arisholm, M. Ciappina, V. S. Yakovlev, D.-E. Kim, A. M. Azzeer, N. Karpowicz, D. Sutter, Z. Major, T. Metzger, and F. Krausz, "Third-generation femtosecond technology," *Optica*, vol. 1, pp. 45–63, July 2014.

[17] C. Jauregui, J. Limpert, and A. Tünnermann, "High-power fibre lasers," *Nature Photonics*, vol. 7, pp. 861–867, Nov. 2013.

[18] P. Russbueldt, D. Hoffmann, M. Höfer, J. Löhring, J. Luttmann, A. Meissner, J. Weitenberg, M. Traub, T. Sartorius, D. Esser, R. Wester, P. Loosen, and R. Poprawe, "Innoslab Amplifiers," *IEEE Journal of Selected Topics in Quantum Electronics*, vol. 21, pp. 447–463, Jan. 2015.

[19] C. J. Saraceno, D. Sutter, T. Metzger, and M. Abdou Ahmed, "The amazing progress of high-power ultrafast thin-disk lasers," *Journal of the European Optical Society-Rapid Publications*, vol. 15, p. 15, June 2019.

[20] A. Klenke, M. Müller, H. Stark, M. Kienel, C. Jauregui, A. Tünnermann, and J. Limpert, "Coherent Beam Combination of Ultrafast Fiber Lasers," *IEEE Journal of Selected Topics in Quantum Electronics*, vol. 24, pp. 1–9, Sept. 2018.

[21] F. Stutzki, H.-J. Otto, F. Jansen, C. Gaida, C. Jauregui, J. Limpert, and A. Tünnermann, "High-speed modal decomposition of mode instabilities in high-power fiber lasers," *Optics Letters*, vol. 36, pp. 4572–4574, Dec. 2011.

[22] R. Jung, J. Tümmler, T. Nubbemeyer, and I. Will, "Thin-disk ring amplifier for high pulse energy," *Optics Express*, vol. 24, pp. 4375–4381, Mar. 2016.

[23] J. Zhang, J. Brons, N. Lilienfein, E. Fedulova, V. Pervak, D. Bauer, D. Sutter, Z. Wei, A. Apolonski, O. Pronin, and F. Krausz, "260-megahertz, megawatt-level thin-disk oscillator," *Optics Letters*, vol. 40, pp. 1627–1630, Apr. 2015.

[24] T. Dietz, T. Dietz, M. Jenne, D. Bauer, M. Scharun, D. Sutter, and A. Killi, "Ultrafast thin-disk multi-pass amplifier system providing 1.9 kW of average output power and pulse energies in the 10 mJ range at 1 ps of pulse duration for glass-cleaving applications," *Optics Express*, vol. 28, pp. 11415–11423, Apr. 2020.

[25] N. Modsching, C. Paradis, F. Labaye, M. Gaponenko, I. J. Graumann, A. Diebold, F. Emaury, V. J. Wittwer, and T. Südmeyer, "Kerr lens mode-locked Yb:CALGO thin-disk laser," *Optics Letters*, vol. 43, pp. 879–882, Feb. 2018.

[26] O. Pronin, J. Brons, C. Grasse, V. Pervak, G. Boehm, M.-C. Amann, V. L. Kalashnikov, A. Apolonski, and F. Krausz, "High-power 200 fs Kerr-lens mode-locked Yb:YAG thin-disk oscillator," *Optics Letters*, vol. 36, pp. 4746–4748, Dec. 2011.

[27] A. A. Eilanlou, Y. Nabekawa, M. Kuwata-Gonokami, and K. Midorikawa, "Femtosecond laser pulses in a Kerr lens mode-locked thin-disk ring oscillator with an intra-cavity peak power beyond 100 MW," *Japanese Journal of Applied Physics*, vol. 53, p. 082701, July 2014.

[28] J. Brons, V. Pervak, E. Fedulova, D. Bauer, D. Sutter, V. Kalashnikov, A. Apolonskiy, O. Pronin, and F. Krausz, "Energy scaling of Kerr-lens mode-locked thin-disk oscillators," *Optics Letters*, vol. 39, pp. 6442–6445, Nov. 2014.

[29] J. Brons, V. Pervak, D. Bauer, D. Sutter, O. Pronin, and F. Krausz, "Powerful 100-fs-scale Kerr-lens mode-locked thin-disk oscillator," *Optics Letters*, vol. 41, pp. 3567–3570, Aug. 2016.

[30] J. Aus der Au, G. J. Spühler, T. Südmeyer, R. Paschotta, R. Hövel, M. Moser, S. Erhard, M. Karszewski, A. Giesen, and U. Keller, "16.2-W average power from a diode-pumped femtosecond Yb:YAG thin disk laser," *Optics Letters*, vol. 25, pp. 859–861, June 2000.

[31] E. Innerhofer, T. Südmeyer, F. Brunner, R. Häring, A. Aschwanden, R. Paschotta, C. Hönninger, M. Kumkar, and U. Keller, "60-W average power in 810-fs pulses from a thin-disk Yb:YAG laser," *Optics Letters*, vol. 28, pp. 367–369, Mar. 2003.

[32] S. V. Marchese, T. Südmeyer, M. Golling, R. Grange, and U. Keller, "Pulse energy scaling to 5 ?J from a femtosecond thin disk laser," *Optics Letters*, vol. 31, pp. 2728–2730, Sept. 2006.

[33] S. V. Marchese, C. R. Baer, A. G. Engqvist, S. Hashimoto, D. J. Maas, M. Golling, T. Südmeyer, and U. Keller, "Femtosecond thin disk laser oscillator with pulse energy beyond the 10-microjoule level," *Optics Express*, vol. 16, pp. 6397–6407, Apr. 2008.

[34] J. Neuhaus, D. Bauer, J. Zhang, A. Killi, J. Kleinbauer, M. Kumkar, S. Weiler, M. Guina, D. H. Sutter, and T. Dekorsy, "Subpicosecond thin-disk laser oscillator with pulse energies of up to 25.9 microjoules by use of an active multipass geometry," *Optics Express*, vol. 16, pp. 20530–20539, Dec. 2008.

[35] C. J. Saraceno, F. Emaury, O. H. Heckl, C. R. E. Baer, M. Hoffmann, C. Schriber, M. Golling, T. Südmeyer, and U. Keller, "275 W average output power from a femtosecond thin disk oscillator operated in a vacuum environment," *Optics Express*, vol. 20, pp. 23535–23541, Oct. 2012.

[36] F. Saltarelli, I. J. Graumann, L. Lang, D. Bauer, C. R. Phillips, and U. Keller, "Power scaling of ultrafast oscillators: 350-W average-power sub-picosecond thin-disk laser," *Optics Express*, vol. 27, pp. 31465–31474, Oct. 2019.

[37] C. Paradis, N. Modsching, V. J. Wittwer, B. Deppe, C. Krankel, and T. Südmeyer, "Generation of 35-fs pulses from a Kerr lens mode-locked Yb:Lu2O3 thin-disk laser," *Opt. Express*, vol. 25, pp. 14918–14925, July 2017.

[38] N. Modsching, J. Drs, J. Fischer, C. Paradis, F. Labaye, M. Gaponenko, C. Kränkel, V. J. Wittwer, and T. Südmeyer, "Sub-100-fs Kerr lens mode-locked Yb:Lu_2O_3 thin-disk laser oscillator operating at 21 W average power," *Optics Express*, vol. 27, pp. 16111–16120, May 2019.

[39] S. V. Marchese, C. R. E. Baer, R. Peters, C. Kränkel, A. G. Engqvist, M. Golling, D. J. H. C. Maas, K. Petermann, T. Südmeyer, G. Huber, and U. Keller, "Efficient femtosecond high power Yb:Lu2O3 thin disk laser," *Optics Express*, vol. 15, pp. 16966–16971, Dec. 2007.

[40] C. R. E. Baer, C. Kränkel, C. J. Saraceno, O. H. Heckl, M. Golling, T. Südmeyer, R. Peters, K. Petermann, G. Huber, and U. Keller, "Femtosecond Yb:Lu_2O_3 thin disk laser with 63 W of average power," *Optics Letters*, vol. 34, pp. 2823–2825, Sept. 2009.

[41] C. R. E. Baer, C. Kränkel, C. J. Saraceno, O. H. Heckl, M. Golling, R. Peters, K. Petermann, T. Südmeyer, G. Huber, and U. Keller, "Femtosecond thin-disk laser with 141 W of average power," *Optics Letters*, vol. 35, pp. 2302–2304, July 2010.

[42] C. J. Saraceno, S. Pekarek, O. H. Heckl, C. R. E. Baer, C. Schriber, M. Golling, K. Beil, C. Kränkel, G. Huber, U. Keller, and T. Südmeyer, "Self-referenceable frequency comb from an ultrafast thin disk laser," *Optics Express*, vol. 20, pp. 9650–9656, Apr. 2012.

[43] C. J. Saraceno, O. H. Heckl, C. R. E. Baer, M. Golling, T. Südmeyer, K. Beil, C. Kränkel, K. Petermann, G. Huber, and U. Keller, "SESAMs for high-power femtosecond modelocking: Power scaling of an Yb:LuScO3 thin disk laser to 23 W and 235 fs," *Optics Express*, vol. 19, pp. 20288–20300, Oct. 2011.

[44] C. J. Saraceno, O. H. Heckl, C. R. E. Baer, C. Schriber, M. Golling, K. Beil, C. Kränkel, T. Südmeyer, G. Huber, and U. Keller, "Sub-100 femtosecond pulses from a SESAM modelocked thin disk laser," *Applied Physics B*, vol. 106, pp. 559–562, Mar. 2012.

[45] S. Ricaud, A. Jaffres, K. Wentsch, A. Suganuma, B. Viana, P. Loiseau, B. Weichelt, M. Abdou-Ahmed, A. Voss, T. Graf, D. Rytz, C. Hönninger, E. Mottay, P. Georges, and F. Druon, "Femtosecond Yb:$CaGdAlO_4$ thin-disk oscillator," *Optics Letters*, vol. 37, pp. 3984–3986, Oct. 2012.

[46] A. Diebold, F. Emaury, C. Schriber, M. Golling, C. J. Saraceno, T. Südmeyer, and U. Keller, "SESAM mode-locked Yb:$CaGdAlO_4$ thin disk laser with 62 fs pulse generation," *Optics Letters*, vol. 38, pp. 3842–3845, Oct. 2013.

[47] A. Klenner, F. Emaury, C. Schriber, A. Diebold, C. J. Saraceno, S. Schilt, U. Keller, and T. Südmeyer, "Phase-stabilization of the carrier-envelope-offset frequency of a SESAM modelocked thin disk laser," *Optics Express*, vol. 21, pp. 24770–24780, Oct. 2013.

[48] F. Emaury, A. Diebold, A. Klenner, C. J. Saraceno, S. Schilt, T. Südmeyer, and U. Keller, "Frequency comb offset dynamics of SESAM modelocked thin disk lasers," *Optics Express*, vol. 23, pp. 21836–21856, Aug. 2015.

[49] N. Modsching, C. Paradis, P. Brochard, N. Jornod, K. Gürel, C. Kränkel, S. Schilt, V. J. Wittwer, and T. Südmeyer, "Carrier-envelope offset frequency stabilization of a thin-disk laser oscillator operating in the strongly self-phase modulation broadened regime," *Optics Express*, vol. 26, pp. 28461–28468, Oct. 2018.

[50] O. Pronin, M. Seidel, F. Lücking, J. Brons, E. Fedulova, M. Trubetskov, V. Pervak, A. Apolonski, T. Udem, and F. Krausz, "High-power multi-megahertz source of waveform-stabilized few-cycle light," *Nature Communications*, vol. 6, May 2015.

[51] M. Seidel, J. Brons, F. Lücking, V. Pervak, A. Apolonski, T. Udem, and O. Pronin, "Carrier-envelope-phase stabilization via dual wavelength pumping," *Optics Letters*, vol. 41, pp. 1853–1856, Apr. 2016.

[52] S. Gröbmeyer, J. Brons, M. Seidel, and O. Pronin, "Carrier-Envelope-Offset Frequency Stable 100 W-Level Femtosecond Thin-Disk Oscillator," *Laser & Photonics Reviews*, vol. 13, no. 3, p. 1800256, 2019.

[53] J. R. C. Andrade, N. Modsching, A. Tajalli, C. M. Dietrich, S. Kleinert, F. Placzek, B. Kreipe, S. Schilt, V. J. Wittwer, T. Südmeyer, and U. Morgner, "Carrier-Envelope Offset Frequency Stabilization of a Thin-Disk Laser Oscillator via Depletion Modulation," *IEEE Photonics Journal*, vol. 12, pp. 1–9, Apr. 2020.

[54] R. W. Boyd, *Nonlinear Optics*. Academic Press, third ed., 2008.

[55] J. H. Marburger, "Self-focusing: Theory," *Progress in Quantum Electronics*, vol. 4, pp. 35–110, Apr. 1975.

[56] V. Magni, G. Cerullo, S. D. Silvestri, and A. Monguzzi, "Astigmatism in Gaussian-beam self-focusing and in resonators for Kerr-lens mode locking," *JOSA B*, vol. 12, pp. 476–485, Mar. 1995.

[57] G. Fibich and B. Ilan, "Self-focusing of elliptic beams: An example of the failure of the aberrationless approximation," *JOSA B*, vol. 17, pp. 1749–1758, Oct. 2000.

[58] F. Salin, J. Squier, and M. Piché, "Mode locking of Ti:Al_2O_3 lasers and self-focusing: A Gaussian approximation," *Optics Letters*, vol. 16, pp. 1674–1676, Nov. 1991.

[59] G. Agrawal, *Nonlinear Fiber Optics*. Optics and Photonics, Academic Press, fifth ed., 2013.

[60] H. A. Haus, "Theory of mode locking with a fast saturable absorber," *Journal of Applied Physics*, vol. 46, pp. 3049–3058, July 1975.

[61] T. Brabec, C. Spielmann, and F. Krausz, "Mode locking in solitary lasers," *Optics Letters*, vol. 16, pp. 1961–1963, Dec. 1991.

[62] S. Kelly, "Characteristic sideband instability of periodically amplified average soliton," *Electronics Letters*, vol. 28, pp. 806–807, Apr. 1992.

[63] F. X. Kärtner and U. Keller, "Stabilization of solitonlike pulses with a slow saturable absorber," *Optics Letters*, vol. 20, pp. 16–18, Jan. 1995.

[64] F. Kartner, I. Jung, and U. Keller, "Soliton mode-locking with saturable absorbers," *IEEE Journal of Selected Topics in Quantum Electronics*, vol. 2, pp. 540–556, Sept. 1996.

[65] F. Kartner, J. der Au, and U. Keller, "Mode-locking with slow and fast saturable absorbers-what's the difference?," *IEEE Journal of Selected Topics in Quantum Electronics*, vol. 4, pp. 159–168, Mar. 1998.

[66] H. Haus, "Mode-locking of lasers," *IEEE Journal of Selected Topics in Quantum Electronics*, vol. 6, pp. 1173–1185, Nov. 2000.

[67] R. Grange, M. Haiml, R. Paschotta, G. Spühler, L. Krainer, M. Golling, O. Ostinelli, and U. Keller, "New regime of inverse saturable absorption for self-stabilizing passively mode-locked lasers," *Applied Physics B*, vol. 80, pp. 151–158, Feb. 2005.

[68] M. Hofmann, J. Hyyti, S. Birkholz, M. Bock, S. K. Das, R. Grunwald, M. Hoffmann, T. Nagy, A. Demircan, M. Jupé, D. Ristau, U. Morgner, C. Brée, M. Woerner, T. Elsaesser, and G. Steinmeyer, "Noninstantaneous polarization dynamics in dielectric media," *Optica*, vol. 2, pp. 151–157, Feb. 2015.

[69] V. Kalashnikov, E. Podivilov, A. Chernykh, and A. Apolonski, "Chirped-pulse oscillators: Theory and experiment," *Applied Physics B*, vol. 83, p. 503, Apr. 2006.

[70] D. J. Jones, S. A. Diddams, J. K. Ranka, A. Stentz, R. S. Windeler, J. L. Hall, and S. T. Cundiff, "Carrier-Envelope Phase Control of Femtosecond Mode-Locked Lasers and Direct Optical Frequency Synthesis," *Science*, vol. 288, no. 5466, pp. 635–639, 2000.

[71] J. R. C. Andrade, *Pulse Shaping and Characterization of Spectra Exceeding One Octave*. Master Thesis, Leibniz Universität Hannover, Hannover, 2013.

[72] H. Telle, G. Steinmeyer, A. Dunlop, J. Stenger, D. Sutter, and U. Keller, "Carrier-envelope offset phase control: A novel concept for absolute optical frequency measurement and ultrashort pulse generation," *Applied Physics B*, vol. 69, pp. 327–332, Oct. 1999.

[73] H. Kogelnik and T. Li, "Laser Beams and Resonators," *Applied Optics*, vol. 5, pp. 1550–1567, Oct. 1966.

[74] A. Giesen, H. Hügel, A. Voss, K. Wittig, U. Brauch, and H. Opower, "Scalable concept for diode-pumped high-power solid-state lasers," *Applied Physics B*, vol. 58, pp. 365–372, May 1994.

[75] A. Giesen and J. Speiser, "Fifteen Years of Work on Thin-Disk Lasers: Results and Scaling Laws," *IEEE Journal of Selected Topics in Quantum Electronics*, vol. 13, pp. 598–609, May 2007.

[76] W. H. Lowdermilk and J. E. Murray, "The multipass amplifier: Theory and numerical analysis," *Journal of Applied Physics*, vol. 51, pp. 2436–2444, May 1980.

[77] C. R. E. Baer, O. H. Heckl, C. J. Saraceno, C. Schriber, C. Kränkel, T. Südmeyer, and U. Keller, "Frontiers in passively mode-locked high-power thin disk laser oscillators," *Optics Express*, vol. 20, pp. 7054–7065, Mar. 2012.

[78] J. Koerner, C. Vorholt, H. Liebetrau, M. Kahle, D. Kloepfel, R. Seifert, J. Hein, and M. C. Kaluza, "Measurement of temperature-dependent absorption and emission spectra of Yb:YAG, Yb:LuAG, and Yb:CaF_2 between 20 °C and 200 °C and predictions on their influence on laser performance," *JOSA B*, vol. 29, pp. 2493–2502, Sept. 2012.

[79] O. Casagrande, N. Deguil-Robin, B. Le Garrec, and G. L. Bourdet, "Time and Spectrum Resolved Model for Quasi-Three-Level Gain-Switched Lasers," *IEEE Journal of Quantum Electronics*, vol. 43, pp. 206–212, Feb. 2007.

[80] M. Behringer, "High-Power Diode Laser Technology and Characteristics," in *High Power Diode Lasers: Technology and Applications* (F. Bachmann, P. Loosen, and R. Poprawe, eds.), Springer Series in Optical Sciences, pp. 5–74, New York, NY: Springer, 2007.

[81] B. Weichelt, A. Voss, M. A. Ahmed, and T. Graf, "Enhanced performance of thin-disk lasers by pumping into the zero-phonon line," *Optics Letters*, vol. 37, pp. 3045–3047, Aug. 2012.

[82] M. Smrž, T. Miura, M. Chyla, S. Nagisetty, O. Novák, A. Endo, and T. Mocek, "Suppression of nonlinear phonon relaxation in Yb:YAG thin disk via zero phonon line pumping," *Optics Letters*, vol. 39, pp. 4919–4922, Aug. 2014.

[83] D. Brown, R. Cone, Y. Sun, and R. Equall, "Yb:YAG absorption at ambient and cryogenic temperatures," *IEEE Journal of Selected Topics in Quantum Electronics*, vol. 11, pp. 604–612, May 2005.

[84] J. Schulte, T. Sartorius, J. Weitenberg, A. Vernaleken, and P. Russbueldt, "Nonlinear pulse compression in a multi-pass cell," *Optics Letters*, vol. 41, pp. 4511–4514, Oct. 2016.

[85] K. Fritsch, M. Poetzlberger, V. Pervak, J. Brons, and O. Pronin, "All-solid-state multipass spectral broadening to sub-20 fs," *Optics Letters*, vol. 43, pp. 4643–4646, Oct. 2018.

[86] C.-L. Tsai, F. Meyer, A. Omar, Y. Wang, A.-Y. Liang, C.-H. Lu, S.-D. Yang, and C. J. Saraceno, "27-fs, 166-MW pulses at 98 W average power from highly efficient thin-disk oscillator driven nonlinear compressor," in *Conference on Lasers and Electro-Optics (2019), Paper JTh5A.4*, p. JTh5A.4, Optical Society of America, May 2019.

[87] J. Brons, *High-power femtosecond laser-oscillators for applications in high-field physics*. PhDThesis, Ludwig-Maximilians-Universität München, Mar. 2017.

[88] G. Herink, B. Jalali, C. Ropers, and D. R. Solli, "Resolving the build-up of femtosecond mode-locking with single-shot spectroscopy at 90 MHz frame rate," *Nature Photonics*, vol. advance online publication, Mar. 2016.

[89] T. Lang, T. Binhammer, S. Rausch, G. Palmer, M. Emons, M. Schultze, A. Harth, and U. Morgner, "High power ultra-widely tuneable femtosecond pulses from a non-collinear optical parametric oscillator (NOPO)," *Optics Express*, vol. 20, pp. 912–917, Jan. 2012.

[90] Y. Khanukaeva, T. Lang, A. Tajalli, J. R. C. Andrade, T. Binhammer, and U. Morgner, "Fast-tunable femtosecond visible radiation via intracavity sumfrequency generation in a NIR NOPO," in *7th EPS-QEOD Europhoton Conference*, (Vienna), 2016.

[91] Y. Binhammer, T. Binhammer, F. Placzek, B. Kreipe, J. R. Andrade, T. Lang, A. Tajalli, and U. Morgner, "Widely tunable femtosecond non-collinear optical parametric oscillator (NOPO) in VIS," in *The European Conference on Lasers and Electro-Optics*, p. CF_P_24, Optical Society of America, 2017.

[92] L. Beichert, Y. Binhammer, J. R. C. Andrade, A. K. Kniggendorf, and U. Morgner, "Non-collinear Optical Parametric Oscillator for Video-Rate Stimulated Raman Spectroscopy of Microplastics," in *8th EPS-QEOD Europhoton Conference*, (Barcelona), 2018.

[93] C. M. Dietrich, I. Babushkin, J. R. C. Andrade, H. Rao, A. Demircan, and U. Morgner, "Field enhancement in a doubly resonant optical parametric oscillator," *Optics Letters*, vol. 44, pp. 4909–4912, Oct. 2019.

[94] T. Dietrich, S. Piehler, C. Röcker, M. Rumpel, M. A. Ahmed, and T. Graf, "Passive compensation of the misalignment instability caused by air convection in thin-disk lasers," *Optics Letters*, vol. 42, pp. 3263–3266, Sept. 2017.

[95] D. Milam, "Review and assessment of measured values of the nonlinear refractive-index coefficient of fused silica," *Applied Optics*, vol. 37, pp. 546–550, Jan. 1998.

[96] A. Major, F. Yoshino, I. Nikolakakos, J. S. Aitchison, and P. W. E. Smith, "Dispersion of the nonlinear refractive index in sapphire," *Optics Letters*, vol. 29, pp. 602–604, Mar. 2004.

[97] "Silica Glass (SiO2) Optical Material." https://www.crystran.co.uk/optical-materials/silica-glass-sio2.

[98] "Sapphire Optical Material." https://www.crystran.co.uk/optical-materials/sapphire-al2o3.

[99] T. Toyoda and M. Yabe, "The temperature dependence of the refractive indices of fused silica and crystal quartz," *Journal of Physics D: Applied Physics*, vol. 16, pp. L97–L100, May 1983.

[100] J. Tapping and M. L. Reilly, "Index of refraction of sapphire between 24 and 1060°C for wavelengths of 633 and 799 nm," *JOSA A*, vol. 3, pp. 610–616, May 1986.

[101] Á. Börzsönyi, Z. Heiner, A. Kovács, M. P. Kalashnikov, and K. Osvay, "Measurement of pressure dependent nonlinear refractive index of inert gases," *Optics Express*, vol. 18, pp. 25847–25854, Dec. 2010.

[102] C. Paradis, *Novel Ultrafast High-Power Thin-Disk Laser Oscillators and Applications for Metrology and XUV Generation*. PhD thesis, Dec. 2017.

[103] H. Kogelnik, E. Ippen, A. Dienes, and C. Shank, "Astigmatically compensated cavities for CW dye lasers," *IEEE Journal of Quantum Electronics*, vol. 8, pp. 373–379, Mar. 1972.

[104] A. Gerrard and J. M. Burch, *Introduction to Matrix Methods in Optics*. Courier Corporation, Jan. 1994.

[105] M. Brunel, H. Shen, S. Coetmellec, and D. Lebrun, "Extended ABCD matrix formalism for the description of femtosecond diffraction patterns; application to femtosecond digital in-line holography with anamorphic optical systems," *Applied Optics*, vol. 51, pp. 1137–1148, Mar. 2012.

[106] S. Gatz and J. Hermann, "Geometrical threshold zones and Gaussian modes in lasers with radially varying gain," *Optics Letters*, vol. 19, pp. 1696–1698, Nov. 1994.

[107] G. Winkler, J. Fellinger, J. Seres, E. Seres, and T. Schumm, "Non-planar femtosecond enhancement cavity for VUV frequency comb applications," *Optics Express*, vol. 24, pp. 5253–5262, Mar. 2016.

[108] H. Carstens, S. Holzberger, J. Kaster, J. Weitenberg, V. Pervak, A. Apolonski, E. Fill, F. Krausz, and I. Pupeza, "Large-mode enhancement cavities," *Optics Express*, vol. 21, pp. 11606–11617, May 2013.

[109] V. Magni, G. Cerullo, and S. De Silvestri, "Closed form gaussian beam analysis of resonators containing a Kerr medium for femtosecond lasers," *Optics Communications*, vol. 101, pp. 365–370, Sept. 1993.

[110] G. Cerullo, S. D. Silvestri, V. Magni, and L. Pallaro, "Resonators for Kerr-lens mode-locked femtosecond Ti:sapphire lasers," *Optics Letters*, vol. 19, pp. 807–809, June 1994.

[111] V. Magni, "Perturbation theory of nonlinear resonators with an application to Kerr-lens mode locking," *JOSA B*, vol. 13, pp. 2498–2507, Nov. 1996.

[112] A. Penzkofer, M. Wittmann, M. Lorenz, E. Siegert, and S. Macnamara, "Kerr lens effects in a folded-cavity four-mirror linear resonator," *Optical and Quantum Electronics*, vol. 28, pp. 423–442, Apr. 1996.

[113] R. Storn and K. Price, "Differential Evolution – A Simple and Efficient Heuristic for global Optimization over Continuous Spaces," *Journal of Global Optimization*, vol. 11, pp. 341–359, Dec. 1997.

[114] E. Grace, A. Ritsataki, P. French, and G. New, "New optimization criteria for slit-apertured and gain-apertured KLM all-solid-state lasers," *Optics Communications*, vol. 183, pp. 249–264, Sept. 2000.

[115] Y. W. Lee, J. H. Yi, Y. H. Cha, Y. J. Rhee, B. C. Lee, and B. D. Yoo, "Numerical Analysis of Soft-Aperture Kerr-Lens Mode Locking in Ti:Sapphire Laser Cavities by Using Nonlinear ABCD Matrices," *Journal Of Korean Physical Society*, vol. 46, pp. 1131–1136, May 2005.

[116] S. Yefet and A. Pe'er, "A Review of Cavity Design for Kerr Lens Mode-Locked Solid-State Lasers," *Applied Sciences*, vol. 3, pp. 694–724, Dec. 2013.

[117] R. Y. Chiao, E. Garmire, and C. H. Townes, "Self-Trapping of Optical Beams," *Physical Review Letters*, vol. 13, pp. 479–482, Oct. 1964.

[118] J. A. Nelder and R. Mead, "A Simplex Method for Function Minimization," *The Computer Journal*, vol. 7, pp. 308–313, Jan. 1965.

[119] J. Herrmann, "Theory of Kerr-lens mode locking: Role of self-focusing and radially varying gain," *JOSA B*, vol. 11, pp. 498–512, Mar. 1994.

[120] O. Haderka, "Influence of diffraction on hard-aperture Kerr-lens mode locking," *Optics Letters*, vol. 20, pp. 240–242, Feb. 1995.

[121] E. T. J. Nibbering, G. Grillon, M. A. Franco, B. S. Prade, and A. Mysyrowicz, "Determination of the inertial contribution to the nonlinear refractive index of air, N_2, and O_2 by use of unfocused high-intensity femtosecond laser pulses," *JOSA B*, vol. 14, pp. 650–660, Mar. 1997.

[122] E. Seres, J. Seres, and C. Spielmann, "Extreme ultraviolet light source based on intracavity high harmonic generation in a mode locked Ti:sapphire oscillator with 9.4 MHz repetition rate," *Optics Express*, vol. 20, pp. 6185–6190, Mar. 2012.

[123] F. Labaye, M. Gaponenko, V. J. Wittwer, A. Diebold, C. Paradis, N. Modsching, L. Merceron, F. Emaury, I. J. Graumann, C. R. Phillips, C. J. Saraceno, C. Kränkel, U. Keller, and T. Südmeyer, "Extreme ultraviolet light source at a megahertz repetition rate based on high-harmonic generation inside a mode-locked thin-disk laser oscillator," *Optics Letters*, vol. 42, pp. 5170–5173, Dec. 2017.

[124] F. Labaye, M. Gaponenko, N. Modsching, P. Brochard, C. Paradis, S. Schilt, V. J. Wittwer, and T. Südmeyer, "XUV Sources Based on Intra-Oscillator High Harmonic Generation With Thin-Disk Lasers: Current Status and Prospects," *IEEE Journal of Selected Topics in Quantum Electronics*, vol. 25, pp. 1–19, July 2019.

[125] R. Peters, C. Kränkel, S. T. Fredrich-Thornton, K. Beil, K. Petermann, G. Huber, O. H. Heckl, C. R. E. Baer, C. J. Saraceno, T. Südmeyer, and U. Keller, "Thermal analysis and efficient high power continuous-wave and mode-locked thin disk laser operation of Yb-doped sesquioxides," *Applied Physics B*, vol. 102, pp. 509–514, Mar. 2011.

[126] R. Peters, C. Kränkel, K. Petermann, and G. Huber, "Broadly tunable high-power Yb:Lu_2O_3 thin disk laser with 80% slope efficiency," *Optics Express*, vol. 15, pp. 7075–7082, May 2007.

[127] T. Südmeyer, C. Kränkel, C. R. E. Baer, O. H. Heckl, C. J. Saraceno, M. Golling, R. Peters, K. Petermann, G. Huber, and U. Keller, "High-power ultrafast thin disk laser oscillators and their potential for sub-100-femtosecond pulse generation," *Applied Physics B*, vol. 97, p. 281, Sept. 2009.

[128] O. Pronin, *Towards a Compact Thin-Disk-Based Femtosecond XUV Source*. PhD thesis, Ludwig-Maximilians -Universität München, Munich, Aug. 2012.

[129] B. Kreipe, *Yb:LuO Thin-Disk Lasers*. In preparation, Leibniz Universität Hannover, 2020.

[130] B. Kreipe, J. R. C. de Andrade, C. Kränkel, and U. Morgner, "Kerr-lens mode-locked Yb3+:Lu2O3 thin-disk laser," in *2016 Conference on Lasers and Electro-Optics (CLEO)*, pp. 1–2, June 2016.

[131] T. Udem, J. Reichert, R. Holzwarth, and T. W. Hänsch, "Accurate measurement of large optical frequency differences with a mode-locked laser," *Optics Letters*, vol. 24, pp. 881–883, July 1999.

[132] G. Sansone, E. Benedetti, F. Calegari, C. Vozzi, L. Avaldi, R. Flammini, L. Poletto, P. Villoresi, C. Altucci, R. Velotta, S. Stagira, S. D. Silvestri, and M. Nisoli, "Isolated Single-Cycle Attosecond Pulses," *Science*, vol. 314, pp. 443–446, Oct. 2006.

[133] M. T. Hassan, T. T. Luu, A. Moulet, O. Raskazovskaya, P. Zhokhov, M. Garg, N. Karpowicz, A. M. Zheltikov, V. Pervak, F. Krausz, and E. Goulielmakis, "Optical attosecond pulses and tracking the nonlinear response of bound electrons," *Nature*, vol. 530, pp. 66–70, Feb. 2016.

[134] I. Babushkin, C. Brée, C. M. Dietrich, A. Demircan, U. Morgner, and A. Husakou, "Terahertz and higher-order Brunel harmonics: From tunnel to multiphoton ionization regime in tailored fields," *Journal of Modern Optics*, vol. 64, pp. 1078–1087, June 2017.

[135] M. Seidel, "Proof of Concept: Few-Cycle Pulse Generation and Carrier-Envelope-Phase Stabilization," in *A New Generation of High-Power, Waveform Controlled, Few-Cycle Light Sources* (M. Seidel, ed.), Springer Theses, pp. 37–74, Cham: Springer International Publishing, 2019.

[136] M. Y. Sander, E. P. Ippen, and F. X. Kärtner, "Carrier-envelope phase dynamics of octave-spanning dispersion-managed Ti: Sapphire lasers," *Optics Express*, vol. 18, pp. 4948–4960, Mar. 2010.

[137] K. Gürel, S. Hakobyan, V. J. Wittwer, S. Schilt, and T. Südmeyer, "Frequency Comb Stabilization of Ultrafast Lasers by Opto-Optical Modulation of Semiconductors," *IEEE Journal of Selected Topics in Quantum Electronics*, vol. 24, pp. 1–9, Sept. 2018.

[138] L. Karlen, G. Buchs, E. Portuondo-Campa, and S. Lecomte, "Efficient carrier-envelope offset frequency stabilization through gain modulation via stimulated emission," *Optics Letters*, vol. 41, pp. 376–379, Jan. 2016.

[139] K. Gürel, S. Schilt, and T. Südmeyer, "Carrier-Envelope Offset Frequency Stabilization of a Fiber Laser by Cross Gain Modulation," *IEEE Photonics Journal*, vol. 10, pp. 1–6, Apr. 2018.

[140] K. Hitachi, A. Ishizawa, T. Nishikawa, M. Asobe, and T. Sogawa, "Carrier-envelope offset locking with a 2f-to-3f self-referencing interferometer using a dual-pitch PPLN ridge waveguide," *Optics Express*, vol. 22, pp. 1629–1635, Jan. 2014.

[141] M. Bradler, P. Baum, and E. Riedle, "Femtosecond continuum generation in bulk laser host materials with sub-μJ pump pulses," *Applied Physics B*, vol. 97, pp. 561–574, Aug. 2009.

[142] J. M. Dudley, G. Genty, and S. Coen, "Supercontinuum generation in photonic crystal fiber," *Reviews of Modern Physics*, vol. 78, pp. 1135–1184, Oct. 2006.

[143] N. Raabe, T. Feng, T. Witting, A. Demircan, C. Brée, and G. Steinmeyer, "Role of Intrapulse Coherence in Carrier-Envelope Phase Stabilization," *Physical Review Letters*, vol. 119, p. 123901, Sept. 2017.

[144] G. Genty, S. Coen, and J. M. Dudley, "Fiber supercontinuum sources (Invited)," *JOSA B*, vol. 24, pp. 1771–1785, Aug. 2007.

[145] A. Braun, G. Korn, X. Liu, D. Du, J. Squier, and G. Mourou, "Self-channeling of high-peak-power femtosecond laser pulses in air," *Optics Letters*, vol. 20, pp. 73–75, Jan. 1995.

[146] A. Couairon and A. Mysyrowicz, "Femtosecond filamentation in transparent media," *Physics Reports*, vol. 441, pp. 47–189, Mar. 2007.

[147] L. Bergé, S. Skupin, R. Nuter, J. Kasparian, and J.-P. Wolf, "Ultrashort filaments of light in weakly ionized, optically transparent media," *Reports on Progress in Physics*, vol. 70, pp. 1633–1713, Sept. 2007.

[148] S. L. Chin, *Femtosecond Laser Filamentation*. Springer Series on Atomic, Optical, and Plasma Physics, New York, NY: Springer, 2010.

[149] J. B. Ashcom, R. R. Gattass, C. B. Schaffer, and E. Mazur, "Numerical aperture dependence of damage and supercontinuum generation from femtosecond laser pulses in bulk fused silica," *JOSA B*, vol. 23, pp. 2317–2322, Nov. 2006.

[150] A. Brodeur and S. L. Chin, "Band-Gap Dependence of the Ultrafast White-Light Continuum," *Physical Review Letters*, vol. 80, pp. 4406–4409, May 1998.

[151] A. Brodeur and S. L. Chin, "Ultrafast white-light continuum generation and self-focusing in transparent condensed media," *JOSA B*, vol. 16, pp. 637–650, Apr. 1999.

[152] G. Cerullo, A. Baltuška, O. D. Mücke, and C. Vozzi, "Few-optical-cycle light pulses with passive carrier-envelope phase stabilization," *Laser & Photonics Reviews*, vol. 5, no. 3, pp. 323–351, 2011.

[153] M. Bradler and E. Riedle, "Sub-20 fs µJ-energy pulses tunable down to the near-UV from a 1 MHz Yb-fiber laser system," *Optics Letters*, vol. 39, pp. 2588–2591, May 2014.

[154] A.-L. Calendron, H. Çankaya, G. Cirmi, and F. X. Kärtner, "White-light generation with sub-ps pulses," *Optics Express*, vol. 23, pp. 13866–13879, June 2015.

[155] D. E. Zelmon, D. L. Small, and R. Page, "Refractive-index measurements of undoped yttrium aluminum garnet from 0.4 to 5.0 Mm," *Applied Optics*, vol. 37, pp. 4933–4935, July 1998.

[156] A. Selivanov, I. Denisov, N. Kuleshov, and K. Yumashev, "Nonlinear refractive properties of Yb3+-doped KY(WO4)2 and YVO4 laser crystals," *Applied Physics B*, vol. 83, pp. 61–65, Apr. 2006.

[157] M. Pujol, M. Rico, C. Zaldo, R. Solé, V. Nikolov, X. Solans, M. Aguiló, and F. Díaz, "Crystalline structure and optical spectroscopy of Er3+-doped KGd(WO4)2 single crystals," *Applied Physics B*, vol. 68, pp. 187–197, Feb. 1999.

[158] R. Riedel, M. Schulz, M. J. Prandolini, A. Hage, H. Höppner, T. Gottschall, J. Limpert, M. Drescher, and F. Tavella, "Long-term stabilization of high power optical parametric chirped-pulse amplifiers," *Optics Express*, vol. 21, pp. 28987–28999, Nov. 2013.

[159] R. Riedel, A. Stephanides, M. J. Prandolini, B. Gronloh, B. Jungbluth, T. Mans, and F. Tavella, "Power scaling of supercontinuum seeded megahertz-repetition rate optical parametric chirped pulse amplifiers," *Optics Letters*, vol. 39, pp. 1422–1424, Mar. 2014.

[160] S. Xu, J. Qiu, T. Jia, C. Li, H. Sun, and Z. Xu, "Femtosecond laser ablation of crystals SiO2 and YAG," *Optics Communications*, vol. 274, pp. 163–166, June 2007.

[161] O. Dematteo Caulier, K. Mishchik, B. Chimier, S. Skupin, A. Bourgeade, C. Javaux Léger, R. Kling, C. Hönninger, J. Lopez, V. Tikhonchuk, and G. Duchateau, "Femtosecond laser pulse train interaction with dielectric materials," *Applied Physics Letters*, vol. 107, p. 181110, Nov. 2015.

[162] J. Rolle, L. Bergé, G. Duchateau, and S. Skupin, "Filamentation of ultrashort laser pulses in silica glass and KDP crystals: A comparative study," *Physical Review A*, vol. 90, p. 023834, Aug. 2014.

[163] M. Mero, B. R. Clapp, J. C. Jasapara, W. G. Rudolph, D. Ristau, K. Starke, J. Krüger, S. Martin, and W. Kautek, "On the damage behavior of dielectric films when illuminated with multiple femtosecond laser pulses," *Optical Engineering*, vol. 44, p. 051107, May 2005.

[164] M. Mero, A. Sabbah, J. Zeller, and W. Rudolph, "Femtosecond dynamics of dielectric films in the pre-ablation regime," *Applied Physics A*, vol. 81, pp. 317–324, July 2005.

[165] A. Jullien, J.-P. Rousseau, B. Mercier, L. Antonucci, O. Albert, G. Chériaux, S. Kourtev, N. Minkovski, and S. M. Saltiel, "Highly efficient nonlinear filter for femtosecond pulse contrast enhancement and pulse shortening," *Optics Letters*, vol. 33, pp. 2353–2355, Oct. 2008.

[166] M. Seidel, J. Brons, G. Arisholm, K. Fritsch, V. Pervak, and O. Pronin, "Efficient High-Power Ultrashort Pulse Compression in Self-Defocusing Bulk Media," *Scientific Reports*, vol. 7, pp. 1–8, May 2017.

[167] T. Südmeyer, F. Brunner, E. Innerhofer, R. Paschotta, K. Furusawa, J. C. Baggett, T. M. Monro, D. J. Richardson, and U. Keller, "Nonlinear femtosecond pulse compression at high average power levels by use of a large-mode-area holey fiber," *Optics Letters*, vol. 28, pp. 1951–1953, Oct. 2003.

[168] A. Killi, A. Steinmann, J. Dörring, U. Morgner, M. J. Lederer, D. Kopf, and C. Fallnich, "High-peak-power pulses from a cavity-dumped Yb:$KY(WO_4)_2$ oscillator," *Optics Letters*, vol. 30, pp. 1891–1893, July 2005.

[169] T. A. Birks, J. C. Knight, and P. S. J. Russell, "Endlessly single-mode photonic crystal fiber," *Optics Letters*, vol. 22, pp. 961–963, July 1997.

[170] M. Miranda, T. Fordell, C. Arnold, A. L'Huillier, and H. Crespo, "Simultaneous compression and characterization of ultrashort laser pulses using chirped mirrors and glass wedges," *Opt. Express*, vol. 20, pp. 688–697, Jan. 2012.

[171] B. Alonso, Í. J. Sola, and H. Crespo, "Self-calibrating d-scan: Measuring ultrashort laser pulses on-target using an arbitrary pulse compressor," *Scientific Reports*, vol. 8, pp. 1–8, Feb. 2018.

[172] E. Escoto, A. Tajalli, T. Nagy, and G. Steinmeyer, "Advanced phase retrieval for dispersion scan: A comparative study," *JOSA B*, vol. 35, pp. 8–19, Jan. 2018.

[173] S. Kleinert, *An Optical-Parametric Amplifier for the Visible*. Master Thesis, Leibniz Universität Hannover, Hannover, 2017.

[174] J. E. Rothenberg, "Pulse splitting during self-focusing in normally dispersive media," *Optics Letters*, vol. 17, pp. 583–585, Apr. 1992.

[175] G. Cerullo, M. Nisoli, and S. De Silvestri, "Generation of 11 fs pulses tunable across the visible by optical parametric amplification," *Applied Physics Letters*, vol. 71, pp. 3616–3618, Dec. 1997.

[176] R. L. Fork, C. V. Shank, C. Hirlimann, R. Yen, and W. J. Tomlinson, "Femtosecond white-light continuum pulses," *Optics Letters*, vol. 8, pp. 1–3, Jan. 1983.

[177] B. Borchers, A. Anderson, and G. Steinmeyer, "On the role of shot noise in carrier-envelope phase stabilization," *Laser & Photonics Reviews*, vol. 8, no. 2, pp. 303–315, 2014.

[178] L. Xu, T. W. Hänsch, C. Spielmann, A. Poppe, T. Brabec, and F. Krausz, "Route to phase control of ultrashort light pulses," *Optics Letters*, vol. 21, pp. 2008–2010, Dec. 1996.

[179] D. J. Jones, S. T. Cundiff, T. M. Fortier, J. L. Hall, and J. Ye, "Carrier–Envelope Phase Stabilization of Single and Multiple Femtosecond Lasers," in *Few-Cycle Laser Pulse Generation and Its Applications* (F. X. Kärtner, ed.), Topics in Applied Physics, pp. 317–343, Berlin, Heidelberg: Springer, 2004.

[180] K. Holman, R. Jones, A. Marian, S. Cundiff, and J. Ye, "Detailed studies and control of intensity-related dynamics of femtosecond frequency combs from mode-locked Ti:sapphire lasers," *IEEE Journal of Selected Topics in Quantum Electronics*, vol. 9, pp. 1018–1024, July 2003.

[181] L. Matos, O. D. Mücke, J. Chen, and F. X. Kärtner, "Carrier-envelope phase dynamics and noise analysis in octave-spanning Ti:sapphire lasers," *Optics Express*, vol. 14, pp. 2497–2511, Mar. 2006.

[182] G. D. Domenico, S. Schilt, and P. Thomann, "Simple approach to the relation between laser frequency noise and laser line shape," *Applied Optics*, vol. 49, pp. 4801–4807, Sept. 2010.

[183] S. Hakobyan, V. J. Wittwer, P. Brochard, K. Gürel, S. Schilt, A. S. Mayer, U. Keller, and T. Südmeyer, "Full stabilization and characterization of an optical frequency comb from a diode-pumped solid-state laser with GHz repetition rate," *Optics Express*, vol. 25, pp. 20437–20453, Aug. 2017.

[184] O. D. Mücke, R. Ell, A. Winter, J.-W. Kim, J. R. Birge, L. Matos, and F. X. Kärtner, "Self-Referenced 200 MHz Octave-Spanning Ti:Sapphire Laser with 50 Attosecond Carrier-Envelope Phase Jitter," *Optics Express*, vol. 13, pp. 5163–5169, June 2005.

[185] S. Rausch, T. Binhammer, A. Harth, E. Schulz, M. Siegel, and U. Morgner, "Few-cycle oscillator pulse train with constant carrier-envelope- phase and 65 as jitter," *Opt. Express*, vol. 17, pp. 20282–20290, Oct. 2009.

[186] B. Majaron, H. Lukac, and M. Copic, "Population dynamics in Yb:Er:phosphate glass under neodymium laser pumping," *IEEE Journal of Quantum Electronics*, vol. 31, pp. 301–308, Feb. 1995.

[187] S. Taccheo, P. Laporta, S. Longhi, O. Svelto, and C. Svelto, "Diode-pumped bulk erbium-ytterbium lasers," *Applied Physics B*, vol. 63, pp. 425–436, Nov. 1996.

[188] G. J. Spühler, L. Krainer, E. Innerhofer, R. Paschotta, K. J. Weingarten, and U. Keller, "Soliton mode-locked Er:Yb:glass laser," *Optics Letters*, vol. 30, pp. 263–265, Feb. 2005.

[189] F. Ö. Ilday, D. K. Kesim, M. Hoffmann, and C. J. Saraceno, "Discrete Similariton and Dissipative Soliton Modelocking for Energy Scaling Ultrafast Thin-Disk Laser Oscillators," *IEEE Journal of Selected Topics in Quantum Electronics*, vol. 24, pp. 1–12, Sept. 2018.

[190] A. F. J. Runge, D. D. Hudson, K. K. K. Tam, C. M. de Sterke, and A. Blanco-Redondo, "The pure-quartic soliton laser," *Nature Photonics*, pp. 1–6, May 2020.

[191] Y. Khanukaeva, T. Lang, A. Tajalli, J. R. Andrade, T. Binhammer, and U. Morgner, "Efficient fast-tunable femtosecond visible radiation based on intracavity sum-frequency generation in a NIR NOPO," in *CLEO: Science and Innovations*, pp. STh1P–6, Optical Society of America, 2016.

[192] L. Rust, *Erzeugung Und Detektion von THz-Pulsen*. PhD thesis, Leibniz Universität Hannover, master thesis, 2018.

[193] L. Beichert, Y. Binhammer, J. R. Andrade, A.-K. Kniggendorf, B. Roth, and U. Morgner, "Non-collinear optical parametric oscillator for video rate stimulated raman spectroscopy of microplastics," in *2019 Conference on Lasers and Electro-Optics Europe & European Quantum Electronics Conference (CLEO/Europe-EQEC)*, pp. 1–1, IEEE, 2019.

[194] W. L. Barnes, A. Dereux, and T. W. Ebbesen, "Surface plasmon subwavelength optics," *Nature*, vol. 424, pp. 824–830, Aug. 2003.

[195] C. Karnetzky, P. Zimmermann, C. Trummer, C. Duque Sierra, M. Wörle, R. Kienberger, and A. Holleitner, "Towards femtosecond on-chip electronics based on plasmonic hot electron nano-emitters," *Nature Communications*, vol. 9, p. 2471, June 2018.

[196] X. Li, Y. Wu, D. Steel, D. Gammon, T. H. Stievater, D. S. Katzer, D. Park, C. Piermarocchi, and L. J. Sham, "An All-Optical Quantum Gate in a Semiconductor Quantum Dot," *Science*, vol. 301, pp. 809–811, Aug. 2003.

[197] E. D. Fabrizio, S. Schlücker, J. Wenger, R. Regmi, H. Rigneault, Giuseppe Calafiore, M. West, S. Cabrini, M. Fleischer, N. F. van Hulst, M. F. Garcia-Parajo, A. Pucci, D. Cojoc, C. A. E. Hauser, and M. Ni, "Roadmap on biosensing and photonics with advanced nano-optical methods," *Journal of Optics*, vol. 18, no. 6, p. 063003, 2016.

[198] L. Shi, R. Nicolas, J. R. C. Andrade, W. Boutu, D. Franz, T. Heidenblut, C. Reinhardt, U. Morgner, H. Merdji, and M. Kovacev, "Impact of Plasmon-Induced Atoms Migration in Harmonic Generation," *ACS Photonics*, vol. 5, pp. 1208–1214, Apr. 2018.

[199] L. Shi, B. Iwan, R. Nicolas, Q. Ripault, J. R. C. Andrade, S. Han, H. Kim, W. Boutu, D. Franz, T. Heidenblut, C. Reinhardt, B. Bastiaens, T. Nagy, I. Babushkin, U. Morgner, S.-W. Kim, G. Steinmeyer, H. Merdji, and M. Kovacev, "Self-optimization of plasmonic nanoantennas in strong femtosecond fields," *Optica*, vol. 4, pp. 1038–1043, Sept. 2017.

[200] L. Shi, J. R. C. Andrade, H. Kim, S. Han, R. Nicolas, D. Franz, W. Boutu, T. Heidenblut, F. B. Segerink, B. Bastiaens, H. Merdji, S.-W. Kim, U. Morgner, and M. Kovačev, "Investigating the origin of third harmonic generation from diabolo optical antennas," *Applied Physics Letters*, vol. 111, p. 173102, Oct. 2017.

[201] S. A. Maier, *Plasmonics: Fundamentals and Applications*. New York, NY: Springer US, 2007.

[202] L. Shi, J. R. C. Andrade, A. Tajalli, J. Geng, J. Yi, T. Heidenblut, F. B. Segerink, I. Babushkin, M. Kholodtsova, H. Merdji, B. Bastiaens, U. Morgner, and M. Kovacev, "Generating Ultrabroadband Deep-UV Radiation and Sub-10 nm Gap by Hybrid-Morphology Gold Antennas," *Nano Letters*, vol. 19, pp. 4779–4786, July 2019.

[203] J.-M. Yi, A. Cuche, E. Devaux, C. Genet, and T. W. Ebbesen, "Beaming Visible Light with a Plasmonic Aperture Antenna," *ACS Photonics*, vol. 1, pp. 365–370, Apr. 2014.

[204] J.-M. Yi, V. Smirnov, X. Piao, J. Hong, H. Kollmann, M. Silies, W. Wang, P. Groß, R. Vogelgesang, N. Park, and C. Lienau, "Suppression of Radiative Damping and Enhancement of Second Harmonic Generation in Bull's Eye Nanoresonators," *ACS Nano*, vol. 10, pp. 475–483, Jan. 2016.

[205] D. Hanna, "Astigmatic Gaussian beams produced by axially asymmetric laser cavities," *IEEE Journal of Quantum Electronics*, vol. 5, pp. 483–488, Oct. 1969.

[206] D. Kane and R. Trebino, "Characterization of arbitrary femtosecond pulses using frequency-resolved optical gating," *Quantum Electronics, IEEE Journal of*, vol. 29, no. 2, pp. 571–579, 1993.

[207] F. Gardner, *Phaselock Techniques*. Wiley, 3rd ed., 2005.

List of Publications

Journal publications

1. *Under peer review*, C. M. Dietrich, I. Babushkin, **J. R. C. Andrade**, H. Rao, A. Demircan and U. Morgner, "Higher-order dispersion and the spectral behaviour in a doubly resonant optical parametric oscillator," Optics Letters, (2020)

2. **J. R. C. Andrade**, N. Modsching, A. Tajalli, C. M. Dietrich, S. Kleinert, F. Placzek, B. Kreipe, S. Schilt, V. J. Wittwer, T. Südmeyer, and U. Morgner, "Carrier-envelope offset frequency stabilization of a thin-disk laser oscillator via depletion modulation," IEEE Photonics Journal **12**(2), 1-9 (2020)

3. C. Dietrich, I. Babushkin, **J. Andrade**, H. Rao, A. Demircan, and U. Morgner, "Field enhancement in a doubly resonant optical parametric oscillator," Optics Letters **44**(19), 4909-4912 (2019).

4. L. Shi, **J. R. C. Andrade**, A. Tajalli, J. Geng, J. Yi, T. Heidenblut, F. B. Segerink, I. Babushkin, M. Kholodtsova, H. Merdji, B. Bastiaens, U. Morgner, and M. Kovacev, "Generating Ultrabroadband Deep-UV Radiation and Sub-10 nm Gap by Hybrid-Morphology Gold Antennas," Nano Lett. **19**(7), 4779-4786 (2019)

5. L. Shi, **J. R. Andrade**, J. Yi, M. Marinskas, C. Reinhardt, E. Almeida, U. Morgner, and M. Kovacev, "Nanoscale broadband deep-ultraviolet light source from plasmonic nanoholes," ACS Photonics **6**(4), 858-863 (2019)

6. I. Babushkin, A. Galan, V. Vaicaitis, A. Husakou, F. Morales, A. Demircan, **J. Andrade**, U. Morgner, and M. Ivanov, "All-optical attoclock: accessing exahertz dynamics of optical tunnelling through terahertz emission," arXiv preprint arXiv: 1803.04187 (2018)

7. L. Shi, B. Iwan, Q. Ripault, **J. R. Andrade**, S. Han, H. Kim, W. Boutu, D. Franz, R. Nicolas, T. Heidenblut, and others, "Resonant-plasmon-assisted subwavelength ablation by a femtosecond oscillator," Physical review applied **9**(2), 024001 (2018)

8. L. Shi, R. Nicolas, **J. R. Andrade**, W. Boutu, D. Franz, T. Heidenblut, C. Reinhardt, U. Morgner, H. Merdji, and M. Kovacev, "Impact of plasmon-induced atoms migration in harmonic generation," ACS photonics **5**(4), 1208-1214 (2018)

9. L. Shi, **J. R. Andrade**, H. Kim, S. Han, R. Nicolas, D. Franz, W. Boutu, T. Heidenblut, F. B. Segerink, B. Bastiaens, and others, "Investigating the origin of third harmonic generation from diabolo optical antennas," Applied physics letters **111**(17), 173102 (2017)

10. L. Shi, B. Iwan, R. Nicolas, Q. Ripault, **J. R. Andrade**, S. Han, H. Kim, W. Boutu, D. Franz, T. Heidenblut, and others, "Self-optimization of plasmonic nanoantennas in strong femtosecond fields," Optica **4**(9), 1038-1043 (2017)

11. N. Pfullmann, M. Noack, **J. R. C. Andrade**, S. Rausch, T. Nagy, C. Reinhardt, V. Knittel, R. Bratschitsch, A. Leitenstorfer, D. Akemeier, A. Hütten, M. Kovacev, and U. Morgner, "Nano-antennae assisted emission of extreme ultraviolet radiation," ANNALEN DER PHYSIK **526**(3-4), 119-134 (2014)

Talks at international conferences

1. **J. Andrade**, S. Kleinert, A. Tajalli, C. Dietrich, F. Placzek, B. Kreipe, and U. Morgner, "Depletion based thin-disk CEP stabilization," in 2019 Conference on Lasers and Electro-Optics Europe & European Quantum Electronics Conference (CLEO/Europe-EQEC) (2019), pp. 1-1

2. **J. R. C. Andrade**, F. Placzek, B. Kreipe, and U. Morgner, "Depletion based thin-disk CEP stabilization concept and realization," in 8th EPS-QEOD Europhoton Conference (2018)

3. (Invited, given on behalf of Liping Shi) L. Shi, **J. R. Andrade**, B. Iwan, Q. Ripault, S. Han, H. Kim, W. Boutu, D. Franz, R. Nicolas, and T. Heidenblut, "Subwavelength laser ablation using impulsively excited surface plasmons," in 32nd URSI GASS (2017).

4. **J. Andrade**, M. Noack, N. Pfullmann, C. Waltermann, M. Kovacev, H. M. J. Bastiaens, F. B. Segerink, V. Knittel, D. Akemeier, A. Hütten, A. Leitenstorfer, and U. Morgner, "Gold bowtie nanoantennas generating UV," in Research in Optical Sciences, Research in Optical Sciences (Optical Society of America, 2014), p. HW4C.5

International conferences, others

1. I. Babushkin, A. Galan, V. Vaicaitis, A. Husakou, F. Morales, A. Demircan, **J. Andrade**, U. Morgner, and M. Ivanov, "Optical attoclock using terahertz radiation," in 2019 Conference on Lasers and Electro-Optics Europe & European Quantum Electronics Conference (CLEO/Europe-EQEC) (2019), pp. 1-1

2. I. Babushkin, A. Galan, V. Vaicaitis, A. Husakou, F. Morales, A. Demircan, **J. Andrade**, U. Morgner, and M. Ivanov, "Subcycle dynamics of ionization revealed via polarization of lowest harmonics," in CLEO: QELS_Fundamental Science (2019), pp. FF3C-2

3. L. Beichert, Y. Binhammer, **J. R. Andrade**, A.-K. Kniggendorf, B. Roth, and U. Morgner, "Non-collinear optical parametric oscillator for video rate stimulated raman spectroscopy of microplastics," in 2019 Conference on Lasers and Electro-Optics Europe & European Quantum Electronics Conference (CLEO/Europe-EQEC) (2019), pp. 1-1.

4. C. Dietrich, I. Babushkin, **J. Andrade**, L. Rust, and U. Morgner, "Intracavity enhancement in a doubly resonant OPO," in CLEO: Science and Innovations (2019), pp. STh4E-2

5. L. Beichert, Y. Binhammer, **J. R. C. Andrade**, A. K. Kniggendorf, and U. Morgner, "Non-collinear Optical Parametric Oscillator for Video-Rate Stimulated Raman Spectroscopy of Microplastics," in 8th EPS-QEOD Europhoton Conference (2018)

6. Y. Binhammer, T. Binhammer, L. Beichert, **J. R. C. Andrade**, A. Tajalli, and U. Morgner, "Scalability of an ultrabroadband non-collinear optical parametric oscillator (NOPO) in the visible," in 8th EPS-QEOD Europhoton Conference (2018)

7. C. M. Dietrich, I. Babushkin, **J. R. C. Andrade**, and U. Morgner, "Doubly-resonant 2?m degenerate optical parametric- enhancement cavity," in 8th EPS-QEOD Europhoton Conference (2018)

8. S. Kleinert, A. Tajalli, B. Kreipe, D. Zuber, **J. R. C. Andrade**, and U. Morgner, "Ultrashort pulses from an OPCPA in the visible," in 8th EPS-QEOD Europhoton Conference (2018)

9. Y. Binhammer, T. Binhammer, F. Placzek, B. Kreipe, **J. R. Andrade**, T. Lang, A. Tajalli, and U. Morgner, "Widely tunable femtosecond non-collinear optical parametric oscillator (NOPO) in VIS," in The European Conference on Lasers and Electro-Optics (2017), p. CF_P_24

10. Y. Khanukaeva, T. Lang, A. Tajalli, **J. R. C. Andrade**, T. Binhammer, and U. Morgner, "Fast-tunable femtosecond visible radiation via intracavity sum frequency generation in a NIR NOPO," in 7th EPS-QEOD Europhoton Conference (2016)

11. Y. Khanukaeva, T. Lang, A. Tajalli, **J. R. Andrade**, T. Binhammer, and U. Morgner, "Efficient fast-tunable femtosecond visible radiation based on intracavity sum-frequency generation in a NIR NOPO," in CLEO: Science and Innovations (2016), pp. STh1P-6

12. B. Kreipe, **J. R. C. Andrade**, B. Deppe, C. Kränkel, and U. Morgner, "160 fs pulses from a Kerr-lens mode-locked Yb3+:Lu2O3 thindisk oscillator," in 7th EPS-QEOD Europhoton Conference (2016)

13. B. Kreipe, **J. R. C. de Andrade**, C. Kränkel, and U. Morgner, "Kerr-lens mode-locked Yb3+:Lu2O3 thin-disk laser," in 2016 Conference on Lasers and Electro-Optics (CLEO) (2016), pp. 1-2

14. A. Harth, S. Rausch, T. Nagy, **J. Andrade**, C. Hoffmann, T. Lang, T. Binhammer, and U. Morgner, "4-f prism-based pulse shaper supporting single-cycle pulses in the visible," in Conference on Lasers and Electro-Optics - International Quantum Electronics Conference (2013), p. paper-CFIE_P_1

15. A. Tajalli, T. Nagy, Anne Harth, **J. R. Andrade**, and U. Morgner, "Towards characterization and compression of 1.5 octaves spectrum spanning from VIS to IR from two-color pumped OPCPA system," in Advanced Solid-State Lasers Congress (2013), p. paper-JTh2A

Acknowledgements

I would like to start off by saying that this list will not be exhaustive, otherwise it would just be a book on its own. I appreciate deeply all those that have been present in so many stages of my life and education and it is hard to put to words the gratitude I have towards everyone.

In first place I would like to thank Uwe Morgner for the opportunity you gave me to work in your group. Above all I admire your passion and incredible knowledge – which you were ready to share and satisfy so many of my questions – towards ultrafast science. I am very grateful for your patience and also the freedom given to me to try some unconventional things.

To Milutin Kovačev and Liping Shi for their always energetic pursuits in plasmonics. Specially to Liping who is a great friend and with whom I had lots of interesting discussions regarding the weirdest of nano-phenomena.

I would like to thank Prof. Thomas Südmeyer for being the external examiner of my thesis and the promptness of the Neuchâtel team to help with the laser stabilization and their input in manuscript writing. Thank you Dr. Stephane Schilt and specially Norbert Modsching and his infectious positiveness.

To all the mentors whose knowledge laid the groundwork that enabled my own ultrafast journey: Thomas, Stefan, Tino, Anne... You all taught me so much and cared deeply about me and had the patience to answer my endless questions. Thank you so much.

Towards the theoretical people in our group I also have a lot of gratitude. Thank you for your mathematical insights Ayhan Demircan, and Ihar Babushkin, your inventiveness and ingenuity are amazing and I always enjoyed discussing things with you.

A very special thank you to Ayhan Tajalli, whose friendship and mentorship mean a lot to me, and your support was invaluable all these years. I will definitely miss kicking your a** in cricket!

To the present and past members of the AG Morgner I would like to thank for all the good times and beers and barbecues and scientific or non-scientific discussions and inputs to this thesis. Martin, you know you did too much and I appreciate every second of your damn patience, and your scientific wit is so sharp and admirable. Your input in this manuscript, exposing the flaws, just made it incredibly better. Christian, may we meet in the slopes many times. Thank you for your help in and out of the lab. Sven, David and Bernhard, I am sorry for having disrupted your work so many times, but I really enjoyed our discussions. I also appreciate all our interactions Welm, and your input to the thesis made me see things from a different perspective. Thanks Dmitrii, Robin, Christoph, Luise, Jintao, Han, Surajit, Steffi, Jan and all others that made this work group a very lively place! I am forever in debt to the secretariat of our group whose fast acting response on all business matters and taking all the pressure from the bureaucratic layers made work much easier and enjoyable. To the workshop I can just say that without you none of my work would have ever been possible. Thank you for all those parts where I said "well, it's very urgent" and I had them on my desk the next day. And my gratitude also goes to Kai-Martin who helped me so much with the electronic parts when I just felt like throwing everything away.

But outside of work, I also want to thank all those that made "mich wohlfühlen". Basketball, ErichWG, AP, Fabian, Gaia, Ghandi, Rodas, Faro, Fabio, you all made me stay sane.

For all it is worth, for all the time spent together, thank you Daggi.

Mars, thanks for visiting me every night in this past 3 months!

And to close this chapter, I would like to send a heartfelt thank you to my family, to whom I know it is hard to be so far away all the time, but without your love and support I would had never reached this point of my life. To Rieke whose help and love in this last few months just made writing this thesis a reality.

A big big wholehearted thank you to all of you.